AN INVESTIGATION INTO THE SPECTRAL TRANSFER FUNCTION AND CHARACTERIZATION OF A TERRESTRIAL SOLAR-BLIND ULTRAVIOLET ELECTRO-OPTICAL SYSTEM

by

Casper Johannes Coetzer

Submitted in partial fulfilment of the requirements for the degree

Master of Engineering (Electronic Engineering)

in the

Department of Electrical, Electronic and Computer Engineering

Faculty of Engineering, Built Environment and Information Technology

UNIVERSITY OF PRETORIA

October 2014

SUMMARY

AN INVESTIGATION INTO THE SPECTRAL TRANSFER FUNCTION AND CHARACTERIZATION OF A TERRESTRIAL SOLAR-BLIND ULTRAVIOLET ELECTRO-OPTICAL SYSTEM

by

Casper Johannes Coetzer

Supervisor: Prof. F.W. Leuschner

Department: Electrical, Electronic and Computer Engineering

University: University of Pretoria

Degree: Master of Engineering (Electronic Engineering)

Keywords: Solar-blind, Ultraviolet (UV), camera characterisation, corona, high voltage, spectral transfer function.

Solar-blind Ultraviolet cameras are used to detect missile plumes and perform the detection of corona on high voltage electrical lines. This study investigates the influence of the spectral transfer function of a specific solar-blind Ultraviolet camera upon Ultraviolet energy measurement results. In addition to the spectral transfer response investigated, is the influence of other related factors, including the specific camera operation and design.

The possibility that the particular camera's measurements are being influenced by its own spectral transfer function, is initially investigated by using a simplified model. The objective of the model was to determine if the hypothesis is possible. In addition to the spectral transfer function of the camera, other factors that could influence camera measurements were also investigated in the literature. Included are highlights from other research conducted utilising this type of camera for high voltage electrical purposes, as well as comments for further research.

Subsequently experiments were executed to characterise the camera, including the determination of the spectral transfer function of the specific camera, taking into considering limitations of the camera and related equipment.

Derived from the spectral transfer of the camera and the other experiments and literature, a proposed method of calibration is presented, as well as suggestions for the improvement of the camera and better utilisation thereof.

OPSOMMING

'N ONDERSOEK VAN DIE SPEKTRALE OORDRAGFUNKSIE EN KARAKTERISERING VAN 'N AARDGEBONDE SON-BLIND ULTRAVIOLET ELEKTRO-OPTIESE STELSEL

deur

Casper Johannes Coetzer

Studieleier:	Prof F.W. Leuschner
Departement:	Elektriese, Elektroniese en Rekenaaringenieurswese
Universiteit:	Universiteit van Pretoria
Graad:	Magister in Ingenieurswese (Elektroniese Ingenieurswese)
Sleutelwoorde:	Sonblind, Ultraviolet (UV), kamera-karakterisering , korona, hoog-spanning, spektrale oordragfunksie.

Son-blind ultraviolet kameras word gebruik om missiel uitlaat gasse sowel as korona op hoogspannings kraglyne op te spoor. Die studie ondersoek die invloed van die spektrale oordragfunksie van 'n spesifieke son-blind ultraviolet kamera op ultraviolet energie meetingsresultate. Addisioneel tot die spektrale response geondersoek, is die invloed van ander verwante faktore op metings insluitend die spesifieke kamera se werking en ontwerp.

Die moontlikheid dat die spesifieke kamera se metings beïnvloed word deur sy eie spektrale oordragfunksie, word aanvanklik eers ondersoek aan die hand van 'n eenvoudige model. Die doel van die model is om te bepaal of die hipotese moontlik is. Addisioneel tot die spektrale oordragfunksie van die kamera, word ander faktore wat die kamerametings kon beïnvloed het, ook ondersoek in die literatuur. Ingesluit is hoogtepunte van ander navorsing wat die tipes kameras gebruik vir hoogspannings elektriese doeleindes, plus kommentaar vir verdere navorsing.

Vervolgens is eksperimente uitgevoer om die kamera te karakteriseer, insluitend die bepaling van die spesifieke kamera se spektrale oordragfunksie, met inagneming van die beperkings van kamera en verwante toerusting.

Afgelei uit die spektrale oordragfunksie van die kamera en die ander eksperimente en literatuurstudie, is 'n voorgestelde kalibrasiemetode aangebied, asook voorstelle vir die verbetering en die kamera en meer effektiewe gebruik daarvan.

LIST OF ABBREVIATIONS

AOI	Area of Interest (defined as a portion of an image)
CCD	Charge Coupled Device (related to detectors)
COG	Centre of Gravity (blob type images)
DR	Dynamic Range
EBI	Equivalent Background Interference (Image Intensifier related parameter)
FOV	Field of View (for a lens)
FWHM	Full Width at Half Maximum (related to events or photon counts)
HVT	High Voltage Transmission
IICCD	Image Intensified CCD
ICCD	Intensified CCD
nm	nano metre (wavelengths)
PD	Partial Discharge
UV	Ultraviolet
UVA	Ultraviolet A (315 nm to 400 nm)
UVB	Ultraviolet B (280 nm to 350 nm)
UVC	Ultraviolet C (100 nm to 280 nm)

TABLE OF CONTENTS

TABLE OF FIGURES

LIST OF TABLES

CHAPTER 1   INTRODUCTION

1.1   PROBLEM STATEMENT

1.1.1   Context

Solar-blind Ultraviolet UV cameras are used for various applications such as the detection of high voltage electrical discharges (corona), missile plumes, rifle muzzle flashes and fire within the solar-blind UV spectrum (Appendix A.1.) [1-4]. The term solar-blind implies the absence of a part of the sun's radiation on earth, because it is blocked by the earth's ozone layer and attenuated by the earth's atmosphere [1]. The relevant wavelengths are 160 to 280 nm, which is a portion of the ultraviolet C spectral band [2]. Only 200 to 280 nm is detectable within the earth's atmosphere, whereas the shorter wavelengths (160 to 199 nm) is not, as they are extremely attenuated by the atmosphere. The absence of the sun as a source at the UV solar-blind wavelengths enables the detection of sources emitting at these wavelengths without interference from the sun [2, 4].

Solar-blind UV cameras currently utilize an image intensifier type technology that produces images which differ from Charge Couple Devices (CCDs) [4]. These image intensifiers have an on-off time response referred to as the dead-time that produces blob type images as illustrated later in this study [5]. Consequently, image intensifier type camera images require a specific type of image processing to measure the energy of a source which is referred to here as counting [6-12].

Solar-blind UV Corona cameras for electrical inspection are only used currently for the observation of corona. These cameras currently do not perform radiometric measurements (measurement of optical power), using the typical quantities such as irradiance and radiance, as summarised in Appendix A.2 [13]. The theoretical model and practical measurements by Du Toit for the particular solar-blind UV corona camera investigated here differed from each other [14], which implied that further investigations were required to improve the measurements.

1.1.2   Research gap

This investigation sets out to improve the radiometric measurements by solar-blind UV cameras specifically for electrical inspection applications. Electrical maintenance teams inspecting power lines need to quantify the amount of optical flux emitted from UV corona from the power line, as earlier research implied that there is a relation between optical flux detected and electrical energy loss. The maintenance teams need to be able to decide if critical expensive electrical components

need to be replaced, based on the value (or level) of measurements. Furthermore, those involved in electrical research using solar-blind UV cameras, also require additional information with regards to the solar-blind UV camera modelling.

1.2 RESEARCH OBJECTIVE AND QUESTIONS

The objective is to improve the solar-blind UV camera's measurement of the solar-blind UV energy, within an electrical application.

Questions that arise from the objective are:

- Why do results obtained from an earlier model and actual measurements differ?
- How can a camera with limited measurement ability be characterized?
- What additional factors need to be considered in order to improve measurements?

1.3 HYPOTHESIS AND APPROACH

It is hypothesised that the following need to be considered to improve the solar-blind UV camera's radiometric measurements:

- The main contributor is hypothesised to be the actual camera spectral bandwidth.
- The distance between the source and the camera needs be considered in measurements.
- Extreme atmospheric attenuation in the UVC spectrum.
- Camera processing will have to be modified or adapted to measure source energy.
- Electric aspects that need to be incorporated as a part of measurements. An example is the 60 Hz or 50 Hz alternate current (AC) of a power line which creates a periodic fluctuating on and off UV source.

The approach within this study is thus as follows:

- Collect and study literature related to radiometric measurements.
- Present an analysis of the status of the current solar-blind UV camera used within the electrical field.
- Use a simplified model to investigate the influence of the camera's spectral transfer function on measurements.
- Use an available camera to characterise the camera operation through a set of experiments.
- Measure the actual spectral transfer function of the camera experimentally.
- Determine if the measured spectral transfer function and the simplified model can clarify the shortcomings in the previous model.

1.4   RESEARCH GOALS

The goals of the particular research are:

- To determine the spectral transfer function of a particular solar-blind UV camera.
- Identify what other factors influence the measurements.

1.5   RESEARCH CONTRIBUTION

The contributions are as follows:

- Determining the influence of a solar-blind UV camera's spectral response on optical flux measurements.
- Identifying and characterizing the parameters of a solar-blind UV camera.
- Deriving and identifying an improved calibration setup and camera processing with the objective of improving the accuracy of the solar-blind UV measurements.
- Providing an insight into the operation of a solar-blind UV camera for the electrical researcher.

1.6   OVERVIEW OF STUDY

Chapter 1 presents a summary and overview of the study. The objective is to determine the influence of a solar-blind UV camera's spectral transfer function on optical UV measurements of a solar-blind UV source.

Chapter 2 discusses the preliminary feasibility study, as well as a background literature related to UV phenomenology and the camera operation. The chapter commences with the hypothesis of the influence of the camera's spectral transfer function on a measurement with a model. Furthermore, this chapter provides an overview of UV sources, solar-blind UV atmospheric attenuation, lens transfer function, solar-blind filters, solar-blind detector technology and photon count algorithms.

 Chapter 3 describes experiments used to characterise a particular solar-blind camera. Included is the spectral characterisation of the solar-blind camera. Chapter 4 presents the results of the experimental and theoretical investigations of a solar-blind UV camera.

Chapter 5 provides short discussions and remarks on the experimental results.

Chapter 6 presents a number of conclusions based on the experimental results and the information presented in the other chapters.

Finally, Chapter 7 provides recommendations for further investigations and studies.

CHAPTER 2   LITERATURE STUDY

2.1   CHAPTER OBJECTIVES

The solar-blind UV camera literature investigation is based on the following objectives:

- To determine how a camera's spectral transfer function can be ascertained through measurement.
- To determine the influence of source and environment on the measurement of energy.
- To create an understanding of the characterisation of a camera.
- To understand the photon count mechanism of an Image intensifier type camera.
- To summarise and investigate previous attempts to find the relation between optical and electrical energy as applicable to high voltage corona.

2.2   SPECTRAL RESPONSE OF A SOLAR-BLIND CAMERA

2.2.1   A simplified model of the spectral transfer function

The hypothesis that the solar-blind camera's own spectral response has an influence on the energy it detects is first investigated by means of a simplified model, as illustrated in **Figure 2.1**. The model includes a source that is a reference Planck source [5] and a camera consisting of a lens, filter and detector. Energy from a source, in general, is attenuated with distance via the atmosphere [15, 16]. This simplified model however, assumes a short distance of two metres between source and the camera, with the atmospheric attenuation neglected for such a short distance. The distance of two metres is based on the minimum focussing distance of the camera investigated. These assumptions are of course a simplification of actual UV optical flux (energy) measurement, with more detail provided in later sections.
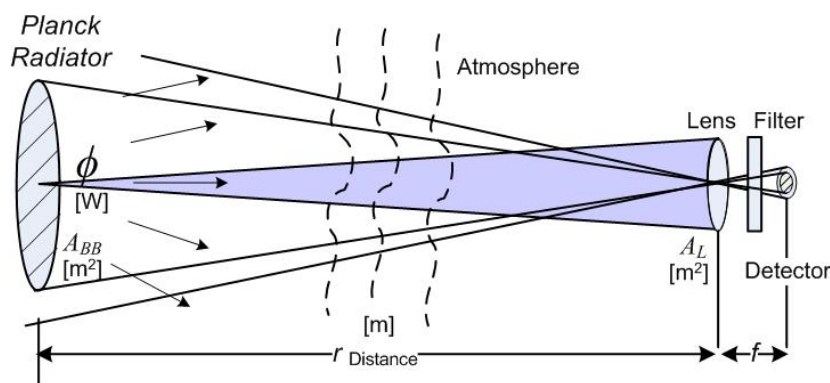
Figure 2.1. Simplified source and camera model.

The camera's spectral transfer function is modelled with three different estimated spectral responses. The estimated (postulated) camera spectral responses modelled are a Gauss shaped, a narrowband response and a wideband spectral response model of Du Toit and Uvirco [13,14]. **Figure 2.2** illustrates the three spectral transfer functions implemented in the model in terms of wavelength (symbol λ) and Detected Quantum Efficiency (DQE), which is the energy throughput (maximum 1) at each wavelength. Refer to Appendix A.3 for the simulation code.
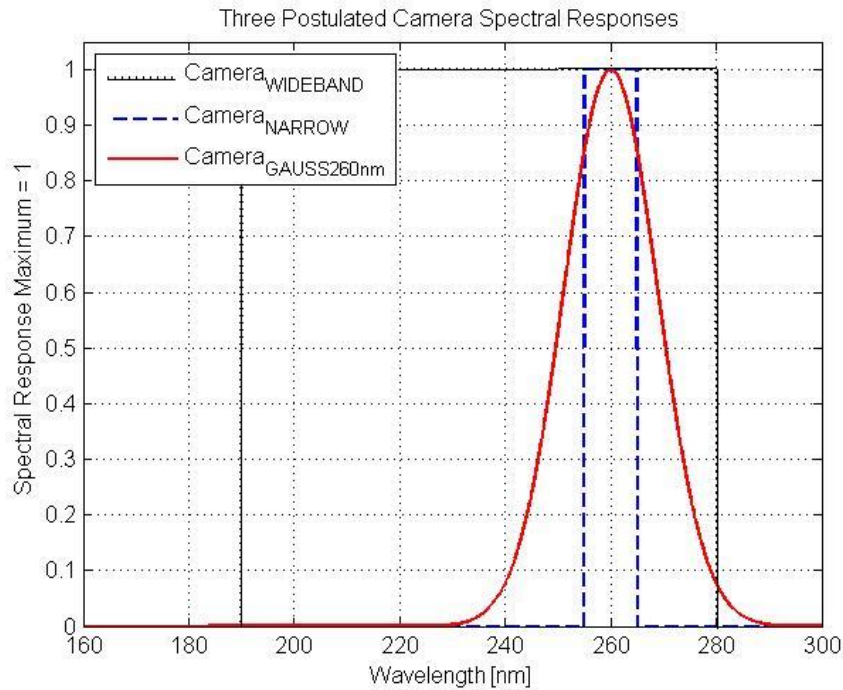
Figure 2.2. Comparison of three camera spectral responses.

The radiated optical flux Φ from a source with unit Watts that arrives at the lens pupil ("effective area ") area A_L [m^2], in terms of spectral Irradiance E_λ for each wavelength (units [W.m^{-2}.nm^{-1}]) can be described by the relation [17,18] :

$$E_\lambda = \frac{\partial \phi_\lambda}{\partial A_L} = \frac{L_\lambda \partial A_O}{r^2} \tau_\lambda , \qquad (2.1)$$

with

  A_O the source area [m^2],

  L_λ the source spectral radiance [W.sr^{-1}.m^{-2}.nm^{-1}],

  r the distance between the source and object in metres [m],

  and

  τ_λ or $\tau_{A\lambda}$ the atmospheric transmittance at each wavelength.

Note: The subscript λ for terms indicated implies here a dependency on wavelength.

The energy incident upon the lens of a camera consists of a multitude of wavelengths, which implies that a summation of all wavelengths is required using (2.1) [17], giving rise to

$$E_{LENS} = \int_0^\infty \frac{\partial \phi_\lambda}{\partial A_L} d\lambda = \int_0^\infty \frac{L_\lambda \partial A_O}{r^2} \tau_\lambda d\lambda \; . \tag{2.2}$$

A camera is only able to measure the energy within its own spectral response S_λ , which implies that the energy can be described by adapting relation (2.2), which is

$$E_{MEASURED}(\lambda) = \int_0^\infty L_\lambda \frac{\partial A_{SOURCE}}{r^2} \tau_{A\lambda} S_\lambda . \partial \lambda \; . \tag{2.3}$$

Figure 2.3 compares the results of the model using relation (2.3) for the three different camera spectral responses. The horizontal axis indicates the source energy in terms of absolute temperature (in Kelvin [K]) for a Planck source relation (section 2.3.1) [18]. The vertical axis indicates the energy that reaches the camera lens input, weighted by the camera's spectral response. A Planck source's energy is described in terms of absolute temperature, which implies that the higher the absolute temperature, the higher the source energy.
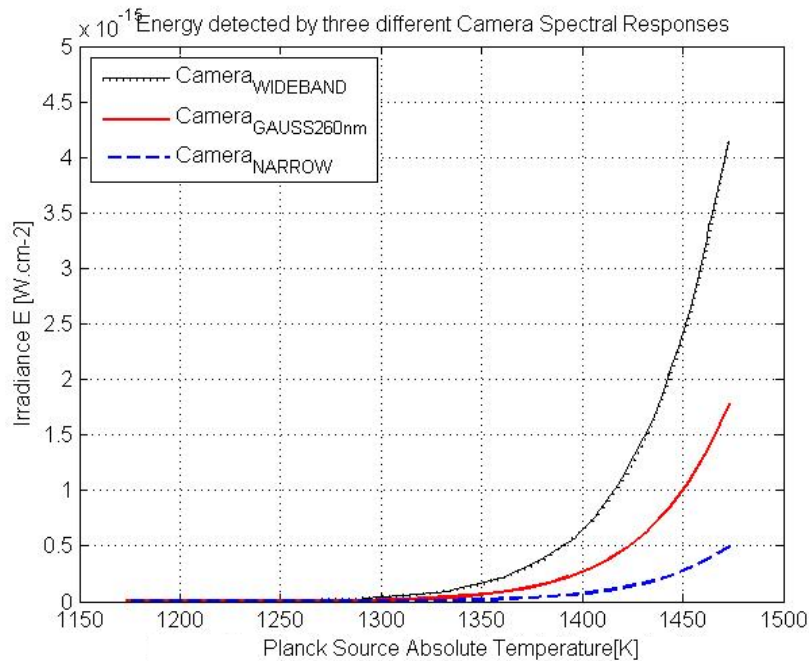
Figure 2.3. Planck source energy input versus lens input energy.

Results in **Figure 2.3** shows that less energy is detected by the gauss and narrowband spectral transfer function. The results imply that the hypothesis of the influence of the camera's spectral response seems to be possible.

2.2.2   Measuring the spectral transfer function of a camera

The spectral transfer function (response) of a camera as modelled in the previous section can be determined by a monochromator and a reference detector [6]. A monochromator is a wavelength selectable (adjustable) source [6]. A UV monochromator uses a wideband source in conjunction with an optical grating to produce a limited narrow band of wavelengths [19]. A Czerny-Turner type monochromator is ideally suited for characterizing solar-blind UV [19].

The procedure for characterising solar-blind cameras is as follows:

1. The monochromator's output is set to produce a particular wavelength output resolution (or output bandwidth), which could be narrow or wide.
2. The output energy of the monochromator is measured by a calibrated detector at a number of wavelengths at which a camera's spectral response needs to be determined. The calibrated detector's spectral and energy response is known, which implies that the actual output energy of the monochromator can be determined at each selected wavelength.
3. Values obtained from the previous step are noted and stored as calibration (correction) factors for a later step.
4. A solar-blind UV camera's (or detector's) response at each wavelength is then noted, using the same wavelength-intervals and monochromator bandwidth setting used in step 2.
5. The values obtained from the calibrated detector are then used to correct the values of the solar-blind UV camera, producing a spectral response.

The solar-blind camera investigated uses an image intensifier detector, which energy measurement is popularly defined in terms of photon count or Detective Quantum Efficiency (DQE) measurements as done by Bergamini *et al*. [6]. The spectral response of a camera is defined in terms of Quantum Efficiency (QE) or DQE, which is the percentage of source energy detected at a particular wavelength. A camera's spectral response is not the only influence on the optical flux (energy) measurement. The UV source that is observed by the solar-blind camera also has a particular source spectrum, which is discussed in the next section.

2.3   SOURCE AND ENVIRONMENT

2.3.1   Sources

Any optical source can be described by Planck's Radiation Law in terms of a temperature T [17, 18]. The description is the energy radiated from a source at each wavelength, known as the spectral emittance M_λ (energy from the source) (Appendix A.2), which is

$$M_\lambda(T) = \grave{o}_\lambda \frac{2\pi hc^2}{\lambda^5\left(e^{\frac{hc}{\lambda kT}}-1\right)} \quad \left[\frac{\text{W}}{\text{m}^3}\right].$$

(2.4)

where

$M_{\lambda W}(T)$ is the spectral emittance from a Plank source $[\text{W.m}^{-2}_{SourceArea}.\text{m}^{-1}_{wavelength}]$,

$\grave{o}_\lambda$ is the ratio of an actual source's $M_{\lambda W}$ to the $M_{\lambda W}$ of an ideal Planck source as a function of λ,

T_o is the absolute temperature for a source in Kelvin [K] or Celsius [°C],

h is the Planck constant which is 6.626176×10^{-34} [J.s],

c is the well-known speed of light in a vacuum 2.997924580×10^8 $[\text{m.s}^{-1}]$,

k is the Boltzman constant 1.380662×10^{-23} $[\text{J.K}^{-1}]$,

and

λ is a wavelength [m].

The total emittance for a UV source using the energy per nanometre wavelength [nm] (for each $d\lambda$), derived from (2.4), can be described by the relation

$$M(T_{\text{A Kelvin}}) = \int_0^{\lambda_{END}} \grave{o}_\lambda \frac{3,7418\times10^{20}}{\lambda^5\left(e^{\frac{14387863,142}{\lambda T}}-1\right)} \quad d\lambda \quad \left[\frac{\text{W}}{\text{m}^2_{area}}\right],$$

(2.5)

and similarly the total photon emittance [17] from a Planck source is

$$M(T_{\text{A Kelvin}}) = \int_0^{\lambda_{END}} \grave{o}_\lambda \frac{1.88365\times10^{36}}{\lambda^4\left(e^{\frac{143878861,058}{\lambda T}}-1\right)} d\lambda \quad \left[\frac{\text{q.s}^{-1}}{\text{m}^2_{area}}\right].$$

(2.6)

Stefan-Boltzmann's Law [17] can be used to verify models that use relations (2.5) and (2.6) for an ideal source where the emissivity is 1. It sums the total source emittance for all wavelengths with

$$M(T) = \sigma_e \times T^4 = 5.67033\times10^{-8}\times T^4 \quad [\text{W.m}^{-2}],$$

(2.7)

or

$$M_q(T) = \sigma_q \times T^3 = 1.5204\times10^{15}\times T^3 \; [\text{q.s}^{-1}.\text{m}^{-2}].$$

(2.8)

Figure 2.2 illustrates the energy transmitted for three ideal sources, each with different absolute temperature values (*T*). The graphs created from relation (2.5) were created with the software Matlab [20]. Furthermore, **Figure 2.2** illustrates the area graphically for one of the three sources as interpreted by Stefan-Boltzmann's Law.
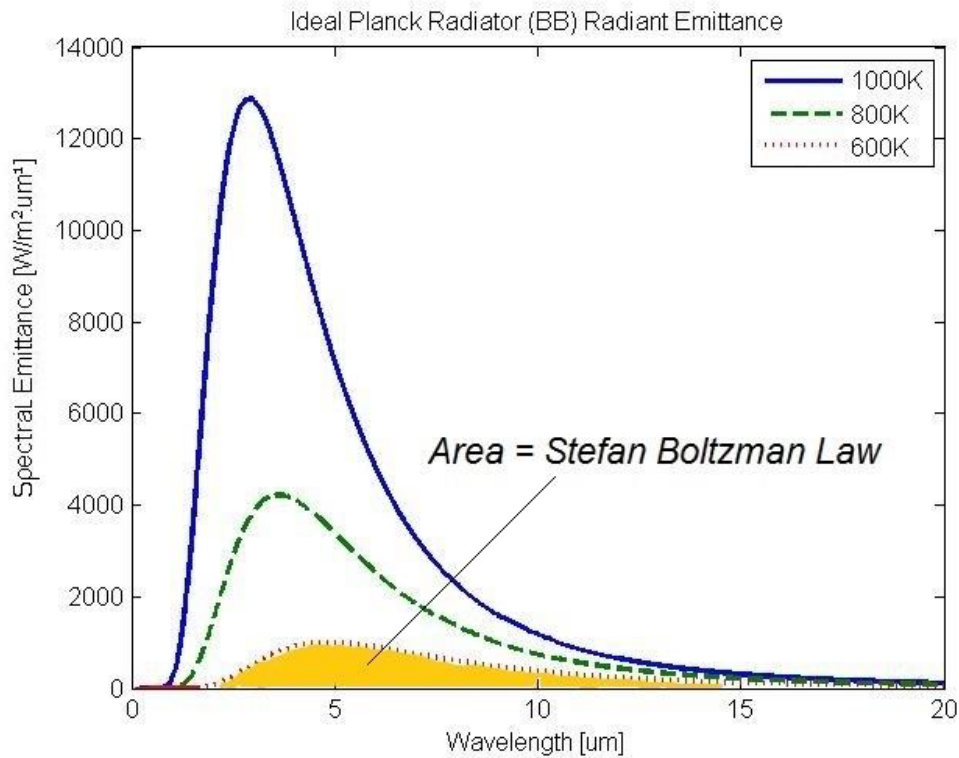
Figure 2.4. Planck source energy input versus lens input energy.

2.3.2 Atmosphere

The optical flux from a source that reaches a camera is not only reduced by the distance square law as implied by (2.2) and (2.3) , but also absorbed and scattered by aerosols and molecules in the atmosphere [15-17, 21, 22]. Each wavelength is differently affected by the atmospheric gas composition and state [17, 22]. Software packages such as Lowtran, MODTRAN and LibRadTran can be used to simulate different atmospheric compositions and the attenuation of each wavelength through the atmosphere [17, 22].

The attenuation attributed to the atmosphere can be summarily described by Pierre Bouquer's Law of 1792 (Essai d'optique sur la gradation de la lumière) [16, 17], which is alternatively known as Beer-Lambert's law (an atmospheric transmittance) that is described by

$$\tau_{A\lambda}(r) = e^{-\gamma_\lambda r} \tag{2.9}$$

with

$\tau_{A\lambda}$ the atmospheric transmittance at each wavelength (0 to 1),

r the distance between a camera and source [m],

and

γ_λ the atmospheric attenuation at each wavelength [m^{-1}].

Note that equation (2.9) is often adapted to describe the transmittance of a group of wavelengths that a camera measures as is done by Willers [17] using the symbol α instead of γ using a "range equation". In this study γ_λ indicates the attenuation for a single wavelength and $\gamma_{effective}$ for a band (group) of wavelengths that is determine by the camera's spectral bandwidth that is measuring a source. **Table 2.1** presents a comparison of practical attenuation values from solar-blind UV cameras and one UVB type camera.

Table 2.1. Typical $\gamma_{effective}$ atmospheric attenuation values

No	Centre wavelength	$\gamma_{effective}$	Case
1	Not applicable	0	No atmosphere.
2	UVB 300 nm	0.3 to 0.5	Wideband Electron Multiplying CCD (EMCCD) observing a gas discharge at a UVB wavelength [23].
3	UVC approx. 270nm , Bandwidth 260 - 280 nm	0.07	Electrical discharge [24, 25]. This case needs further investigation as it does not use true radiometric type processing for the camera.
4	UVC 270 nm	1 to 1.2	Missile detection system [1].
5	UVC (unknown)	1 to 1.1	Missile detection system [4].

2.3.3   Effect of distance between source and camera

The previous paragraph described that the optical flux (energy) from a source reaching the camera is depleted by the atmosphere and also distance as described by relations (2.3) (section 2.2.1) and (2.9). A solar-blind camera thus needs to perform additional processing dubbed here as *scaling* to determine the energy of the source, taking the distance and atmospheric attenuations into consideration. The scaling of a measurement by the camera based on the information presented here, is determined by:

- The UV source's particular spectral bandwidth.

- The camera's spectral transfer function (section 2.2.1).

- The atmospheric influence.

The distance between source and the camera is easily obtainable by range finders that operate with lasers, or other methods such as the focal length of a camera's optics for a particular observation. To determine value of γ_λ is somewhat more challenging as it forms part of relation (2.3), which is embedded within the integral. One of the methods to determine the atmospheric attenuation for camera and source is by using measurements of at least two or more different distances. The atmospheric attenuation for a narrowband camera and source case can be obtained by division of measurements, which yields

$$\gamma_\lambda = \frac{-1}{R_A - R_B} \left[\ln\left(\frac{R_A}{R_B}\right)^2 + \ln\left(\frac{X_\lambda(R_A) - w_{Offset}}{X_\lambda(R_B) - w_{Offset}}\right) \right] \quad \left[m^{-1} \right] \tag{2.10}$$

with

$X_\lambda(r)$ the source energy measured at a distance r in terms of

L the radiance $\left[W.m^{-2}.sr^{-1} \right]$, E the irradiance $\left[W.m^{-2} \right]$ or I intensity $\left[W.sr^{-1} \right]$,

r_A and r_B the two different distances between the source and camera $\left[m \right]$,

γ_λ the attenuation coefficient for a particular wavelength $\left[m^{-1} \right]$,

$X(0)$ the actual source energy at distance 0,

and

w_{Offset} the offset attributed to factors such as noise and temperature.

An alternate approach similar to relation (2.10) is to determine $\gamma_{effective}$ effective atmospheric attenuation for the wideband case [17]. Furthermore, the atmospheric attenuation and distance are not the only aspects (or factors) that influence the solar-blind camera's measurement [16]. Internal components and the operation of the camera need to be considered as part of a measurement, which is the focus of the overview of the solar-blind UV camera's internal operation provided in the next section.

2.4   DESCRIPTION OF A TYPICAL SOLAR BLIND UV CAMERA

2.4.1   Objective

This section introduces the typical solar-blind camera components that translate the solar-blind UV energy from a source to an electrical signal for measurements. The objective of this section is to facilitate a basic understanding of the solar-blind camera's operation.

2.4.2   Overview

Figure 2.5 conceptually illustrates the UV components of the solar-blind camera's UV channel investigated [2]. The figure depicts a UV source (target) detected through a set of optics represented by a simplified lens. The lens and image intensifier have a wideband spectral response, which implies that a set of filters are required to enable the detection of solar-blind UV. The solar-blind UV light enters the image intensifier at the photocathode where it is converted to electrons in a vacuum. Amplification of the electrons is achieved by one or two Micro Channel Plates (MCP) with a honeycomb type structure [5]. The electrons hit a phosphor screen at the end (anode) of the image intensifier. The excitations by the electrons on the phosphor screen are visible within the visible wavelength spectrum. Phosphor images are relayed from the anode via fine fibre optic bundles or lens assembly to a Charge Couple Detector (CCD). This type of camera is often referred to as an Image Intensified CCD (IICCD) or Intensified CCD (ICCD) [5]. There are various pros and cons associated with the use of a fibre optic- or lens assembly in the final pre-CCD stage [5].
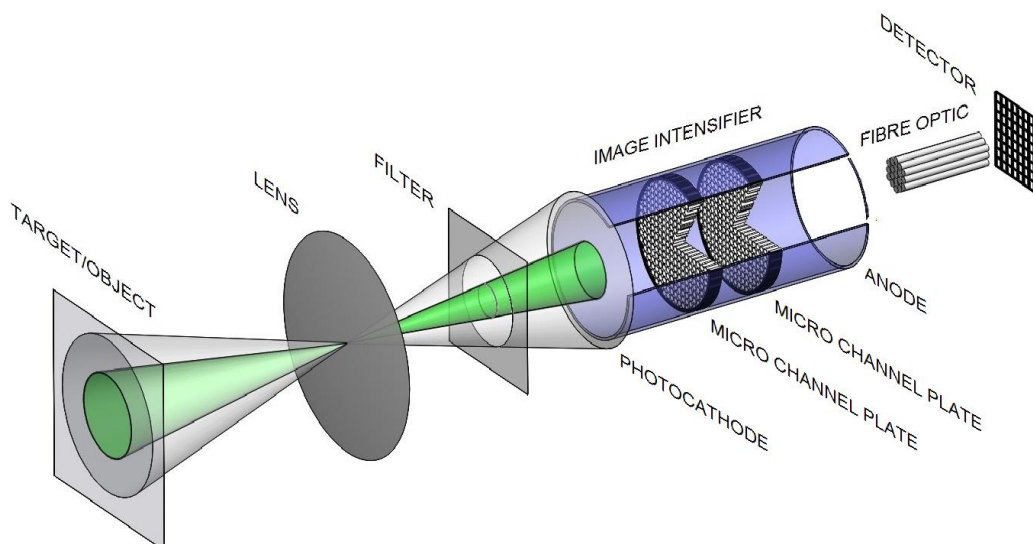
Figure 2.5. A typical Image Intensifier Charge Coupled detector camera.

2.4.3 Camera images and processing

Figure 2.6 illustrates the typical differences between CCD- and IICCD type camera images. The left hand illustration of **Figure 2.6** shows a CCD type camera's image, with processing required on each pixel of the image to determine the energy level of a source. Images of the IICCD solar-blind UV camera as illustrated on the right hand figure of **Figure 2.6**, typically appear as discontinuous pixel images or blobs. These blob type images are more appropriately measured in terms of photon counts if the source constitutes a single wavelength. However in case where the source is wideband and the camera has a wide spectral transfer function the measured count value should be presented in the form of irradiance with the units [W.m^{-2}] as argued later in par.2.5.3. To achieve counting the image is divided into *sectors* as shown in the right hand figure with 5×5 pixels [6, 7]. A count of the number of blobs is performed for each of the pixel sectors to measure the optical flux [4].
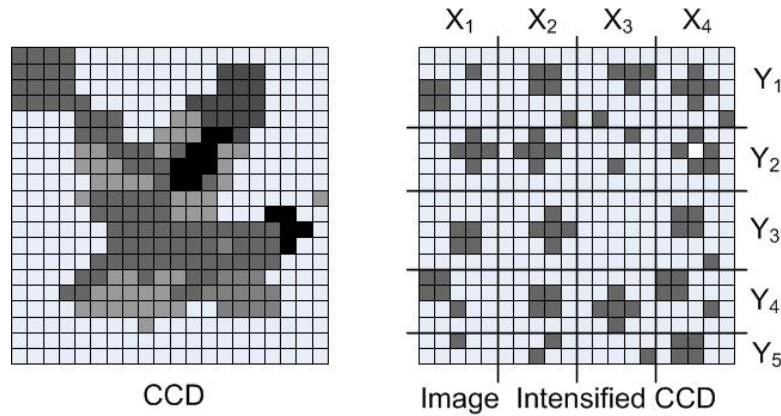
Figure 2.6. Image differences between CCD and IICCD detectors.

The energy or Irradiance E on the ICCD can be derived from (2.1) to determine the energy detected by the camera here with an approximation in terms of counts per second as

$$E_{MEASURED}(\lambda) \approx \sum_{i=0}^{\text{Total sectors}} \frac{\phi_{Ri}(f).N_{Ri}(f)}{a_i} \; \left[\text{W.m}^{-2}\right], \tag{2.11}$$

where

$\phi_{Ri}(f)$ is the event count transfer function of a sector on the image plane $\left[\text{counts}/\text{s}\right]$,

$N_{Ri}(f)$ is the correction factor for a particular sector $\left[\text{W.s.counts}^{-1}\right]$,

and

a_i is the area for the particular associated pixel sector $\left[\text{m}^2\right]$.

The correction factors in relation (2.11) are associated with a particular sector which is related to a portion of a UV source as it is projected through the atmosphere, lens, intensifier and optic fibre

upon the final CCD image of the ICCD (**Figure 2.5**). Corrections of (2.11) is also a function of the lens design, which is discussed next.

2.4.4   Lenses

2.4.4.1   Overview

Energy from an ultraviolet source is decreased by the atmosphere and arrives through a set of optics through the filter(s) upon the input of the image intensifier of the solar-blind camera (**Figure 2.5**). The three methods to determine the lens transfer function (UV source to image intensifier input mapping) briefly explored within this section, are as follows:

- The *thin lens* description[27]

- *Polynomials*.

- *Computer Vision* which is related to lens design using Geometric optics [19, 28, 29].

2.4.4.2   Thin Lens presentation

Figure 2.7 depicts an idealistic thin lens model that is used to create a mapping of the optical flux from a source through a lens incident on the image intensifier [27]. The figure illustrates a flat ultraviolet source (object plane) that transfers optical flux through a lens onto the image plane, which in this case study is the intensifier input of **Figure 2.5**.
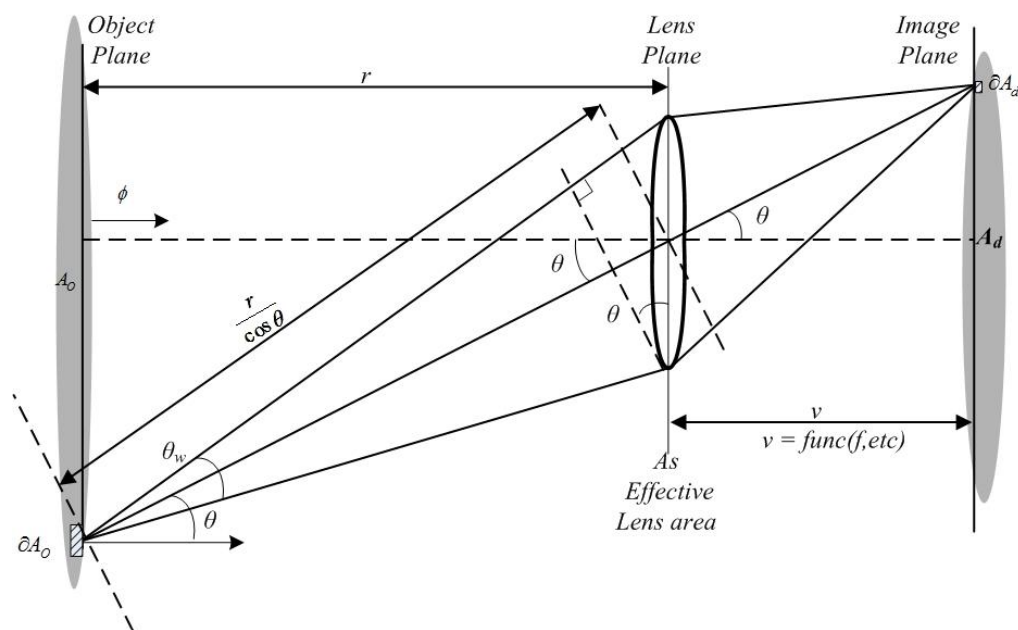
Figure 2.7. Simplified Lens transfer, adapted from [27].

The optical flux for each wavelength of the source that arrives on a portion of the image plane (intensifier input) as derived from Jacobson *et al.* [27] and Willers [17] is described by

$$\partial\phi_\lambda = \pi\ \partial A_O \tau_{A\lambda} \tau_S \grave{o}_\lambda L_\lambda \left[\frac{\cos^4\theta}{4 \times F_\#^2 \left(1 + M_R\right)^2} \right] \partial\lambda + \phi_{CAMERA\_STRAY\_FLUX} \qquad \left[\text{W.nm}^{-1} \right] \tag{2.12}$$

where

$\partial\phi_\lambda$ is the flux density on a small area of the image plane in terms of $\left[\text{W.nm}^{-1} \right]$ or $\left[\text{q.s}^{-1}.\text{nm}^{-1} \right]$,

$\grave{o}_\lambda$ is the emmisivity with values 0 to 1,

L_λ is the spectral Radiance $\left[\text{W.m}^{-1}.\text{sr}^{-1}.\text{nm}^{-1} \right]$,

∂A_O is a portion area of the source area $A_O \left[\text{m}^2 \right]$,

$\tau_{A\lambda}$ is the atmospheric attenuation for each particular wavelength,

τ_S is the system transmittance ($\tau_{FILTER} \times \tau_{LENS}$), which scales the energy at each wavelength,

r is the distance between the camera lens input and source $\left[\text{m} \right]$,

θ is the angle at which of energy projected from a flat source as shown in the figure,

$F_\#$ is the lens number ,

and

M_R is the reduction factor from source to image plane.

The optical flux detected on the camera's image intensifier input as described by (2.12) is referred to as the $cos^N\theta$ effect or shape [22, 27]. Relation (2.12) thus describes a radial distortion upon the solar-blind UV camera's image intensifier input. Within relation (2.12) the influence of the distance (*r*) between a source and the camera forms a part of M_R, the reduction factor according to the thin lens description [27]. Furthermore, note that a summation of (2.12) must be performed across the entire image intensifier input area to attain a radiometric measurement, which is similar (but not identical) to the description (2.11).

2.4.4.3 Polynomials

The lens map (transfer function) can also be derived by observing a point source as shown in **Figure 2.8**, using polynomials [4]. Polynomials are used in some cases where the exact lens map is unknown [4, 30]. Polynomial coefficients are determined during the observation of a small or point source as shown with the assembly of **Figure 2.8**. Such a polynomial fit is a power series with coefficients x_i and observation angle θ (θ of **Figure 2.8**) from Wu *et al.* [30], which is

$$f_N(\theta) = x_1\theta + x_2\theta^3 + x_3\theta^5 + x_4\theta^7 + x_5\theta^9 + ... \tag{2.13}$$

Figure 2.8. shows that four polynomials can be used to create a lens map of a complex lens assembly by dividing it into 48 sectors, with each sector which has a unique correction factor (refer

to **Figure 2.6**). Furthermore, the number of sectors is related to the number of polynomials used for a particular solar-blind camera. Note that the mechanical arrangement shown is restricted to cameras with a narrow field of view (FOV). Also note that the distance between source and camera needs to be incorporated into the polynomial relation, which could be computationally intensive. Computer vision as alternative for lens mapping is briefly discussed in the next section.
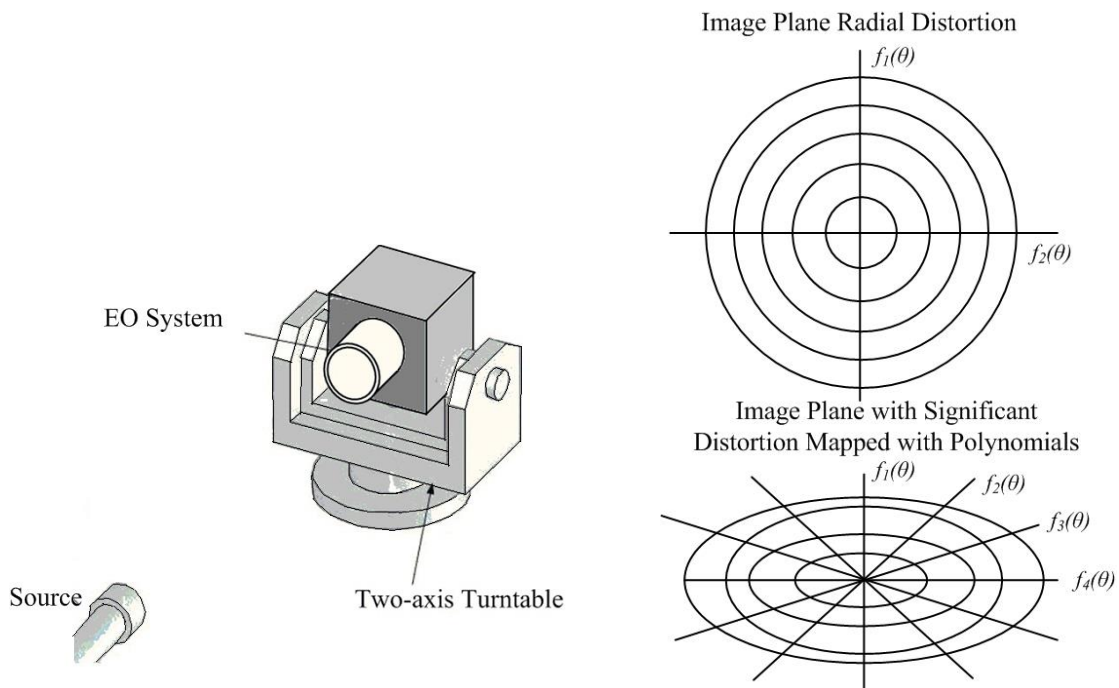
Figure 2.8. Narrow Field of View Characterisation from [30], with the additional figures that describe how image sectors are created using polynomials.

2.4.4.4 Computer Vision

The proposed relation (2.11) based on the operation of other similar solar-blind ICCD cameras implies that a camera must convert a count for each sector to a E [W.m^{-2}] value. Furthermore the imperfections across the lens for ICCD type cameras as found by those using count techniques (paragraph 2.5) is not the only factor that must be considered. Additional factors are:

- Corona discharges sources have non-uniform three dimensional shapes that need to be determined for purposes of determining the related optical flux and electrical loss.
- The electronic processing in ICCD type of cameras use devices such as FPGAs and Graphic Processing Units (GPUs) that performs optimally with matrix operations.

Fortunately the design and analysis of the lenses of a camera can be performed with matrixes [19, 28]. Similar to lens design with matrixes and three dimensional processing of objects is the field of

computer vision which also uses matrixes [28]. Computer vision if correctly applied can be used as an alternative to the classic relation (2.12). An example is Sentenac *et al*.[31], who used Computer vision principles for infrared wavelengths for radiometric measurements. Equation (2.14) is an introduction to the Computer Vision relation of a source with X, Y and Z coordinates as it translated through a number of lenses to the detector with the coordinates x_i and y_i [28]. This is referred to as a pipelined transformation which consists of a number of matrix operations according to Nielsen [29], which can be combined into a single matrix such as

$$\begin{bmatrix} x_i \\ y_i \\ z_i \\ 1 \end{bmatrix} = \begin{bmatrix} p_{11} & p_{12} & p_{13} & p_{14} \\ p_{21} & p_{22} & p_{23} & p_{24} \\ p_{31} & P_{23} & p_{33} & p_{34} \end{bmatrix} \begin{bmatrix} X_i \\ Y_i \\ Z_i \\ 1 \end{bmatrix} \text{, or in a condensed matrix form } \underline{x} = \underline{P} \ \underline{X} \tag{2.14}$$

where

X_i, Y_i, Z_i is part of the source coordinates,

P is the forward transformation matrix unique for each camera,

and

x_i, y_i, z_i is the image coordinates.

2.4.5 Filters

In addition to the lens transfer function influence, is the optical filter between the image intensifier and lens of the solar-blind camera (**Figure 2.5**) that reduces the energy by filtering wavelengths. Filters of solar-blind UV cameras are typically made of materials such as Gallium Oxide [32]. The filter transfer functions of seemingly identical cameras differ due to manufacturing tolerances [4,13]. The transfer function is best determined by measurement with an instrument such as a Spectrometer [33]. A typical description of a filter is described by Willers [17] as

$$\tau_f(\lambda) = \tau_S + \tau_P \exp\left[-\left(\frac{2(\lambda - \lambda_C)}{\Delta \lambda}\right)\right] \tag{2.15}$$

where

$\tau_f(\lambda)$ or τ_{FILTER} is the filter transmittance with the values 0 to 1,

τ_S is the transmittance in the filter's suppression range,

τ_P is the peak transmittance in the filter's pass-band range with the values 0 to 1,

λ_C is the center wavelength value in the filter's pass-band range [nm],

$\Delta \lambda$ is the width of the filter's pass-band [nm],

and

s is the filter shape, which is ∞ for a square shaped filter and 2 for a gauss shape filter.

2.4.6   Image Intensifier and detector related components

The UV source energy leaving the filter enters an Image Intensifier as introduced in **Figure 2.5**. The image intensifier operates in conjunction with a Charge Coupled Detector for the particular solar-blind camera studied, which is referred to as an image intensifier CDD (IICCD) configuration, used for solar-blind UV imaging applications [14, 34]. The advantage of the image intensifier technology is the excellent noise immunity, the fact that it is hindered less by temperature fluctuations and extremely low optical signal detection [34]. The general characteristics and operation of image intensifiers can be summarized as follows:

- The photocathode (input) of an image intensifier in the case of solar-blind UV consists of UV sensitive materials such as Cs_XTe (Cesium telluride) or CsI (Cesium Iodide) [35].

- The quantum efficiency (QE) or energy throughput through the image intensifier for UV is approximately 10% [36].

- Image intensifiers' wavelength responses are wideband, which implies that filters must be used as shown in **Figure 2.5** [2,4,14]. A filter will reduce the overall QE of the camera even further.

- The Micro Channel Plate (MCP) amplifies (by acceleration) the electrons in the image intensifier, thereby amplifying faint optical signals. The typical description for the image intensifiers gain [35] is provided by

$$G_{INTENSIFIER\_MCP} = e^{G \times (l/d)} \tag{2.16}$$

with

  $G_{INTENSIFIER\_MCP}$ the image intensifier gain,

  G the Gain factor related to the image intensifier type,

  l the length of the MCP pores (channels),

  and

  d the diameter of the MCP pores or channels.

- According to other intensifier studies the angled channels MCP's in a Z stack configuration have a deteriorating gain performance over time, as the channels are worn out by electron scrubbing. This implies a limited lifespan, requiring recalibration over time [37, 38].

- The type of phosphor material on the output anode of the image intensifier has an influence on the camera's time response [39].

- The MCP's "dead time" response for a particular image intensifier also influences a camera's time response[5], which is described by

$$t_d = \frac{\text{output charge per MCP channel}}{\text{strip current per MCP channel}} \quad [\text{s}]. \tag{2.17}$$

From other studies it appears as if the values of t_d are smaller for image intensifier with a larger gain [37, 39]. This implies that fast events could be missed in some cases.

2.4.7   Camera Dynamic Range

From personal experience with infrared and ultraviolet cameras it seems as if the minimum and maximum energy that can be detected by a camera is dependent on the type of CCD technology. In this particular case the image intensifier operation limits the dynamic range [39]. The minimum and maximum detectable energy of a camera similar to other electronic systems is defined in terms of dynamic range [27]. Joseph [40] implies in a summary of different Ultraviolet detectors that image intensifiers have a very low dynamic range. Dynamic range for the solar-blind UV energy measured by a camera, is similar to photography where an image can be over- or under -exposed [1, 29]. The dynamic range (DR) description for a detector [27] is described by the relation

$$DR_{\text{DETECTOR}} = 20\log\left[N_{e'\,full\_well} \div n_{RMS} \right] \, [\text{dB}]. \tag{2.18}$$

where

  $N_{e'\,full\,well}$ is the full well value (maximum) of the detector usually with the units electrons,
  and

  n_{RMS} the root mean square of the noise.

The full (or total) dynamic range of a camera [27] in terms of a digital level, with the unit bits, can be described with the equation

$$DR_{\text{Camera}} = \log\left(2^{\text{maximum measured bits}} / 2^{\text{noise level in bits}} \right) \quad [\text{dB}]. \tag{2.19}$$

The noise level as part of the DR of a camera can be determined by capturing images from a non-emitting reference source, such as a non-reflective surface. Dynamic range can be determined from reference calibration sources, using statistical histograms [29, 41, 42]. But the DR of the solar-blind camera can only be determined if its particular measurement output (counting) is understood. The subsequent section therefore provides an outline of the operation of the count mechanism.

2.5   COUNT MECHANISMS

2.5.1   Introduction

Solar-blind cameras with an ICCD as mentioned earlier (section 2.4.6) observe blobs or events. This is due to the dead time response of the image intensifier as described by (2.17)[5], including the phosphor type material at the cathode [39]. Not all the researchers and the manufacturers of solar-blind UV ICCD cameras use the known radiometric photon counting techniques when observing electrical phenomena [13, 24]. This section therefore provides an overview of photon counting, also referred to as event counting.

2.5.2   Analogue measurements versus count method

The solar-blind camera's IICCD images can be interpreted with an analogue or event counting method according to intensifier manufacturers [35, 36]. The output level of the image intensifier is unfortunately sensitive to the voltage controlling the image intensifier, which is the reason for the preference of photon counting techniques by image intensifier type camera manufacturers [35]. The particular solar-blind UV camera investigated in this study utilizes a proprietary analogue and count algorithm, which was developed for imaging and not for true UV radiometric measurements.

2.5.3   Event counting versus photon count

Photon energy p_q according to textbooks [18] is described by the relation

$$p_q = \frac{hc}{\lambda} \qquad [\text{J}]. \tag{2.20}$$

The energy of each photon is thus related to wavelength, which introduces measurement inaccuracies when the solar-blind camera's spectral response is unknown. A similar dilemma occurs if the source spectrum is unknown. It can thus be concluded that the term photon counting can only be used if the camera's spectral transfer function is known and if the camera is calibrated. This study thus rather refers to the term event counting, as the experiments are conducted on an un-calibrated camera.   As the solar-blind camera investigated is not truly calibrated, the manufacturers of the solar-blind camera for electrical applications consequently adapted the datasheets from photon count to event count in 2012. As a result of this and other related shortcomings as later noted in Chapter 3, a number of adaptations had to be made to the solar-blind camera experimental data processing. The correct measurement unit would be radiance or irradiance which implies a wideband measurement.

2.5.4   Typical event/photon count

For the purpose of implementing a successful count algorithm, the events (counts) must be characterised in terms of pixel dimensions, which is the x and y size [6]. The phosphor on the image intensifier anode causes a Point Spread Function of which the centre must be located. **Figure 2.9** shows an actual typical event and associated distortion during characterisation by Bergamini. *et al.* [6]. Characterisation (profiling) of events in terms of Full-Width-at-Half-Measure (FWHM) is described by P. Bergamini *et al.* [6], with the smallest possible FWHM of one pixel [39]. The FWHM according to P. Bergamini *et al.* [6] could be asymmetrical due to the MCP's conductive channel construction. This asymmetrical profile was proven by P. Bergamini *et al.* [6] for another camera with an IICCD which MCP has a Z stack channel structure.
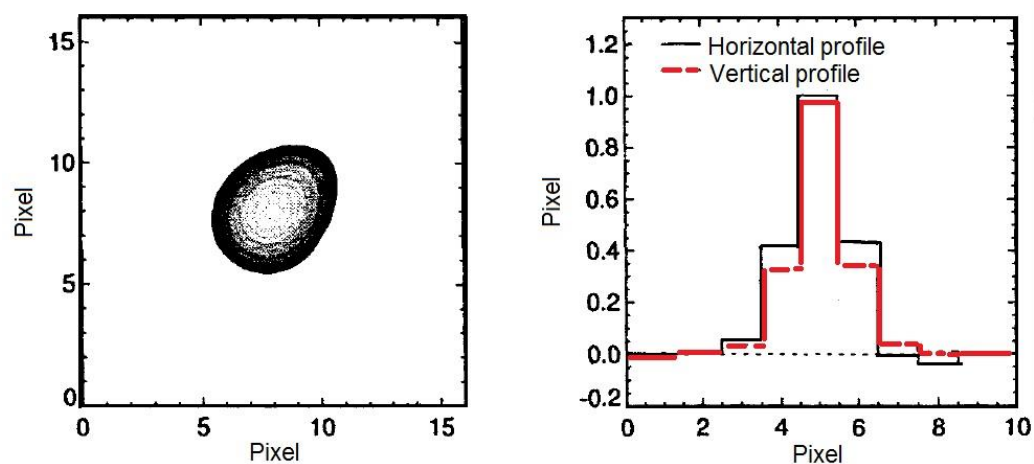
Figure 2.9. A result of event profiling from [6].

2.5.5   Algorithms

Centroiding algorithms objective is to find the location of the count event on the image plane [7], thereby determining to which sector (**Figure 2.6** and **Figure 2.8**) a count belongs. A variety of algorithms can be used, such as the Centre of Gravity (COG), Gaussian, Parabola, Lorentzian and finally the Hyperbolic Cosine as summarized by Suhling *et al.* [8].

The COG algorithm as an example for a 5×5 sized pixel event as shown by **Figure 2.10** is the easiest that can be implemented in electronic digital hardware such as a Complex Programmable Devices (CPLD) [6, 7] or a Field Programmable Gate Arrays (FPGA). A COG algorithm can be described as two processes running concurrently in the x and y direction on the image plane with the goal to determine the center of an event (blob). The center can be determined for a 5x5 FWHM

by five pixels referred to as A, B, C, D and E as done by Bellis *et al.* [9], Fordham *et al.* [39] and Bergamini *et al.* [6]. The COG in the X and Y direction can be described by the relation

$$\text{COG}_{\text{CENTRE}} = (2 \times A + B - D - 2 \times E) / (A + B + C + E) = M / N .$$ (2.21)

The variables M and N of (2.21) can be calculated separately as first step. Next M and N can be and divided using a lookup table [6, 9]. The COG for the X and Y directions using (2.21) are

$$X_{COG} = (2 \times A_3 + B_3 - D_3 - 2 \times E_3) / (A_3 + B_3 + C_3 + E_3) ,$$ (2.22)

and

$$Y_{COG} = (2 \times C_1 + C_2 - C_4 - 2 \times C_5) / (C_1 + C_2 + C_4 + E_5) .$$ (2.23)

The event centre once identified can be assigned to a specific image sector for counting.
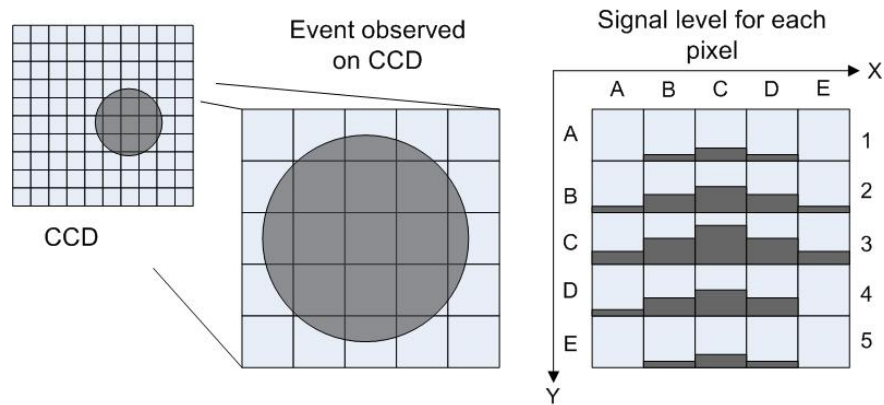
Figure 2.10. A 5x5 event based on the figures of [7].

There is a relation that describes the counting for a sector of a camera image (**Figure 2.6** and **Figure 2.8**) by using a statistical Poisson distribution (*s curve shape*) [43, 44]. The particular s-curve shaped description has a lower and upper threshold as provided by Dainty *et al.*[43], which is described by the statistical type equation

$$\phi_{Ri} = T_{UX} \left(1 - \left[\frac{1}{T_U} \left(\sum_{k=0}^{T_L-1} \frac{\phi_I^k}{k!} + \sum_{k=0}^{T_L} \frac{\phi_I^k}{k!} + \sum_{k=0}^{T_L+1} \frac{\phi_I^k}{k!} + ... + \sum_{k=0}^{T_U+T_L-1} \frac{\phi_I^k}{k!} \right) \right] e^{\phi_I} \right)$$ (2.24)

with

ϕ_{Ri} the event count for the entire detector for a point source [count.s^{-1}],

  or for a larger source [count.s^{-1}.m^{-2}] ,

ϕ_I the input source flux for a point source [count.s^{-1}] or larger source area [count.s^{-1}.m^{-2}] ,

T_{UX} upper limiting threshold for a single point source [count.s^{-1}] or for a

  large uniform source [count.s^{-1}.m^{-2}],

and

T_L lower noise or system threshold for a point source [count.s] or [count.s^{-1}.m^{-2}] .

Contrary to the previous descriptions of (2.24) is the experimental data of Bergamini *et al.* [6], which produce third order polynomial relations, if curve-fitting is applied to the data. Bergamini *et al.* [6] results approximate other exponential count descriptions by Fordham *et al.* [39]. **Figure 2.11** provides a comparison of relation (2.24) and Bergamini *et al.* [6] results. The transfer function (statistical or a polynomial) can be utilised for the entire image or each sector (**Figure 2.6** and **Figure 2.8**) on an image. The upper thresholds (T_{UA} and T_{UC}) that describe the transfer functions are determined by the frame rate. A coincidence level or threshold on each transfer function is a particular value where events (counts) start to overlap with each other, making counting difficult. Fordham *et al* [39] and Carter *et al.* [11] attempted to provide solutions for solving coincidence (overlap). Boksenberg *et al.* [7] subtracts a "calibration frame" from their results, which is the noise threshold or background. This slight deviation or uncertainty is indicated in **Figure 2.11** as a *band of results*, which is as result of the Electronic Background Interference (EBI) and the anode phosphor time response variation [35, 36].
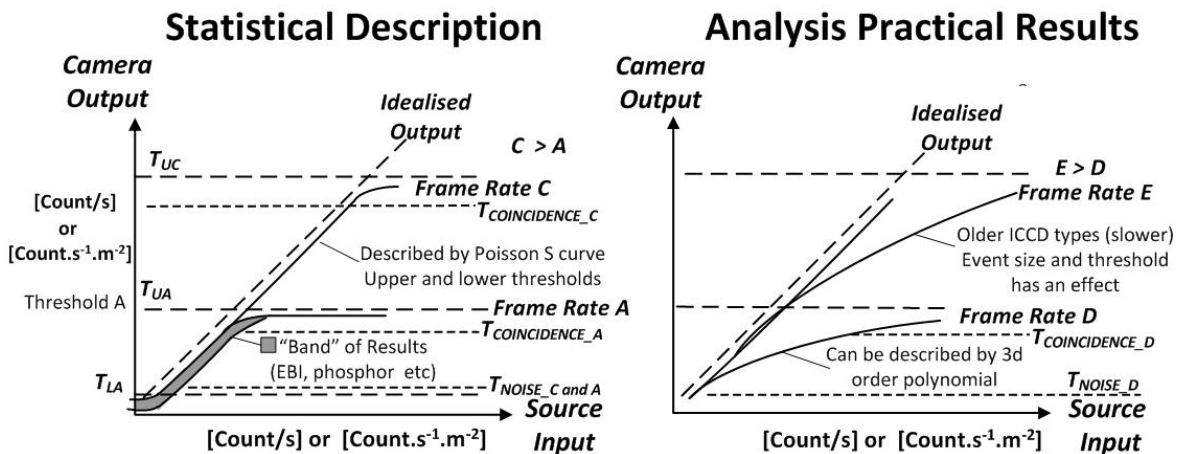
Figure 2.11. Summary of event count transfer functions compiled from [6], [7] and [43].

An alternative description similar to the description of (2.24) was found to be

$$\phi_S = T_{UX}\left(1 + T_L e^{S_{SYS}\phi_I}\right)^{-1}$$ (2.25)

with the postulated inclusion of a system transfer function S_{SYS}. This system seems to be similar to the models presented by Fordham *et al.* [39].

This concludes an abstract of the information investigated with regards to the internal operation of the solar-blind UV camera. The next section provides an abstract in the form of a condensed summary of the investigations of the particular and similar solar-blind cameras used in the high voltage electrical field.

2.6   HIGH VOLTAGE INDUCED CORONA: AN ABSTRACT OF STUDIES ATTEMPTING TO FIND THE RELATION BETWEEN ELECTRICAL LOSSES AND THE OPTICAL FLUX DETECTED BY A CAMERA

The solar-blind UV camera investigated is used to inspect High Voltage Transmission (HVT) lines and equipment [45]. Defects in HVT components as well as unwanted substances (i.e. dirt, salt, pollution and bird droppings) produce unwanted ground return paths, resulting in corona emissions. Corona emissions can lead to progressive damage of HVT components and loss of electrical energy. The electrical energy losses are converted to other forms of energy such as heat, radio frequency and optical emissions [45]. **Table 2.2** is an abstract from other investigations by the author identifying other researchers that attempted to find a relation between electrical corona loss and optical flux detected. These investigations implied that radiometric principles must first be understood before attempting to uncover the relation between electrical losses and optical flux.

Table 2.2. Highlights of HVT corona versus optical solar-blind UV energy studies.

No	Electrical test configuration	Optical flux parameters investigated	Radiometric processing?	Results
1	115kV insulator, Partial Discharge Test. [26]	Distance, Humidity	Uses intensity and background subtraction	Optical Intensity and electrical Partial Discharge (losses) related
2	Point to plane for AC and DC voltages [25]	Distance	Photon Number and own Intensity type processing	Effect of distance
3	Point to plane AC Voltage [24]	Distance	Use camera as is with counting	Effect of distance. Maybe relation between electrical and optical
4	Insulator [46]	ICCD pulse outputs	Pulses from a photo multiplier tube	The electric corona pulses coincide with optical pulses.

CHAPTER 3   DESCRIPTION OF EXPERIMENTS

3.1   OVERVIEW

This chapter describe the experiments to determine the spectral response of the solar-blind camera as it influences the radiometric measurements of a source. Other influences on the measurement are also investigated as part of the experiments.

This chapter consists of the following sections:

- An outline of the information used to develop the experiments.
- Limitations that had to be overcome.
- Descriptions of the experiments.

3.2   OUTLINE OF THE INFORMATION USED TO DEVELOP EXPERIMENTS

Experiments as described within this chapter were developed from the following:

- Rudimentary radiometric source to detector relations.
- Particular camera detector technology.
- Operational limitations of the solar-blind camera used.
- Limitations of the available equipment.
- Utilisation (practical application) of the solar-blind UV camera within the High Voltage industry.
- Other similar test configurations.
- Elementary models of infrared - and solar-blind UV cameras.

3.3   CAMERA CHARACTERISATION BASED ON THE RADIOMETRIC RELATION

3.3.1   Introduction

According to the simplified model and relation (2.3) in section 2.2.1, the UV irradiance detected by the camera is less than the actual source energy. This is because of the various influences such as the atmospheric attenuation and the camera's construction and design itself. A camera must therefore perform processing of the energy it detects to determine the actual energy at the source. Radiometric relation (2.3) which describes the energy that reaches the camera is used as a first

order approximation to identify factors (parameters) that form part of characterisation in the next paragraphs and during the experiments.

3.3.2   Determining the source energy

The simplified model of a solar-blind camera as described with relations (2.2) and (2.3) implies that the design and processing must be such that it can deduce the source energy (radiance L_λ) from the energy that it detects. During characterisation of a camera the objective is to determine how a camera processes (observes) a known source, revealing the camera's spectral transfer function S_λ. Source energy described in the form of spectral Radiance L_λ for each wavelength is defined as

$$L_\lambda = M_\lambda / \Omega \ , \tag{3.1}$$

with

M_λ the source spectral emittance [W.m^{-2}.nm^{-1}]

and

Ω the projected solid angle [sr^{-1}].

An ideal Planck radiator (Black-Body) source (section 2.3.1) used as part of the camera characterisation can be described by relation (2.5) or (2.6) energy in terms of spectral emittance M_λ with units [W.m^{-2}]. The emission from such a reference source is modelled with a flat surface, which emits half a spherical solid angle. This implies that the projected solid angle Ω of π [sr]. For the purposes of measurement and the camera characterisation, the energy upon the lens can thus be described by

$$E_{UPON\_LENS}(\lambda) = \int_0^\infty \frac{M_\lambda}{\pi} \frac{\partial A_{SOURCE}}{r^2} \tau_{A\lambda} . \partial \lambda \tag{3.2}$$

with units [W.m^{-2}].

Source energy is enclosed within the relation (within the integral), implying that the relation between camera measurements and actual source energy is best determined with numerical methods. A reference source is used to create a relation between camera measurement and source values, which can subsequently be used to measure an unknown UV source.

According to the simplified model as described by (2.2) and (2.3) variables such as the source area A_O , distance r must also be included as part of the processing to determine the source energy. The next sections discuss some of the variables which form part of the experimental investigation defined as a camera characterisation.

3.3.3   Source Area

The source area A_O is easily identified as a parameter that needs to be considered as part of the relation (2.3) to determine the source energy. Source energy doesn't form part of the integral, but it can be extracted from relations such as (2.2) and (3.2). These relations provide a simplistic perspective of a solution to determine A_O. The actual solution to find A_O requires more effort, as the lens mapping and the distance between the camera lens and the source must be taken into account [31, 47].

3.3.4   Distance

Relations (2.2) and (3.2) describing the UV source to camera translation, readily provides the distance as influence on measurements by a camera. Energy that reaches the camera lens is attenuated by a factor of r^2, thus implying that camera measurements must be increased by a factor r^2 to obtain the source energy. Similar to the source energy distance doesn't form part of the integral, implying that it can be extracted from relations such as (2.2) and (3.2)

3.3.5   Atmospheric attenuation

The atmospheric attenuation is another parameter that must be considered to determine the source energy as discussed in detail earlier in sections 2.3.2 and 2.3.3.

3.3.6   Spectral response

The spectral response of the camera similar to the source area (section 3.3.3), forms part of the integral, which implies that it should form part of the numerical solution to determine the relation between source and the camera measurement as mentioned in section 3.3.2.

3.4   LIMITATIONS

3.4.1   Limitations of the solar-blind UV camera investigated

The solar-blind camera investigated has the following operational limitations:

- Video output is an analogue output, which make processing difficult. The video output was only available in VGA format, which implies eight bit resolution.

- Effect of distance on measurements (counting) was not included as part of the camera processing, as proven by measurements done by Zang [24] and Zhou [25] on the camera.

- The camera doesn't have a command link messages that enables control from a personal computer (PC) for the purpose of energy measurements. This implies that the camera must be controlled by buttons which is time consuming.

- No automatic gain control mechanisms were incorporated in the design of the camera.

3.4.2   Limitations of the available equipment

The Planck source also referred to as a Black-Body (BB), has the following limitations:

- It is a wideband wavelength source which is not ideal for determining the camera's dynamic range. The BB spectral emissions deviates non-uniformly when it's absolute temperature T is adjusted, which in addition is also influenced by the spectral transfer function of a camera. The camera manufacturer for the particular found that different cameras non-radiometric measurements differed when a BB was observed at different BB values of T [13]. A simulation model proved that this is due to the variance of the various cameras spectral transfer functions. This can be corrected with calibration with a BB, but with limited measurement accuracy for an actual source which spectral content is not equal to a BB. This implies that a source that approximates the actual source must be used for calibration.

- The BB output aperture (source area) size is small in comparison with the camera's lens field of view. The normal practice in such case is to extend the source area as seen by a camera is with the use of a collimator or an integrating sphere [4, 17]. However neither was available at the time.

3.5   EXPERIMENTAL DESCRIPTIONS

3.5.1   General test configuration

The general test configuration is illustrated in **Figure 3.1**, with the solar-blind UV camera that observes a Planck source (specifications in A.4). In addition to this source a high energy tungsten lamp is used for focussing the camera for each experiment. The Planck source's output is circular, which size is adjustable with a rotary wheel with selectable apertures. Images from the camera are captured with an analogue frame capture card. The data is in a TIFF file format, which is a raw data format [27]. The data resolution is limited to 8 bits, which provides 255 levels per pixel. Most of the experiments are conducted at a distance of two metres as is the cameras minimum operating distance.   The Planck radiator's output energy level is adjustable by modifying the absolute temperature T, which is a part of description (2.6).
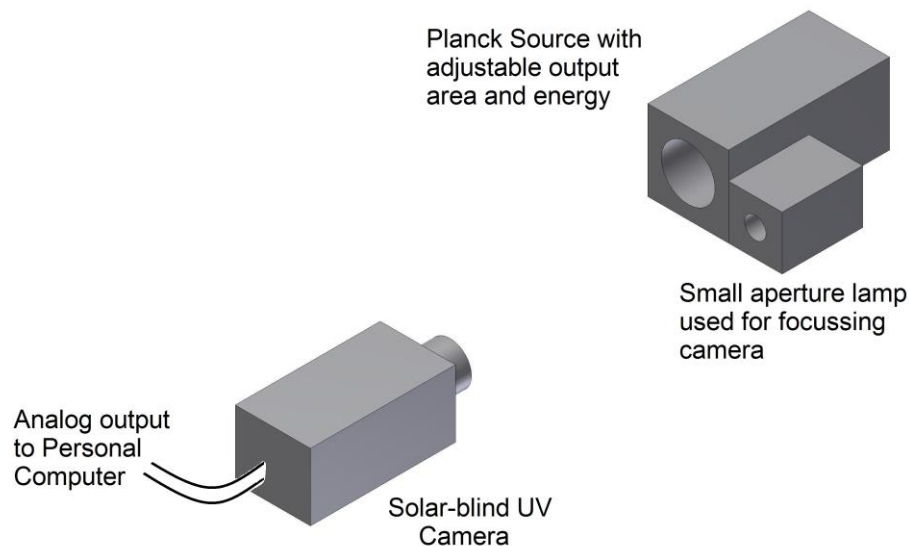
Figure 3.1. Camera and Planck Radiator test configuration.

3.5.2   Measurement output and processing

3.5.2.1   Introduction

According to image intensifier manufacturers, it is possible to use analog or event counts as noted earlier [35]. The analog method is part of the investigation presented here as the camera had some operational limitations with regard to counting. These limitations could only be overcome with direct access to the internal hardware, which wasn't possible. The advantage of the analog method is that it does not require sophisticated counting routines, with a cost in accuracy according to

detector manufacturers (section 2.5.2). Event counting was investigated but not all the experimental data are presented within this report, as the focus is here to determine the spectral response. Two hundred frames at a frame rate of 50 Hz was captured with a frame grabber and summed for each experiment to attain an un-calibrated measurement *X* as described by

$$X = \sum_{frame=0}^{200} \left[\sum_{i=0}^{Totalpixel} DL_i - background \right],$$ (3.3)

with

        DL_i the digital level of a pixel detecting a source,

        and

        background by inserting a lens cap in front of the camera lens.

The background in the previous relation is used to eliminate the noise floor ("background subtraction"). A lens cap is placed in front of the camera lens and 200 frames are captured giving rise to

$$Background = \left[\sum_{frame=0}^{200} \sum_{i=0}^{Totalpixel} DL_i \right] \div 200.$$ (3.4)

3.5.2.2 The need for statistical analysis

In addition to the noise (background) which represents the minimum detectable signal, the maximum detectable signal by a camera must also be taken into account. A single pixel that forms part of a CCD with thousands of pixels with a maximum value could imply that the measurement is saturated. One pixel with a maximum digital value could imply saturation, implying that a measurement is not usable. The saturation of an image, whether it be part of counting or an analogue method, can be detected with statistical methods such as histograms [27]. Experiments thus need to include analysis of the CCD images with histograms to ensure that the measurements do not saturate. It is suggested that each individual frame of the camera needs to be investigated with a histogram to determine if saturation occurs.

3.5.2.3 True radiometric measurement

To expand relations (3.3) and (3.4) to be actual true radiometric measurements of the UV optical flux with the units Watts or Joules per second (Appendix A.2 [18]), parameters such as distance, source area, atmospheric attenuation must be included (section 3.3). In addition to these parameters is the frame rate, which implies that the relation (3.3) should be

$$X_{\text{Value Per Second}} = \sum_{frame=0}^{\text{No of frames}} \left[\sum_{i=0}^{Totalpixel} DL_i - background \right] \div \text{FrameRate} , \tag{3.5}$$

which gives an analogue value per second. However, in this investigation relation (3.3) is used to explore the different factors (parameters) individually. This is to develop an understanding of the influence of each factor with an experiment, creating a model at a later stage, thus overcoming the operational limitations of the camera.

3.5.2.4 Graphical presentation of experimental processing

Figure 3.2 illustrates the processing of the experimental data of the solar-blind camera in graphical manner using relation (3.3). The two different options to process the data (event count and analogue) are illustrated as an example for a source observed at different distances.
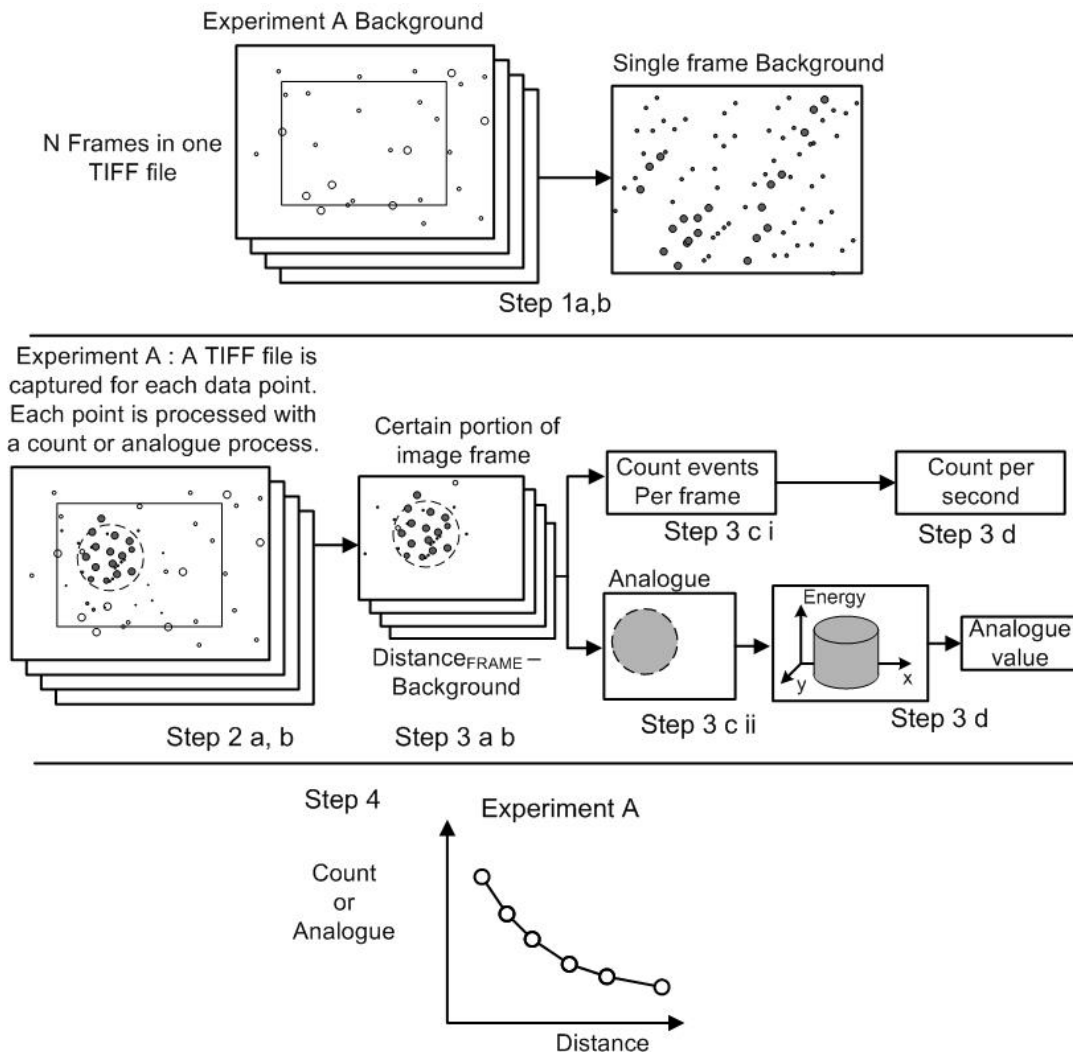
Figure 3.2. Overview of the processing of the experimental data.

Department of Electrical, Electronic and Computer Engineering   31
University of Pretoria

Each step in **Figure 3.2** is explained with a corresponding number as follows:

1. First background or blank images are captured to eliminate the noise floor:
   a. The camera parameters are set for a particular gain and operation (i.e. Attack and Decay value) that are required for the particular experiment.
   b. A lens cap is inserted in front of the camera's lens and a number of sequential images known as frames are captured and stored in a single TIFF file.

2. Actual experimental data are then captured as follows:
   a. The data for the particular experiment is captured by the camera in TIFF file format.
   b. Each change to the experimental setup (i.e. source size, output, distances and change in camera operating temperature) is captured in a specific TIFF file.

3. Processing of the images within a single TIFF file is subsequently done as follows:
   a. A particular predefined area on the image is specifically extracted from each TIFF frame for processing. The particular area for the particular camera investigated, is the portion of the image contained within a demarcated square of the images captured.
   b. The background image related to a particular camera setup as described in the previous step, is subtracted from each experimental TIFF individual frame.
   c. One of two methods can be used to process the particular frame (image):
      i. Event counting as one option.
      ii. Another option is to treat the image as an analogue picture.
   d. All the results (events or analogue method) from all the frames of a TIFF file are summed to obtain a count value or an image. The image displayed in the case of the analogue is cylindrical as a result of the circular reference source. The cylindrical image is dissected in some experiments to highlight and inspect certain aspects. All the pixel values in the analogue method are summed to obtain a value.

4. The result of the previous step of multiple TIFF files, which represent different changes (e.g. source energy captured at different distances with each distance in a single TIFF file) are combined into a single two dimensional graph, to present the results.

3.5.3   Confidence test: Analogue processing

The camera investigated with the experiments described in this study is regarded as not calibrated as the influence of the camera spectral function has not been included as part of calibration. An objective of the first experiment is to prove that the experimental results using relation (3.3) approximates the optical flux as defined by the term Irradiance. Relations (2.2) and (2.3) described

the Irradiance with a simplified model of a measurement (section 2.2.1). These relations highlight that the Irradiance upon the lens and measurement by the camera is directly proportional to the source area *Ao*. This implies that if the result of relation (3.3) is found to be directly proportional to a change of the source area, the relation can be used with confidence for experiments. Only the source area is changed, with other parameters and experimental setups such as the camera gain, source energy and distance between source and camera kept constant.

A Planck Source with an adjustable source area is used to perform this first experiment. The advantage of the Planck radiator source available for the experiment is such that it radiates within the solar-blind spectrum with an adjustable source area. **Figure 3.3** provides an estimated result of different source areas using (3.3) and the processing as described by **Figure 3.2**, assuming little distortion from the lens.
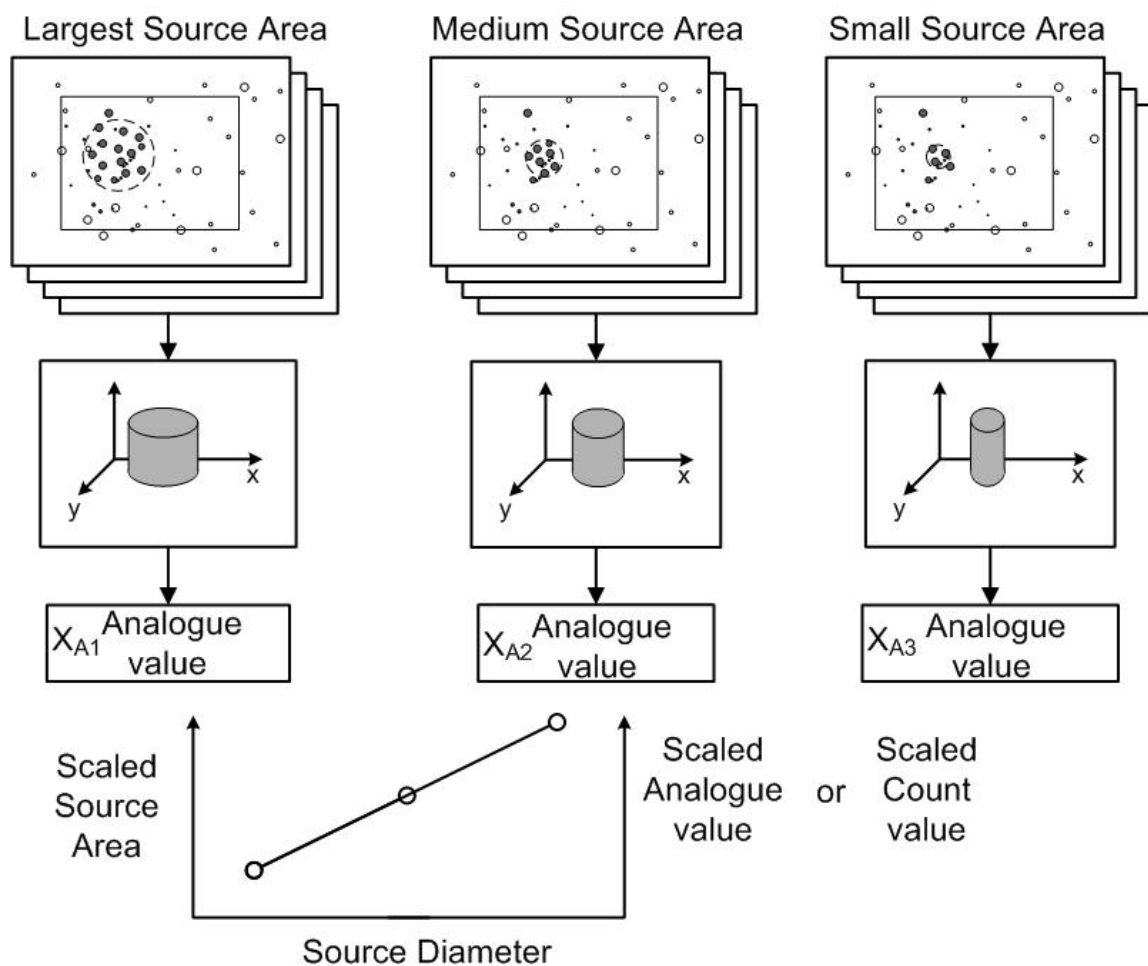
Figure 3.3. Estimated results of the source energy detected by changing the source area.

The results investigating the suitability of relation (3.3) for this investigation are described later in Chapter 4. All the following experiments described in this chapter are used to create a further

understanding of the camera operation using relation (3.3), verifying its specification and uncovering the unknown camera parameters. The aim is to progressively gain confidence with each experiment, with the objective of measuring the spectral response of the camera in the last experiment.

3.5.4 Dynamic Range

This experiment's objective is to determine the minimum and maximum energy measurable by the camera investigated, which is actually the dynamic range (DR) as discussed in section 2.4.7. **Figure 3.4** illustrates a conceptual drawing with the minimum and maximum values in the form of a transfer function of an infrared camera that the author encountered [48].
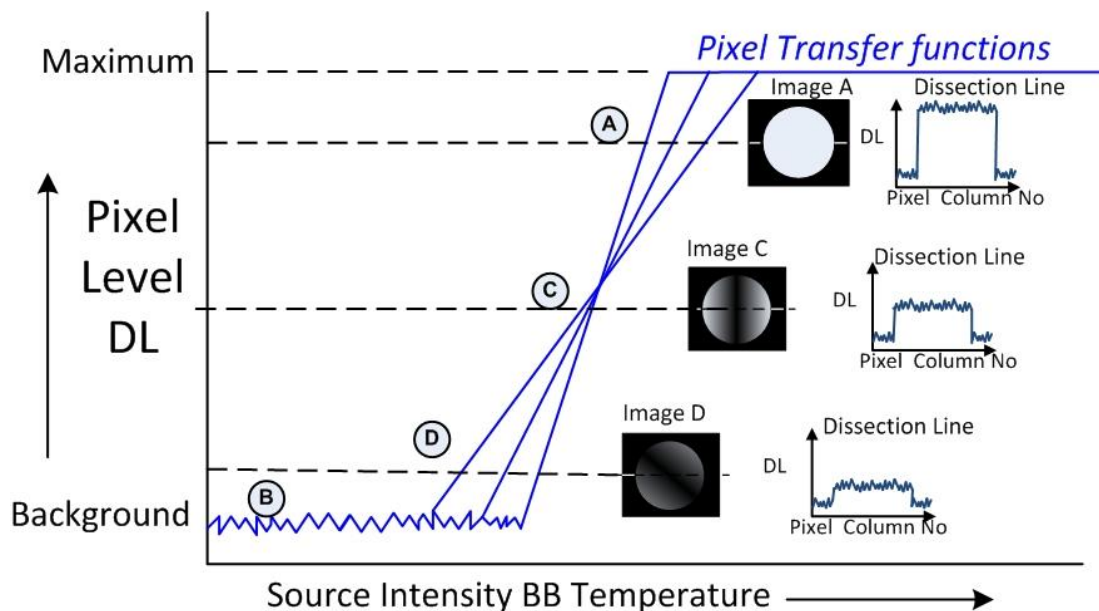
Figure 3.4. Typical transfer function from the author's experiences with infra-red cameras.

The figure shows the increasing value of three pixels and the total image, as a circular Planck source is observed by a camera. Also illustrated is a dissection line through the image, which increases as the source output energy is increased. The transfer function for the solar-blind UV camera should be similar to the photon count transfer functions of **Figure 2.11**, as discussed in section 2.5. The minimum level (as part of DR) that a camera can detect, can be obtained by measuring the camera output with a lens cap placed in front of the lens. The maximum measurable level of the solar-blind UV camera on the other hand is more challenging to obtain, as the source must have sufficient output energy in the case of solar-blind UV. Similar to other electronic equipment, the dynamic range of a camera is influenced by the selected gain of the camera itself [48]. This influence of gain on DR will be discussed later as part of the analysis of experiments. A

gain of approximately 60 to 70% was selected for most of experiments. This gain level is based on the experiments of Du Toit and the solar-blind camera manufacturer's experiences involving an electrical application [13, 14].

3.5.5   Gain

In addition to the dynamic range the gain of the particular solar-blind UV camera is also investigated. The output of the camera is recorded for different gain settings, observing a Planck source with a constant energy. The experimental result of the gain should approximate the typical relation of an ICCD's gain, as given by (2.16). Note: this is similar to an Electron Multiplying CCD (EMCCD) camera which also has an exponential gain relation [49].

3.5.6   Source area estimation

The intention of determining the lens map as mentioned in the previous section (3.5.8) is to use it to estimate the source area A_O. Source area in turn can be used to determine the source energy (L_λ the source radiance) from UV energy measurement relations (2.2) and (2.3). A Planck Source with a number of known source areas is used as part of this set of experiments, to determine if it is possible to perform source area estimations. The objectives of this experiment are as follows:

- To determine if the UV and visual channel of the camera source areas are similar in size. The particular type of camera used for electrical inspection has a visual and UV camera that share the same optical lens input from a beam splitter [2, 14]. The manufacturers of these solar-blind UV cameras, claim that the visual and the UV images are similar in size (Appendix A.4). The Planck radiator used for the experiment are detectable in the visible and UV wavelengths, which implies that the images of both should be the same.
- To determine if different sized source area targets are deducible from images captured at fixed known distance.
- To determine if the source area can be deduced for a known reference Planck source at different distances.

There are a number of simplified relations that can be used to investigate the source area estimation. The first relation provided here for estimating of the effective focal length f from a number of different sized targets at a known distance r, is

$$f = \left[\sum_{n=1}^{N} \sqrt{\frac{A_{in}}{A_{On}}} \, r^2 \right] \div N \tag{3.6}$$

where

f is the effective focal length [mm] of the camera,

N is the number of images (frame) sample,

r is the distance [m] between the reference source and the camera,

A_{in} is the image area [m^2] as seen by camera indicated here as a sample number n, and

A_{On} is the actual source (object) area [m^2] indicated here as a sample number n.

Another relation to use from classical thin lens theory for determining f of an image with the image diameter D_{IMAGE}, source diameter D_{SOURCE} and distance r, is

$$f_{eff\_XorY} = r / \left[1 + \left(D_{IMAGE} / D_{SOURCE} \right) \right] \tag{3.7}$$

3.5.7   Distance

Whereas the previous section's objective was only to uncover the relation between the source size and image size, this experiment's objective is to uncover the relation between the source's energy and its decay with distance. A Planck source is used as part of the experiment. The Planck source is not the ideal source for this experiment, as it is a wide band source. The reason for this is that each wavelength is attenuated differently within the earth's atmosphere. A narrowband - or electrical corona source of which the output energy is adjustable, is actually a better source to use.

Different Planck Source energies should result in attenuation that varies with distance. The results of the experiment should be clarified once the actual camera's spectral transfer function is known.

3.5.8   Lens transfer function

The objective of the lens experiments is to uncover the influence of the solar-blind camera's lens on UV energy measurements. According to the camera's specification the lens's Field-of-View (FOV) is $8.0°$ x $6.0°$, which is very narrow. This narrow FOV implies that there should be little distortion. A small target with a fixed energy is to be swept across the lens at a fixed distance, investigating the cos shaped relation (2.12) without the two axis camera table mount of **Figure 2.8**.

3.5.9   Individual count profile

Event profiling forms part of a solar-blind UV camera characterisation and calibration. Events similar to those depicted in **Figure 2.9** as produced by the solar-blind UV camera, are investigated with a Planck source with a large source area.

3.5.10 Spectral measurement and simulation

3.5.10.1 Spectral Measurement

The final set of experiments measure the spectral transfer function of the camera, using the procedure described in section 2.2.2. In section 2.2.2 is described how to use a wavelength adjustable source (monochromator) to uncover the spectral response of the solar-blind camera at different wavelengths. The solar-blind UV camera's output response (analogue or count value section 3.5.2) at each wavelength of a monochromator source, can be used to plot the camera's spectral response. **Figure 3.5** is a postulation of how the camera's spectral function can be obtained with the analogue processing technique described in section 3.5.2, which is similar to the count method of [6]. The source size is estimated to be similar for all the different source wavelengths, but with different heights, as postulated in the three dimensional plot at different wavelengths.
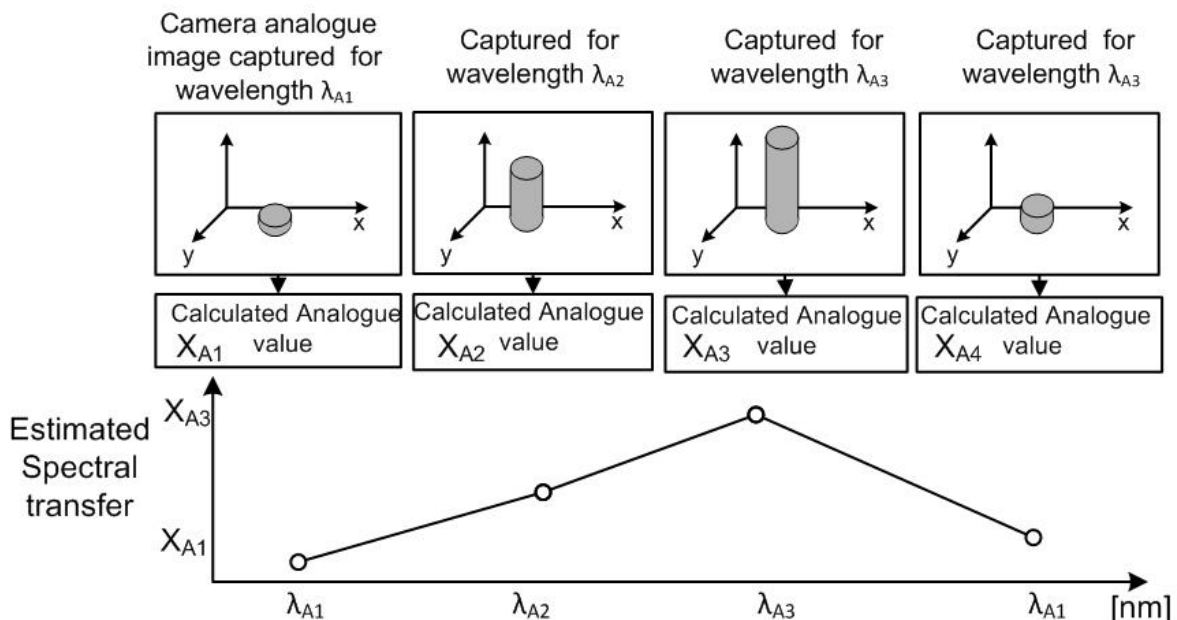
Figure 3.5. Expected spectral transfer function using the analogue function.

3.5.10.2 Incorporating the spectral transfer function into a model

Finally the spectral transfer function measured in this experiment is used in the simplified model of section 2.2.1. An objective of the simulation is to determine if the camera's spectral function influences the camera's output as postulated in **Figure 2.3**, implying that the spectral transfer function of the solar-blind UV camera is less than what Du Toit expected [14]. It is hypothesised that it could explain the difference between Du Toit's model and actual practical measurements. The next chapter (4) provides the experimental results.

CHAPTER 4   EXPERIMENTAL RESULTS

4.1   EXPERIMENTAL RESULTS

4.1.1   Actual equipment used for experiments

Figure 4.1 contains photographs of the Planck source and the actual solar-blind UV camera used in the experiments. The source has an adjustable wheel with holes that provide different source sizes for the camera to observe. The diameter of the source size provided with the wheel range from 22.2 mm to as little as 0.8 mm. The actual image of the source of **Figure 4.1** was created via the visual channel that form part of the camera tested. Solar-blind UV cameras for electrical inspection can produce UV and visual images simultaneously or individually, with the help of a beam splitter and electronic- plus software processing [2].
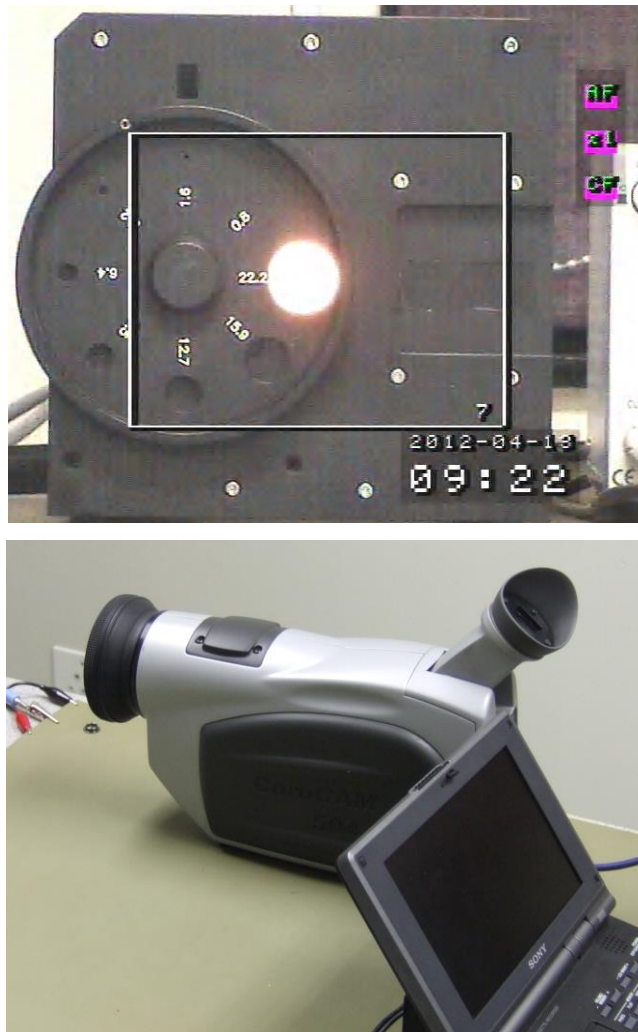
Figure 4.1. The Planck Source and the solar-blind UV camera used for experimentation.

4.1.2 Measurement output and processing

The left and right images in **Figure 4.2**, shows the typical events that occur in each frame of a TIFF file, captured from the output of the solar-blind UV camera investigated, for two different camera settings. The left hand picture in **Figure 4.2** shows the camera operating with a gain of 70%, with the attack (integration) and decay (subtraction or discharge) of 14% applied by the camera processing, whereas the right hand picture shows no attack and decay applied. A Planck source with a 1200 $^\circ$C absolute temperature (equation (2.5)) with a diameter of 22.2 mm, is observed at 2 metres. Only the area within the white triangle in the UV image is used to create an image with relation (3.3). The area within the white triangle of the UV channel, corresponds with the camera's visual channel shown earlier in **Figure 4.1**. The area demarcated with the white triangle is often referred to as the Area of Interest (AOI) by camera manufactures.

Figure 4.2. Single frame attack and decay on (left) and attack and decay off (right).

The images in **Figure 4.3** show that it is indeed possible to recreate the circular source image of the visual channel (wavelengths) of the camera in **Figure 4.1**, which is achieved by adding 200 frames of the UV channel using relation (3.3). The results are similar for both camera settings (attack plus decay on and off) as shown by the two images in **Figure 4.3**.

Figure 4.3. Summation of 200 frames with attack and decay on (left) and the summation of 200 frames with attack and decay off (right).

4.1.3   Confidence test: Analogue processing

The first test's objective is to provide confidence of the use of relation (3.3). The Planck source is placed at a distance of 2 metres from the solar-blind UV camera. Four different source targets are used to evaluate the use of the relation (3.3), using 200 frames and a background. **Figure 4.4** shows the results of relation (3.3) of the four different source targets within the AOI. The Matlab code that processes the TIFF files for each source size, is available in Appendix A.3.
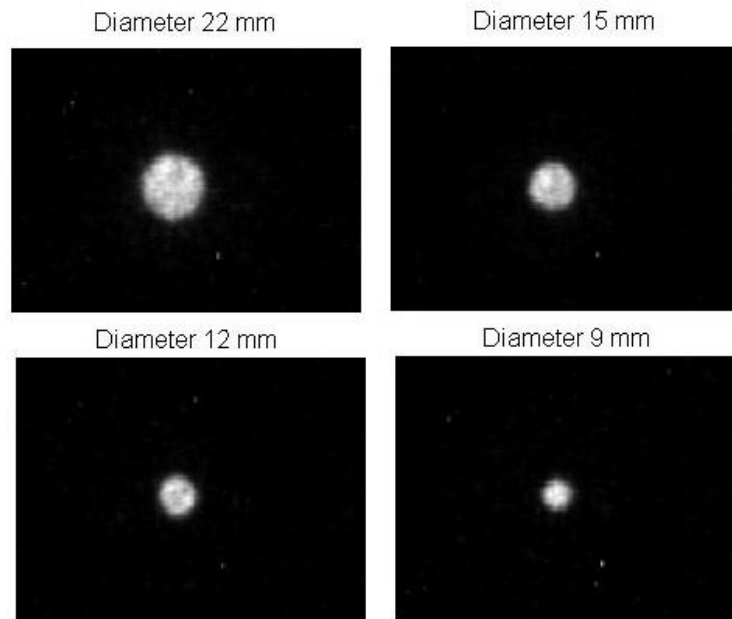
Figure 4.4. Different source sizes from 200 averaged frames for Planck source at 1200 °C.

It is possible to create a three dimensional image for each source area of **Figure 4.4**, as illustrated by the Matlab code of Appendix A.3 in **Figure 4.5**.
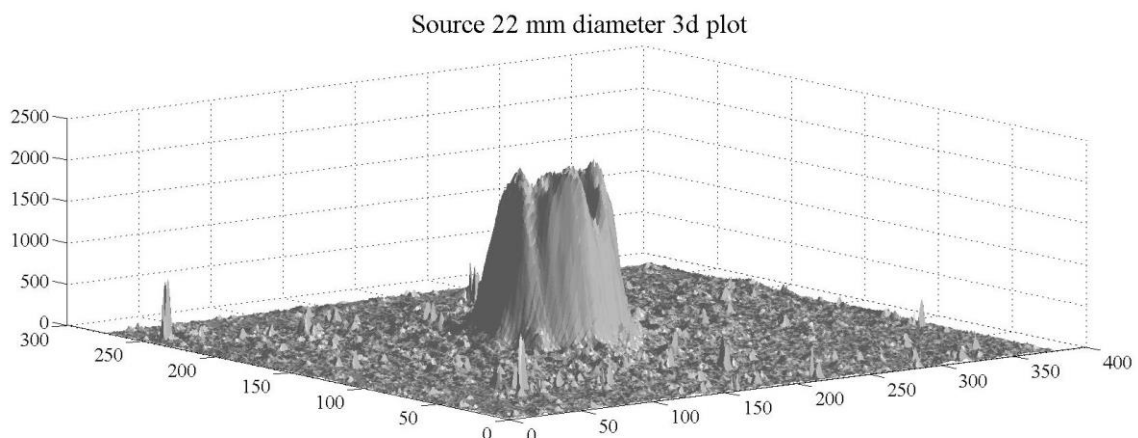
Figure 4.5. Three dimensional plot of the energy captured of a 22m source area from 200 frames and background subtracted.

The images as created in **Figure 4.4** are all summed individually, to provide a value for each source area and plotted and normalised to the maximum source area as shown in **Figure 4.6**. In addition to the summation of the image values in **Figure 4.6**, the different source areas of the experiment are normalised to the largest source area and also plotted in **Figure 4.6**.
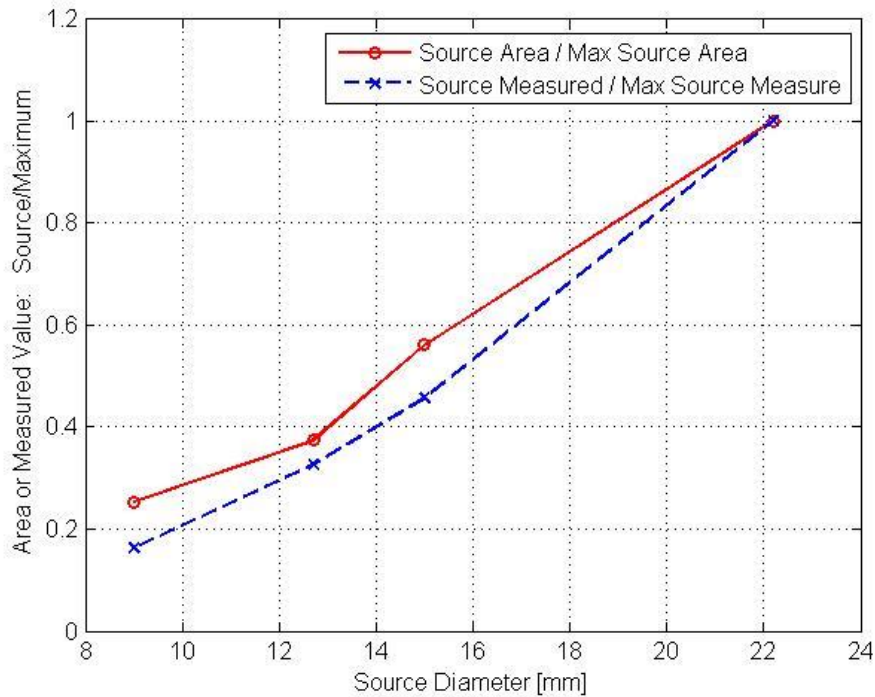
Figure 4.6. Analogue processing confidence test: Comparing source area and analogue measurement.

Figure 4.6 thus implies that there is a proportional relation between the source area and the actual value, using relation (3.3). The result of **Figure 4.6** corresponds with the postulated result of the experiment in **Figure 3.3**

4.1.3.1 Confidence test: Conclusion

The analogue processing technique can thus be used to explore the solar-blind camera experimentally, according to **Figure 4.6**.

4.1.4   Dynamic Range

4.1.4.1   Experimental Results

The objective of the dynamic range (DR) experiment was to determine the minimum and maximum values that a camera is able to detect (refer to section 2.4.7 and section 3.5.4 and **Figure 3.4**). The result of a 22.3 mm diameter Planck source as observed at a distance of 2 metres by the solar-blind UV camera, with a gain of 55%, using relation (3.3), is shown in **Figure 4.7**.
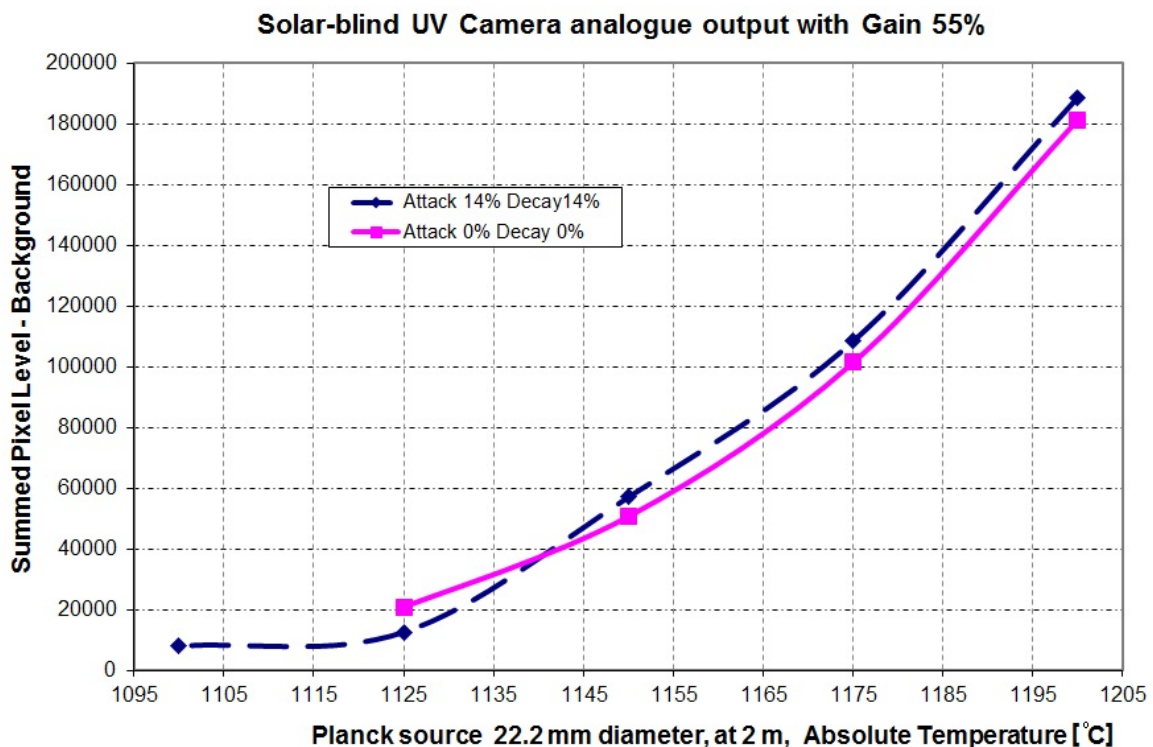
Figure 4.7. Dynamic range experiment: Observing a Planck source for different absolute temperatures with 55% camera gain.

Figure 4.7 implies that the attack and decay on or off results do not differ for the selected gain settings. The dynamic range for a gain of 55% is 3.3 dB.

This low DR corresponds with the notes of Joseph [40], which implies a low DR for image intensifiers. In addition to the 55% camera gain, the DR was also investigated for other camera gain settings, which seem to increase with a change in gain, as seen in **Figure 4.8**. This increase in dynamic range, with an increase in gain, does not correspond with experiences of the author related to infra-red cameras and electronic spectrum analysers [48, 51]. These other experiences implied that the dynamic range decreased as more gain was applied.
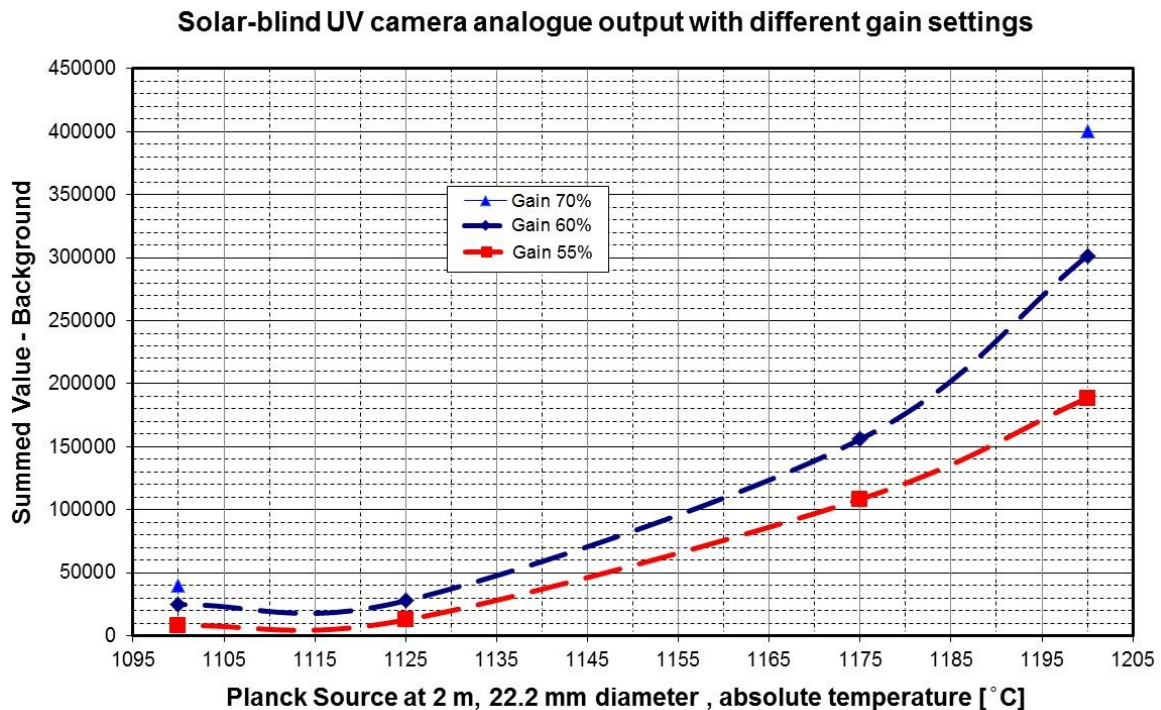
Figure 4.8. Dynamic range experiment: Observing a Planck source for different absolute temperatures, for different camera gains.

The data of **Figure 4.7** and **Figure 4.8** were subsequently also scrutinised with a statistical analysis to determine where saturation occurred. **Table 4.1** shows the results of the statistical analysis at 55% gain. The statistical analysis is influenced by the fact that the particular solar-blind UV camera performs a 'convolution' (exact processing unknown) to accentuate the events for visual imaging. This 'convolution' could have an influence on the statistical results, as argued in a discussion next.

Table 4.1. Statistical analysis of the 55%, Attack and decay on and off.

Plank temp Celsius	1100	1125	1150	1175	1200	1100	1125	1150	1175	1200
Attack	0	0	0	0	0	14%	14%	14%	14%	14%
Decay	0	0	0	0	0	14%	14%	14%	14%	14%
Frames saturation out 200	124	166	192	199	200	0	1	4	14	48
Bin 252	37	56	129	221	395	0	1	1	6	29
Bin 253	30	92	147	264	511	0	2	1	6	32
Bin 254	30	81	142	267	478	0	0	2	4	22
Bin 255	3057	5249	10143	19768	37878	0	5	17	51	230

When studying **Table 4.1** the question that arises here is why bin number 255 value is much larger than those of bin number 253. To understand the statistical results of **Table 4.1**, the individual

TIFF images were studied. **Figure 4.9** shows the worst case scenario of a three-dimensional image of one of the TIFF images for a camera gain of 70% and attack and decay set to 0%. The figure shows a single frame prior to the subtraction of the background frame, according to the procedure of section 3.5.2.4, as summarised in **Figure 3.2**. According to the camera's manufacturer notes and the operational manual, a convolution function (exact processing unknown) is applied to reduce noise [13-14]. According to experiences by the author, a convolution tends to accentuate (amplify) a signal with a very steep peak at the signal's centre. This accentuation results in a distortion of the original signal, implying an influence on the accuracy of the statistical and processed data.

Gain 70%: AOI 3D last Saturated image in TIFF stream, 1200 C Planck Source at 2 m
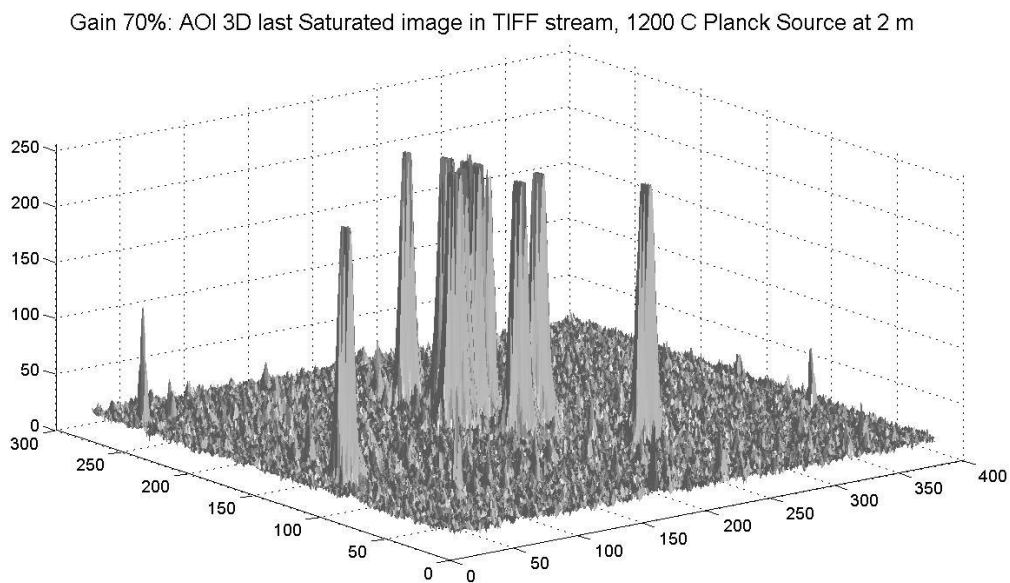
Figure 4.9. Dynamic range experiment: Gain of 70%, 3d image of saturated events.

4.1.4.2   Discussion and decision

It is uncertain at which gain the camera saturates, which could imply that the camera processing is wrong or the source is too weak. It can be concluded from the data presented in this experiment, that the unknown convolution processing should not be applied. However, the particular camera's convolution function is embedded in a variety of menus and hardware, which is difficult and time-consuming to deactivate. Lacking a software interface to deactivate the convolution function, it was decided to continue with rest of experiments with this function activated.

4.1.5   Gain

4.1.5.1   Results

This experiment investigated the camera's input versus output gain relation. The aim was to determine if the camera gain is similar or equal to equation (2.16). The Planck source was to an absolute operating temperature of 1200 °C, which ensures that solar-blind UV energy is detected. The source aperture was selected for the maximum 22,2 mm. The camera setting was 0% Attack and Decay. Two hundred frames were sampled at a number of camera gain setting using relation (3.3) and dissection lines on the resulting image. **Figure 4.10** shows the results for the experiment, which appears to be an exponential relation similar to equation (2.16). The exponential fitted relation on the data for the experiment yielded

$$\text{Value} = 3650.6 \, e^{0.0616 \times Gain} \, . \tag{4.1}$$
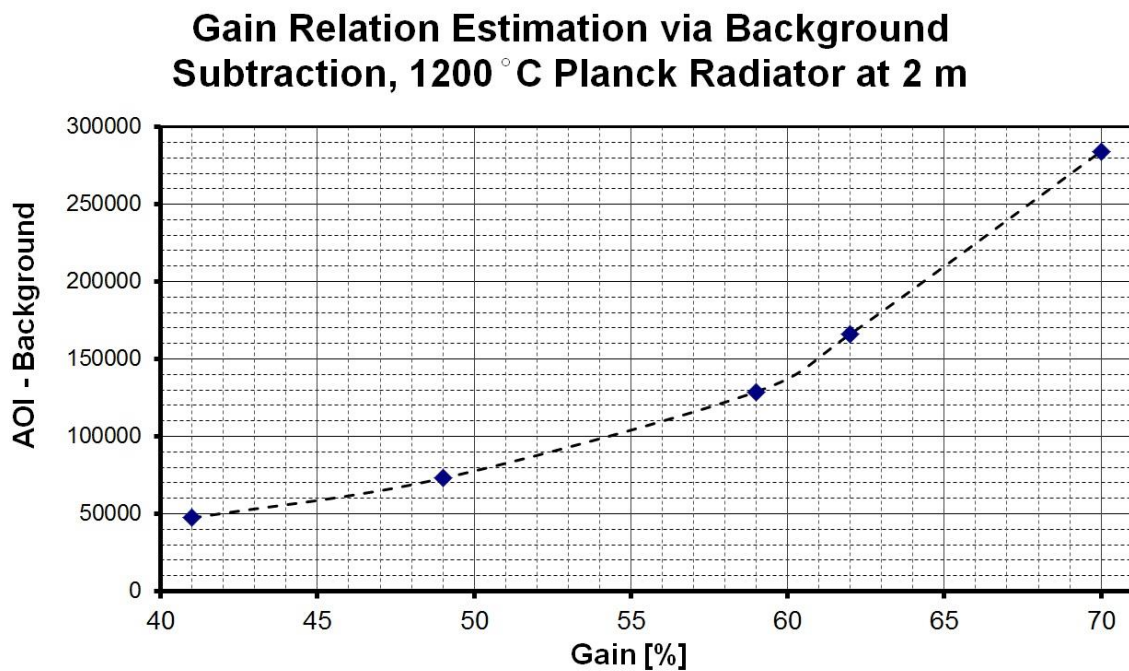
Figure 4.10. Gain experiment results: Investigating the effect of gain for a fixed distance and source.

4.1.5.2   Discussion

The result as fitted with relation (4.1) implies that the camera adhere to typical image intensifier's gain characteristics.

4.1.6   Distance

4.1.6.1   Results

Figure 4.11 illustrates the results for different Planck source temperatures and different distances between the source and the camera. The results highlight the different rates of attenuation, due to the differences in spectral content.
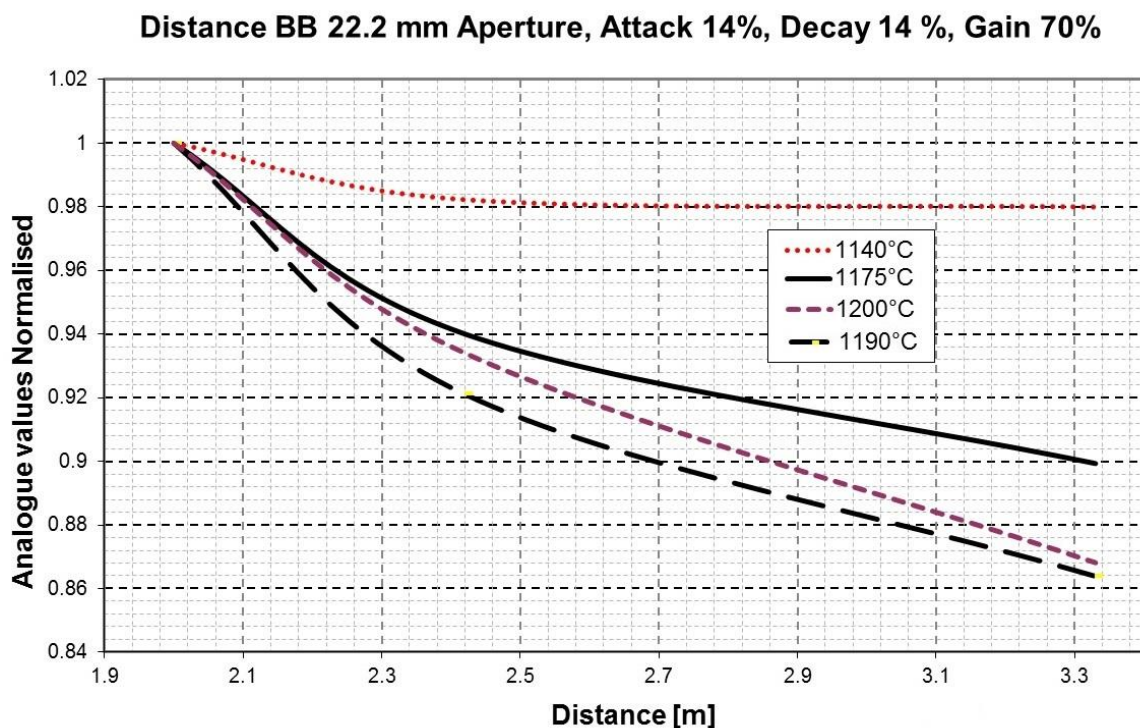
Figure 4.11. The effect of distance on camera measurements for different Planck source temperatures.

4.1.6.2   Discussion

The conclusion from the results is that the following aspects need to be considered to determine adherence of the results of **Figure 4.11** to a model:

- The source spectrum has an influence.
- The atmospheric attenuation at each wavelength needs to be considered.
- The Camera's spectral transfer function's influence on the measurements itself.

4.1.7   Source area estimation

4.1.7.1   Results of source area estimation at a fixed distance

The Planck radiator's different circular source areas as observed by the camera were investigated. The circular source areas observed had a cross diameter of 22.2, 15.9, 12.7 and 9.5 [mm]. Similar to other experiments the selected source's absolute temperature was 1200 °C. Using relation (3.3) 200 frames per source target diameter and averaging were used to create images similar to **Figure 4.4**. The gain of the IICCD was kept constant at 62% to avoid image saturation as encountered in section 4.1.5.1. The resulting images using relation (3.3) were measured with horizontal and vertical dissection lines. The aim was to determine if there is predictable relation between the source and camera image, which is known as the reduction factor M as part of (2.12) in thin lens models [27]. **Table 4.2** implies that there a predictable relation between the image- and the source area. Most of the source and related camera images produce a reduction factor (M) of 1.267×10^3 (refer also to sections 2.4.4.2 and 3.5.6). Note that the pixel dimensions used was assumed to be similar to the pixel dimensions presented by Du Toit [14], because this was the only information available from an earlier generation of the solar-blind camera used in this study.

Table 4.2. Target size estimation of a Planck Source of 1200 ℃ at a fixed distance with camera settings of gain of 62%, Attack 14% and Decay 14%.

BB Target Diameter [m]	Calculated Source Area [m²]	Relation to largest Source Area	Visual X Y Pixels		UV pixels Diameter X then Y	Pixel Dimension [m] [14]	Observed Image Area [m²]	Image Relation to largest Image Area	Reduction or M
22.2×10^{-3}	387.1×10^{-6}	100.00%	75	X	73	8.6×10^{-6}	319.215×10^{-9}	100.00%	1.213×10^3
			80	Y	78	8.3×10^{-6}			
12.7×10^{-3}	126.7×10^{-6}	32.73%	50	X	45	8.6×10^{-6}	123.616×10^{-9}	38.72%	1.025×10^3
			50	Y	49	8.3×10^{-6}			
9.5×10^{-3}	70.9×10^{-6}	18.31%		X	30	8.6×10^{-6}	55.501×10^{-9}	17.39%	1.277×10^3
				Y	33	8.3×10^{-6}			
15.9×10^{-3}	198.6×10^{-6}	51.30%		X	53	8.6×10^{-6}	157.477×10^{-9}	49.33%	1.261×10^3
				Y	53	8.3×10^{-6}			

4.1.7.2   Results of source area estimation at different distances with fixed source size

The effect of changing the distance between source and the camera was investigated, yielding the results as in **Table 4.3**. A Planck source aperture of 22.2 mm with an absolute temperature of 1200°C, was investigated at distances of 2, 2.37, 2.75, 3.66 and 4.21 metres. Using relation (3.3)

200 frames at each distance of the source target and averaging across all frames were used to create pictures similar to **Figure 4.4** to analyse. The dimensions of the averaged images in the X (horizontal) and Y directions (vertical) were measured with horizontal and vertical dissection lines. The objective was to determine if the reduction factor M changed with distance, thereby investigating if there was a correspondence with a calculated effective focal length. This effective focal length **Table 4.3** was determined by using equations (3.6) and (3.7)

Table 4.3. Target size estimation of a Planck Source of $1200\,\text{℃}$ at different distances with camera settings of gain of 62%, Attack 14% and Decay 14%.

BB Target Diameter [m]	Source Area [m^2]	Distance [m]		No Pixel $\times$ pixel size X or Y [14]	Calculated Focal length [m] X and Y	Image Area [m^2]	Reduction or M	Calculated effective focal length f [m] using area
22.2×10^{-3}	387.1×10^{-6}	2.00	X	$73\times8.6\times10^{-6}$	55.003×10^{-3}	319.215×10^{-9}	1.213×10^{3}	57.435×10^{-3}
			Y	$78\times8.3\times10^{-6}$	56.672×10^{-3}			
22.2×10^{-3}	387.1×10^{-6}	2.37	X	$61\times8.6\times10^{-6}$	54.712×10^{-3}	218.865×10^{-9}	1.769×10^{3}	56.356×10^{-3}
			Y	$64\times8.3\times10^{-6}$	55.384×10^{-3}			
22.2×10^{-3}	387.1×10^{-6}	2.75	X	$55\times8.6\times10^{-6}$	57.370×10^{-3}	169.587×10^{-9}	2.282×10^{3}	57.561×10^{-3}
			Y	$55\times8.3\times10^{-6}$	55.409×10^{-3}			
22.2×10^{-3}	387.1×10^{-6}	3.66	X	$41\times8.6\times10^{-6}$	57.222×10^{-3}	94.240×10^{-9}	4.107×10^{3}	57.108×10^{-3}
			Y	$41\times8.3\times10^{-6}$	55.256×10^{-3}			
22.2×10^{-3}	387.1×10^{-6}	4.21	X	$36\times8.6\times10^{-6}$	57.905×10^{-3}	70.638×10^{-9}	5.480×10^{3}	56.873×10^{-3}
			Y	$35\times8.3\times10^{-6}$	54.379×10^{-3}			
							f average	57.067×10^{-3}

4.1.7.3 Discussion

- The results imply on a macro-scale, that it is possible to determine the source size for the purposes of radiometric measurement, using image averaging. The source area, once known, can be used as part of the camera processing to determine actual source energy.

- The distance between the source and the camera must be known to perform the source area calculation.

- There is little change in the effective focal length when the distance changes.

4.1.8 Lens transfer function

4.1.8.1 Results

The lens map (distortion) was investigated for a Planck source placed 2 metres from the camera. The Planck source's aperture was set to a 9 mm diameter, with an absolute temperature of 1200 °C. Two hundred frames (images) were sampled at various locations on the camera's CCD by swilling the camera horizontally and vertically. The camera gain was set to 70% with Attack and Decay activated (14%), to attain an integrated value. **Figure 4.12** shows three of the locations on the image in the form of a composite image each using relation (3.3).
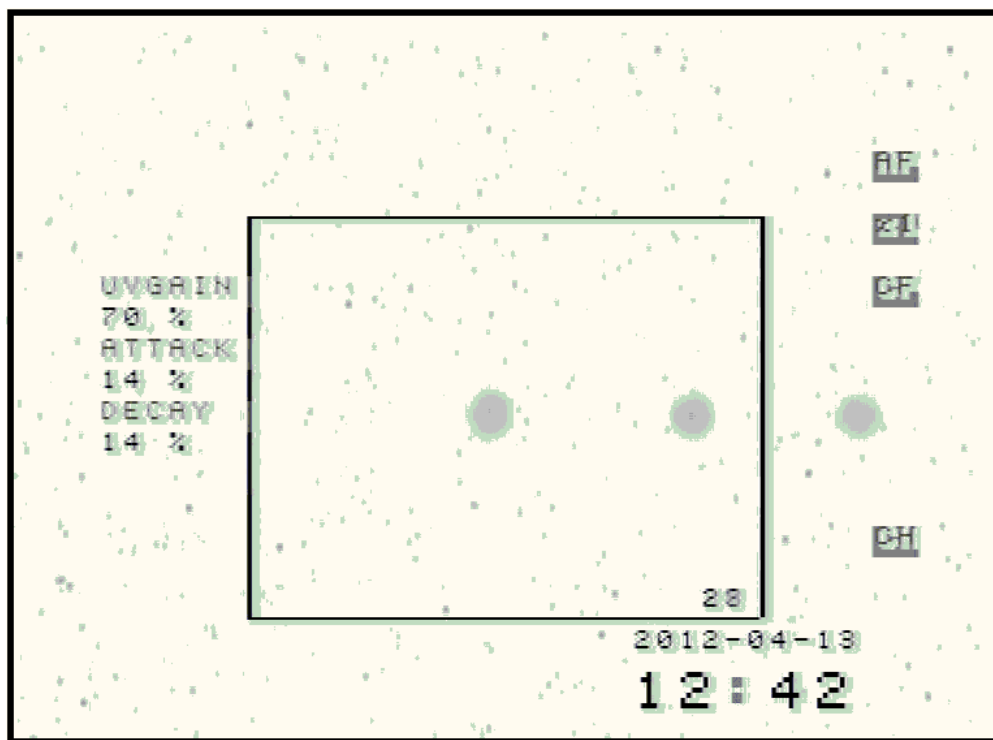
Figure 4.12. Composite image of three positions on the camera image plane which observed the same target. (Reverse contrast for the sake of clarity)

Figure 4.13 shows that there is a small deviation in amplitude and target size as a result of using (3.3). The results for each image imply a low image distortion for such a small FOV, especially in the Area of Interest (AOI) which is the white rectangle of **Figure 4.12**.

The distortion in the horisontal (X) and vertical (Y direction on the CCD seemed to be similar.

Image Distortion in x direction on CCD
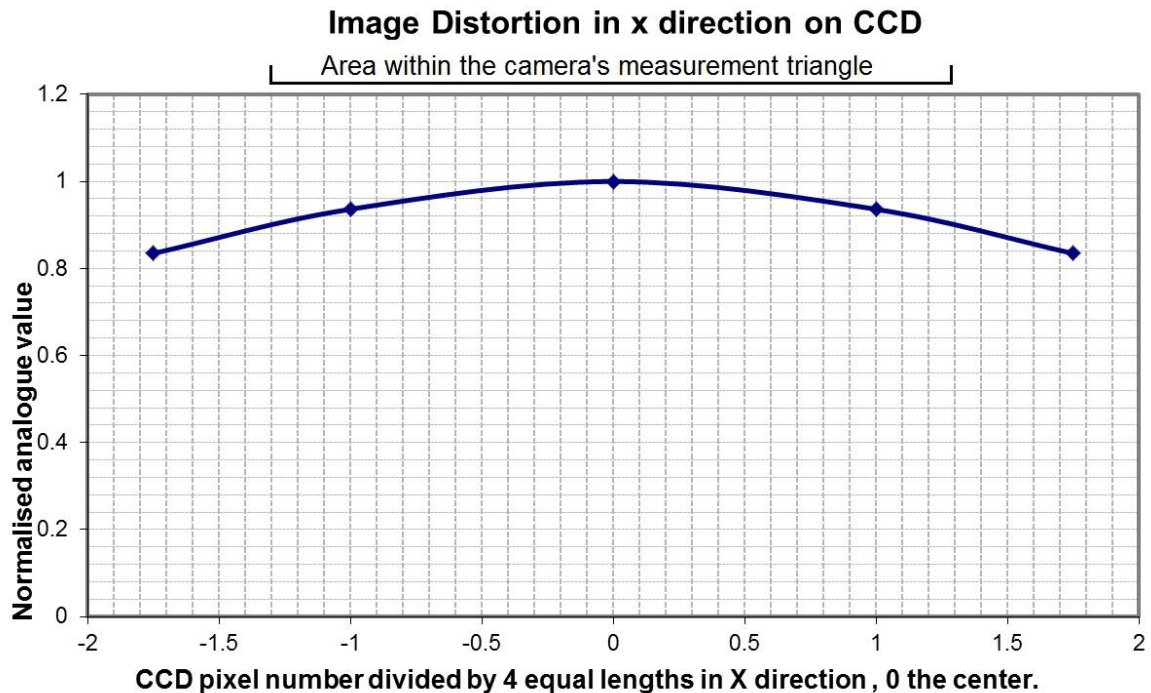
Figure 4.13. Normalised analogue value across an image for lens characterisation.

4.1.8.2   Discussion

Results appear to be more indicative, implying that an improved mechanical test configuration is required as suggested in **Figure 2.8**.

4.1.9   Individual count profile

Event pulses form and size of the solar-blind UV camera was investigated as described in section 2.5. Events were investigated for different camera settings (i.e. gain and integration on/off). The software package Image Pro-Plus 7 and Matlab were used to analise the data captured. Attack and decay on (14%) and off (both 0%) delivered similar results. Non-integrating mode (attack 0% and decay 0%) events saturated at smaller IICCD gain level in comparison with integrating mode activated. The default gain of the particular solar-blind UV camera at 70 % was found to be unsuitable for event counting, as the events were saturated. The saturation observed was similar to dynamic range measurements of section 4.1.5 as depicted in **Figure 4.9**. The ideal gain is in the order of 62% gain.   **Figure 4.14** shows an image of the typical events captured without any processing on the image. These images were investigated with horisontal - (**Figure 4.15**) and vertical dissection lines (**Figure 4.16**).
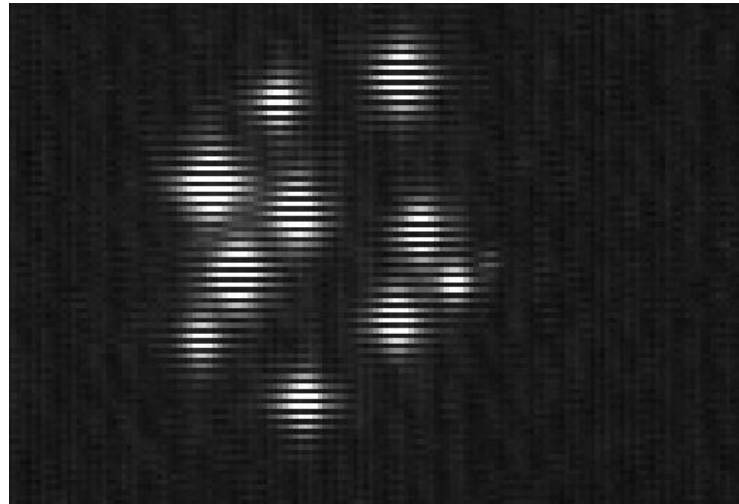
Figure 4.14. Typical events captured from the solar-blind UV camera evaluated.

Figure 4.15 shows one of the events dissected in the horizontal direction with a typical width of 15 pixels. **Figure 4.16** on the other hand shows the typical events dissected in the horizontal direction to be serrated (tooth-edged) as a result of the interlacing of two images [27] .
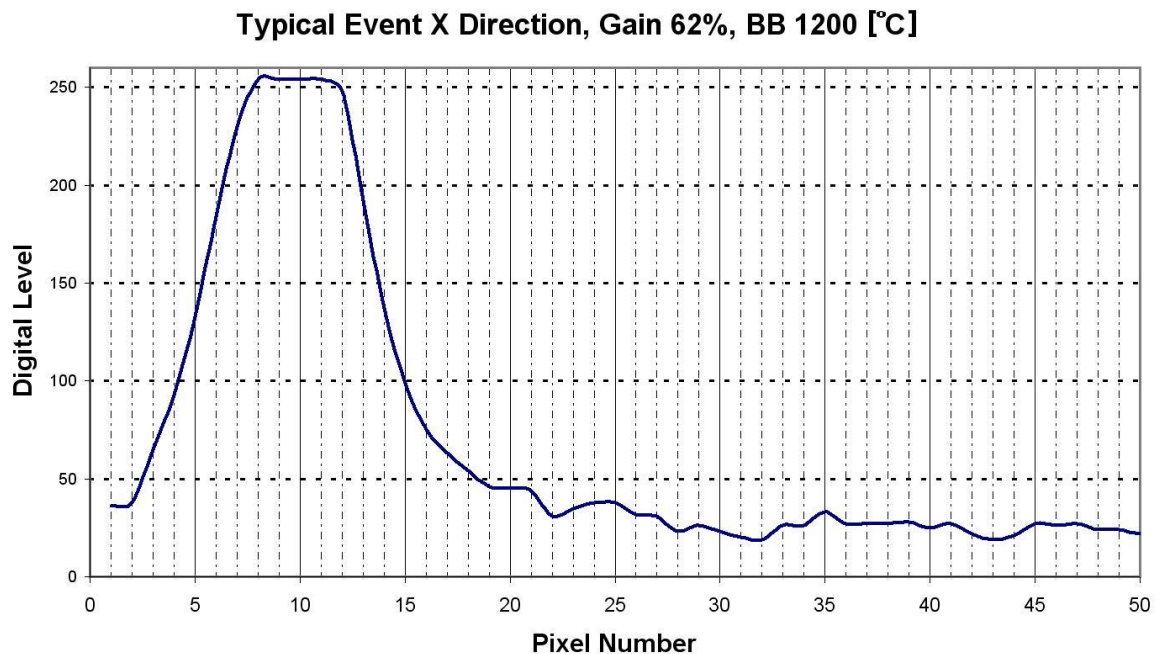
Figure 4.15. Dissection in the X direction of a typical event captured from the solar-blind UV camera evaluated.
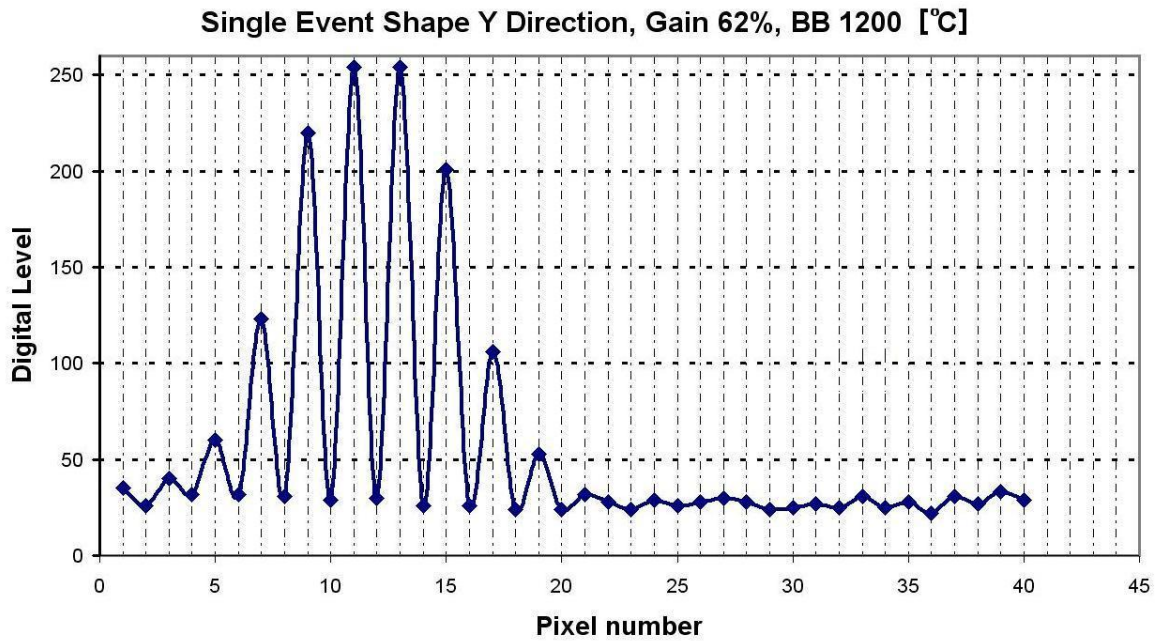
Figure 4.16. Dissection in the Y direction of a typical interlaced event captured from the solar-blind UV camera evaluated.

The shape and size of the events at different camera gains as collected are presented in **Table 4.4**. The predominant event size was 15 - by 19 pixels. Note that the first entry in the table (test no.16) didn't observe any source. The aim of this entry was to determine the thermionic emissions within the image intensifier.

Table 4.4. Event sizes collected at different camera gain levels.

Test No.	Gain [%]	FWHM X direction event width [pixels]	Other event X direction width [pixels]	FWHM Y direction event width [Pixels]	Other y direction events [pixels]	Saturated pulses ? Y/N	AOI averaged Sum	Max bin 254	Camera Count	Is a figure visible if average of 200 frames taken
16	62	15	✗	19	✗	Yes	1923010	30	32	No
10	41	10	9	15	10	No	1951382	3	69-80	Faint
7	49	15	10,9	15	12	Yes & No	1977048	25	99	yes
6	55	15	20,9	20	15	Yes & No	2017245	118	100	yes
3	59	15	10,9	15	9	Yes	2032913	155	73-100	yes
15	62	15	8	19	10	Yes	2070191	202	83	yes
2	70	15	12,5,9	25	20	Yes	2188156	445	81	yes

The results of test number 16 in **Table 4.4** imply that even with the lens cap on in the absence of a source, random events can still be observed. These events can be attributed to thermionic emission

from the image intensifier which approximated event sizes of 15 by 19 pixels. In addition to event profiling a statistical analysis was also performed as indicated with the Bin count in **Table 4.4**.

Figure 4.17 shows a dissection of two events that occur in close proximity of each other. This highlights that a camera process or mechanisms for the purposes of counting must be able to distinguish between one or more events.
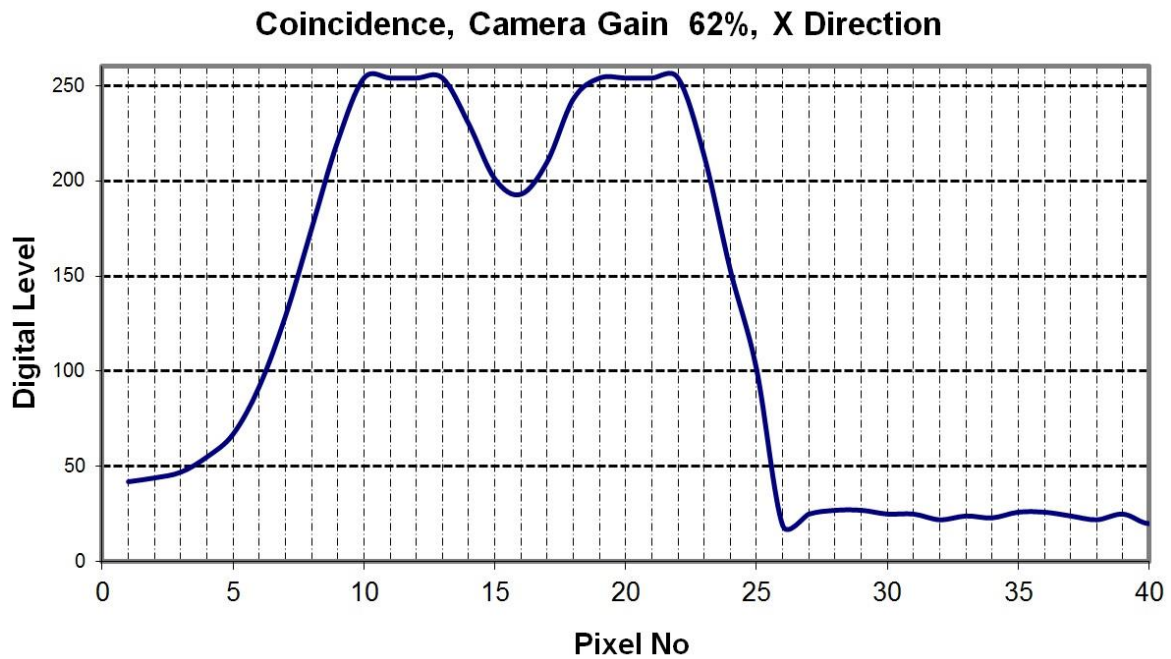
Figure 4.17. Dissection in the X direction of the typical coincidence of two events.

4.1.9.1   Discussion

It can be concluded that no convolution should be applied to the internal operation of the camera as it creates uncertainty with regards to saturation for the purposes of radiometric measurements.

Interlacing of the images create some uncertainty with regards to counting as the interlaced images are double the actual frame rate. A suggestion to overcome interlaced images is available from the author for those interested in photon counting.

Coincidence between events was observed.

4.1.10 Spectral measurement

4.1.10.1 Results

Armed with results of the previous experiments the spectral transfer function was measured as described in section 3.5.10. **Figure 4.18** shows the monochromator and its output via an optical fiber. This particular monochromator configuration is used to measure the wavelength response of single UV detectors [52]. The particular Chezy-Turner monochromator output power at each wavelength is non-linear as shown in **Figure 4.19**.
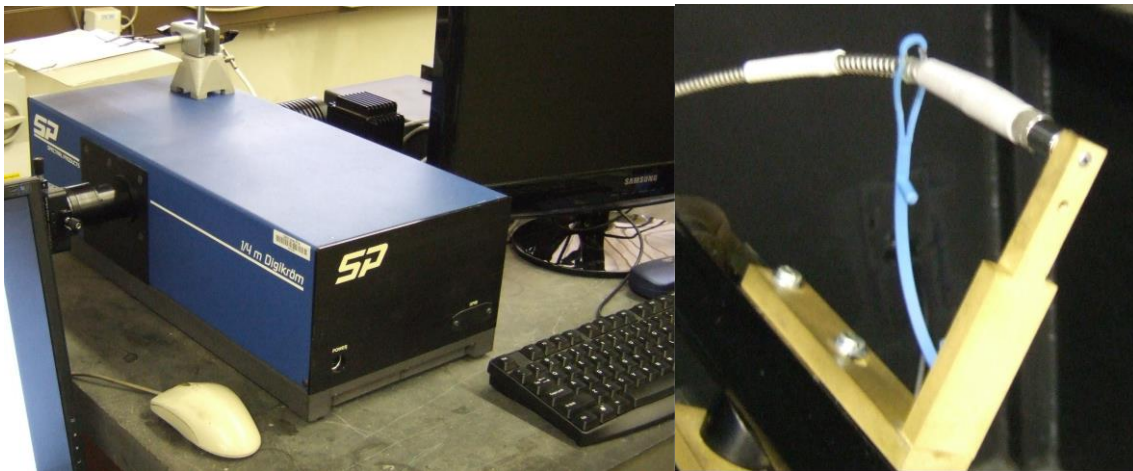
Figure 4.18. Chezy-Turner monochromator with fibre output.

Figure 4.19. Chezy-Turner monochromator wavelength response peak normalised.

Values of the graph in **Figure 4.19** were obtained from a reference detector that measured the actual optical power output at each wavelength of the monochromator as provided in Appendix A.6. The values of **Figure 4.19** were used to correct the results at each wavelength measured by the solar-blind UV camera. These correction values that were created from **Figure 4.19** for solar–blind UV wavelengths are available in a table in Appendix A.6.

The procedure to capture the analogue value at each wavelength as described in section 3.5.10 had to be slightly adapted. This was due to the discovery that the output power of monochromator within the solar-blind UV wavelengths was excessively more than the Planck Source used in the other experiments. The excessive power of the monochromator was concluded by the saturated events similar but even more saturated than those events studied in the dynamic range experiment of section 4.1.4 as shown in **Figure 4.9**. Energy detected by the camera was attenuated by lowering the solar-blind UV camera gain to 5% and increasing the distance to 3.84 metres between the monochromator and camera.

Figure 4.20 shows the solar-blind UV camera's spectral response which was obtained by multiplying analogue value at each wavelength obtained by relation (3.3) and (3.4) with the correction table in Appendix A.6. The half-power values approximate 248 nm 272 nm for a camera gain of 5%. The Matlab code to generate the spectral data is available in Appendix A.7.
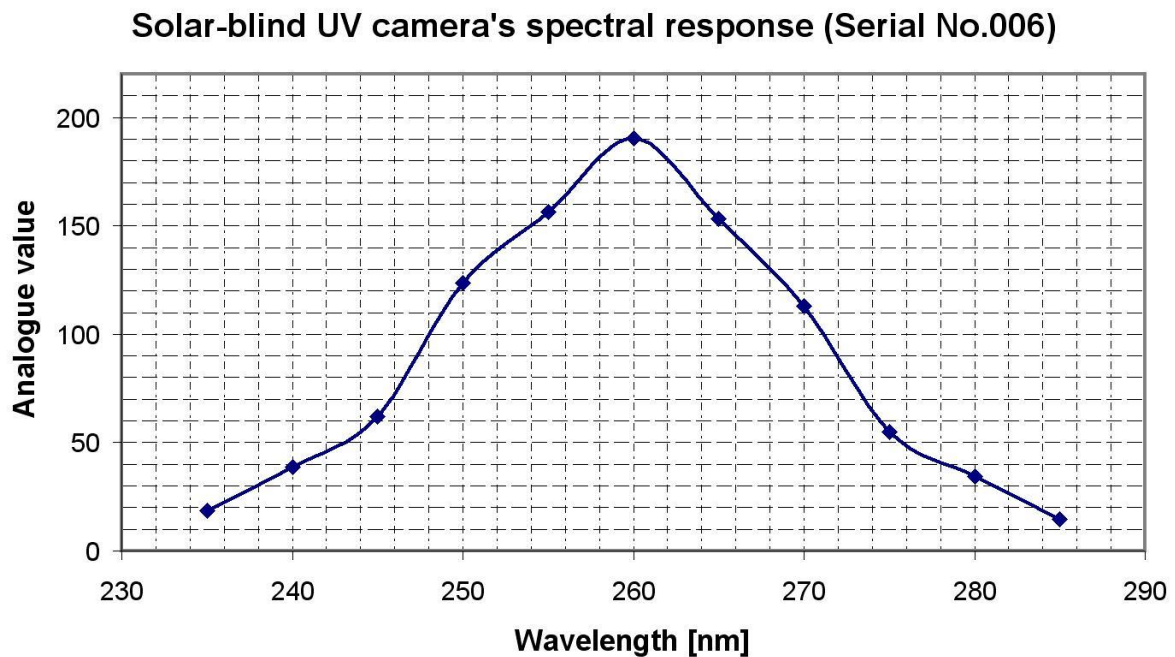
Figure 4.20. Solar-blind UV camera's spectral response.

4.1.10.2 Simulations using the spectral data

The hypothesis that the spectral transfer function of the camera has an influence on the actual measurement as stated in section 1.3 was investigated with the simplified model of section 2.2.1. **Figure 4.21** shows the camera's measured spectral function marked as *Corocam 504* as it was applied to the model of section 2.2.1. **Figure 4.21** also shows the earlier hypothesized camera spectral functions of **Figure 2.2** together with the measured spectral transfer function. Note that the actual throughput value of the actual measured spectral function is not shown by request of the manufacturer. The maximum throughput of the camera is shown for illustrative purposes to be approximately 10%, based on other similar solar-blind UV cameras which are 18% [54]. This is to compare an idealistic camera with a hypothesized actual camera which is known to measure only a very small portion of the source signal.
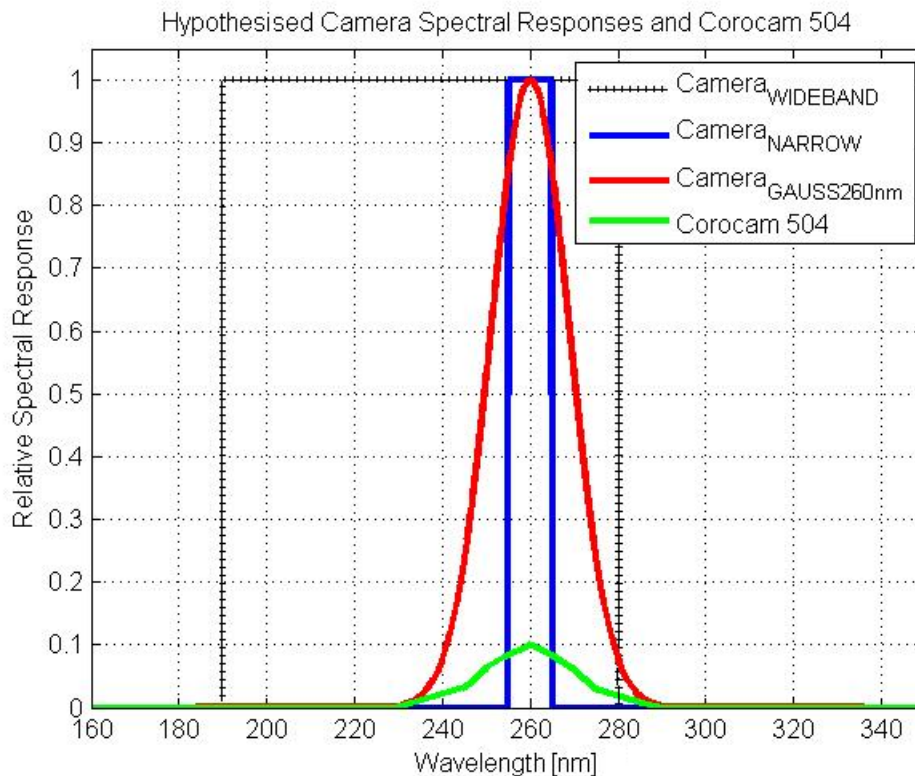
Figure 4.21. Solar-blind UV camera's spectral response in comparision with the model developed earlier in section 2.2.1.

The data of **Figure 4.21** was used in a Matlab model based on section 2.2.1 to determine the output response of the camera when it observes a Planck source. **Figure 4.22** shows the results of this model which code is listed in Appendix A.7. The figure highlights that the energy detected by the solar-blind UV camera is less than expected.
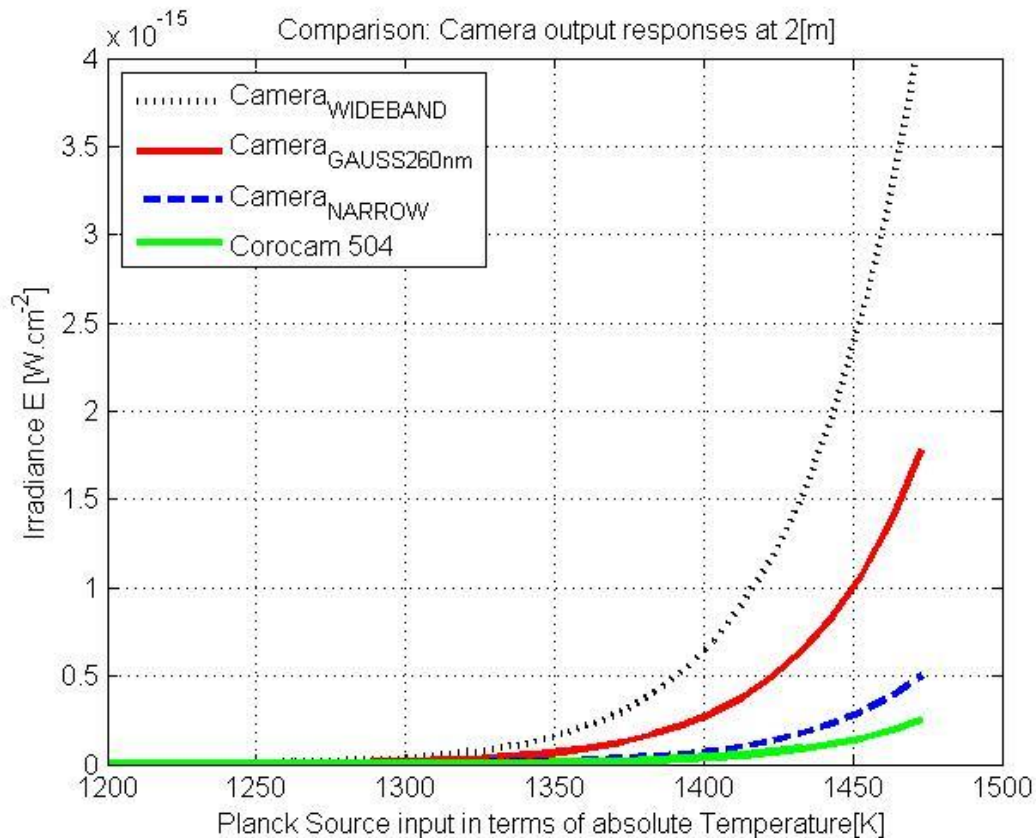
Figure 4.22. Solar-blind UV camera's output response used together with the camera

models in section 2.2.1.

4.1.10.3 Discussion

All the experiments such as the event analysis, dynamic range, distance and lens transfer function provided additional information that was used to create and improve the spectral transfer function. Each of these factors had a different contribution to a measurement that needs to be considered when constructing a model of the solar-blind camera.

The measured camera's spectral transfer function agrees with the initial hypothesis as simulated with a hypothesised model. The measured spectral transfer function's peak response was however less than the expected Gauss spectral function of the hypothesised model section 2.2.1.

4.2   CHAPTER CONCLUSSION

The next chapter provides a short discussion of the experimental results, followed by conclusions and recommendations in the final chapter.

CHAPTER 5   DISCUSSION OF RESULTS

5.1   INTRODUCTION

This chapter provides a discussion and observations of the experimental results of Chapter 4.

5.2   CONFIDENCE TEST: ANALOGUE PROCESSING

The results of **Figure 4.6** imply that the analogue processing technique, using relation (3.3), can be used to perform relative radiometric measurements. However, the additional convolution and other unknown processing by the solar-blind UV camera as implemented by the camera manufacturer, create uncertainties with regards to the saturation of the source signal (Dynamic Range section 4.1.4.2 as part of on 4.1.4). Fortunately, experiments such as the source area estimation confirm that relation (3.3) can be used with confidence to extract the source size. Furthermore, the lack of accuracy of the confidence test's results can be attributed to the limited 8 bit (256 levels) resolution of the sampling video card.

5.3   DYNAMIC RANGE

As noted earlier the statistical data as presented in **Table 4.1** and the discussion in Section 4.1.4.2, implies that some uncertainties arise where the saturation point occurs due to the camera manufacturer's convolution process. It is remarked that a different source, with different spectral content could have had a different result. Furthermore, it can be concluded that the results of **Figure 4.7** and **Figure 4.8**, must also be processed in such a manner that the saturation is incorporated as part of the graphs, as shown conceptually in **Figure 5.1**, using the statistics.
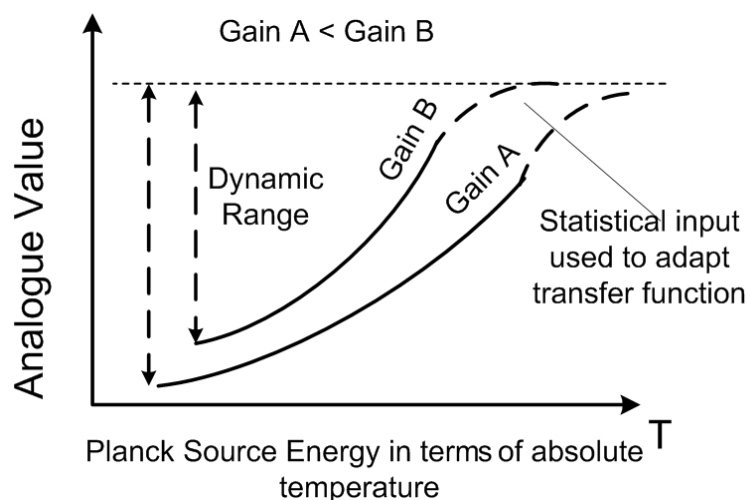
Figure 5.1. Conceptual adaptation of the dynamic range of **Figure 4.7**.

To provide an additional perspective on the DR, **Figure 5.2** illustrates the effect of gain on dynamic range, from experiences by the author with the design of spectrum analysers and infrared cameras [48, 51]. The figure highlights that as the gain is increased, the dynamic range measured decreases ("measurable input range"). Fortunately, the resolution increases with an increase in gain, as indicated on the output axis of the figure. Furthermore, the noise level (not indicated) which is located around V_{MIN} in the figure, increases as the gain increases. This implies that the output noise increases with gain, as illustrated around $V_{OUTMINB}$ and $V_{OUTMINC}$.
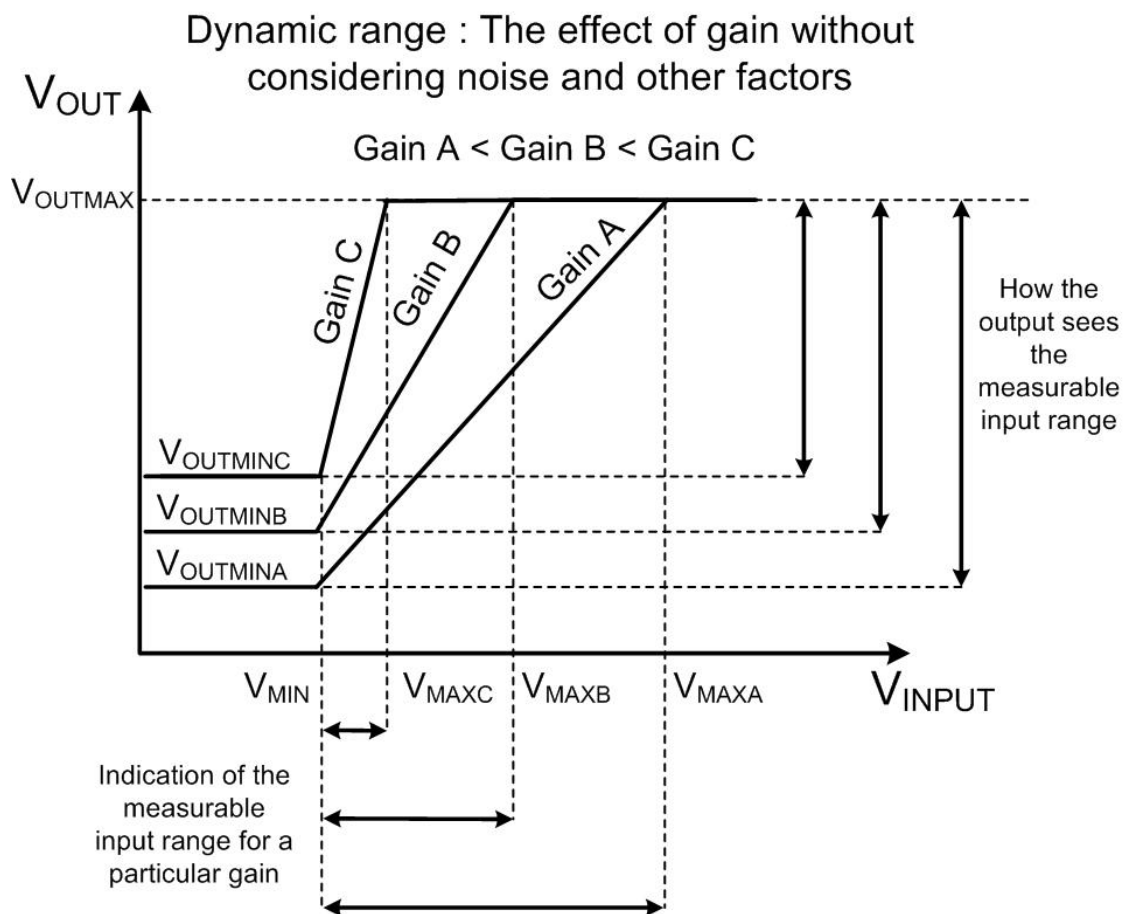
Figure 5.2. The effect of gain on the dynamic range, without considering noise.

5.4   GAIN

The resulting gain relation (4.1) magnitude corresponds with other ICCD experiments by Wiza [55], as well as the gain of 2 million of another similar solar-blind UV camera [54]. Similar to the DR experiment's discussion (section 5.3), the question arises what the result would have been on the resulting gain equation, if a narrow band source was used. A different wide band source with

another spectral content thus would have produced different results. **Table 5.1** created from the 30% to 70% experimental results, provides some insight into the gain relation, but with the cautionary note that other factors, such as the source bandwidth have an influence. The ICCD used has a gain of approximately 2 million, which is similar to other solar-blind UV cameras [13, 14, 54]. Some uncertainty is created by the wideband source's influence. The gain for the camera in reality should be less, as a result of extreme losses of the solar-blind filter and the low Quantum Efficiency (OE) of the image intensifier [4, 35]. Furthermore, the difference between the 5% camera gain used for the monochromator source and 60% to 70% camera gain used for the Planck source provides some indication of differences in output power of the two sources.

Table 5.1. Effective Gain from experimental relation.

Gain setting	Gain factor found by experimentation	Ratio to 5%
5	4967.4	1.00
10	6759.1	1.36
15	9197.1	1.85
20	12514.5	2.52
25	17028.6	3.43
30	23170.8	4.66
35	31528.5	6.35
40	42900.8	8.64
45	58375.2	11.75
50	79431.2	15.99
55	108082.1	21.76
60	147067.5	29.61
65	200114.9	40.29
70	272296.5	54.82
75	370514.1	74.59
80	504158.9	101.49
85	686009.5	138.10
90	933453.9	187.92
95	1270151.6	255.70
100	1728296.5	347.93

5.5   EFFECT OF DISTANCE

Figure 4.11 illustrates that different Planck sources' energy values have different effects on the attenuation of the energy observed by the camera with distance. However, the particular camera is used to observe electrical corona that has a spectral energy distribution [2] which is totally different from a Planck Source. In view of these facts and the results, it was consequently decided to provide

a recommendation for the adaptation of the particular experiment, as part of the calibration procedure in Chapter 6.

5.6   SOURCE AREA ESTIMATION

The set of experiments as noted in **Table 4.2**, confirms that the particular camera's images are smaller than the source (area) as expected. Furthermore, similar to other cameras the size of the image area also changes if the distance between camera and source is increased, as observed in **Table 4.3**. It can thus be concluded from these tables, that it is indeed possible to determine the actual source size, if the distance between the source and the solar-blind UV camera is known.

This experiment thus seems to fulfil the objective to determine the source two-dimensional area (sections 3.3.3 and 3.5.6). The source area can thus be used to scale the flux level measured by the camera to determine the source energy.

5.7   LENS TRANSFER FUNCTION

The experiment highlighted that the lens within the designated AOI (white rectangle) shows little distortion with the particular source area used. A smaller source and a dedicated mechanical test assembly with event counting might have yielded different results, similar to the experiments of Bergamini *et al.* [6]. These experiments by Bergamini *et al.* [6] could detect the lens Point Spread Function (PSF) of another ICCD camera.

5.8   EVENTS PROFILE

The comments and observations with regards to the event profile are as follows:
- A suggestion is that no convolution be applied as part of the processing of the camera.
- It is not advisable to use attack and gain to perform the correct event counting, as the number of events captured doesn't correlate with the camera's own results.
- The interlaced video encumbers real event counting as implied by **Figure 4.16**.
- The event counts as produced by the camera output do not correlate with the video data captured with a frame grabber.

A solution around the interlacing could be to produce two new de-interlaced images from the interlaced picture, followed by an event counting. **Figure 5.3** shows the alternate result for **Figure 4.16** if an image is separated into two de-interlaced images.
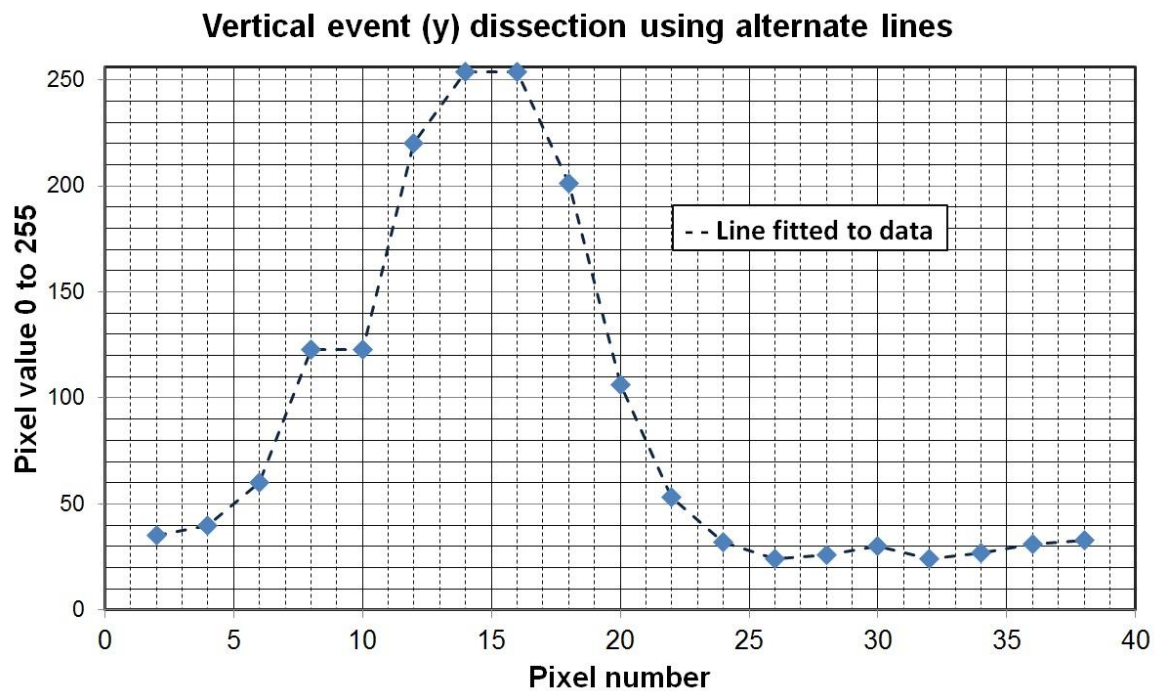
Figure 5.3. Using alternate image lines for interlaced images.

5.9   SPECTRAL TRANSFER FUNCTION

5.9.1   General remark on the experiment

The measurement of the spectral function attempted to ensure that the issues encountered by other experiments were not encountered. An example of an issue encountered by other experiments was the saturation of the camera images by the camera.

5.9.2   Comments on and additions to the results

The spectral measurement confirms the initial hypothesis that the spectral transfer function is a Gauss shape, as in the initial model of section 2.2.1. In addition, a simulation using the measured spectral data clarifies why there are differences between a mathematical model and actual measurements encountered by Du Toit [14].

Furthermore, there is one interesting observation made during the execution of the experiment itself. The solar-blind camera's gain observing the monochromator, is lower than the gain used for observing the Planck source. This implies that the monochromator has more energy at a single wavelength than a wideband Planck source. To prove the experimental observation, a simulation

was performed (Appendix A.8). The simulation *as a first order approximation considered no atmospheric attenuation.* In the simulation, the Planck source's energy that reaches the camera lens can be determined by

$$E_{\lambda PLANCKLENS} = L_{\lambda PLANCK}.\Omega_P.\cos\theta_{LENS} \tag{5.1}$$

where

$E_{\lambda PLANCKLENS}$ is spectral Irradiance that reaches the lens [W.cm^{-2}.nm^{-1}],

$L_{\lambda PLANCK}$ is the spectral radiance energy at the Planck source [W.sr^{-1}.cm^{-2}.nm^{-1}],

Ω_P is the projected solid angle as seen by the camera [sr] (where $\Omega_P = A_{PLANCK} \times r_P^{-2}$),

r_P is the distance in meter between the camera and the Planck source [m] ,

A_{PLANCK} is the Planck source area [m^2] ,

and

θ_{LENS} is the angle at which the lens lies relative to source, which is 0 in this case.

The energy of the monochromator in terms of spectral Irradiance (E_λ) as measured by a reference calibration detector as provided by Van Schalkwyk [52] (**Figure A.3**, Appendix A.6), can be described in the simulation by

$$E_{\lambda CALDET} = L_{\lambda MONO}.\Omega_{MONOCALDET}.\cos\theta_{CALDET} \tag{5.2}$$

where

$E_{\lambda CALDET}$ is spectral Irradiance that reaches the calibration detector [W.cm^{-2}.nm^{-1}],

$L_{\lambda MONO}$ is the spectral Radiance energy at the Monochromator source [W.sr^{-1}.cm^{-2}.nm^{-1}],

$\Omega_{MONOCALDET}$ is the solid angle that the detector sees[sr] ($\Omega_{MONOCALDET} = A_{MONO} \times r_{CALDET}^{-2}$),

r_{CALDET} is the distance between the Monochromator and the calibration detector[m] ,

A_{MONO} is the Monochrome (fibre) source area [m^2] ,

and

θ_{CALDET} is the angle at which the detector lies relative to the source is 0 in this case.

The energy of the monochromator in terms of the spectral Irradiance (E_λ) as measured by the solar-blind UV camera within the simulation is thus

$$E_{\lambda MONOCAM} = L_{\lambda MONO}.\Omega_{MONOCAM}.\cos\theta_{CAM} \tag{5.3}$$

where

$E_{\lambda MONOCAM}$ is the spectral Irradiance that reaches the camera [W.cm^{-2}.nm^{-1}],

$L_{\lambda MONO}$ is the spectral Radiance energy at the Monochromator source [W.sr^{-1}.cm^{-2}.nm^{-1}],

$\Omega_{MONOCAM}$ is the solid angle the camera sees[sr] ($\Omega_{MONOCAM} = A_{MONO} \times r_{MONOCAM}^{-2}$),

r_{CALDET} is the distance between the Monochromator and the camera[m] ,

A_{MONO} is the Monochrome (fibre) source area [m^2] ,

and

θ_{CAM} is the angle at which the camera lies relative to to source is 0 in this case.

Within the relations (5.2) and (5.3), the spectral Radiance ($L_{\lambda MONO}$) of the monochromator is the same, which imply that the two relations can be used to obtain the spectral Irradiance of the monochromator that reaches the solar-blind camera's lens at each wavelength is

$$E_{\lambda MONOCAM} = E_{\lambda CALDET} \cdot [r_{CALDET} / r_{MONOCAM}]^2 . \qquad (5.4)$$

Figure 5.4 shows the results of the comparison of the 1200 ℃ Planck source (22.2 mm source diameter) and the monochromator energy. The simulation calculates the energy that arrives at the camera lens at a distance of 3.84 metres, using relation (5.1) for the Planck source, the data of **Figure A.3** and relation (5.4). The simulation is listed in Appendix A.8 with the numerical values available in **Table A.5**.
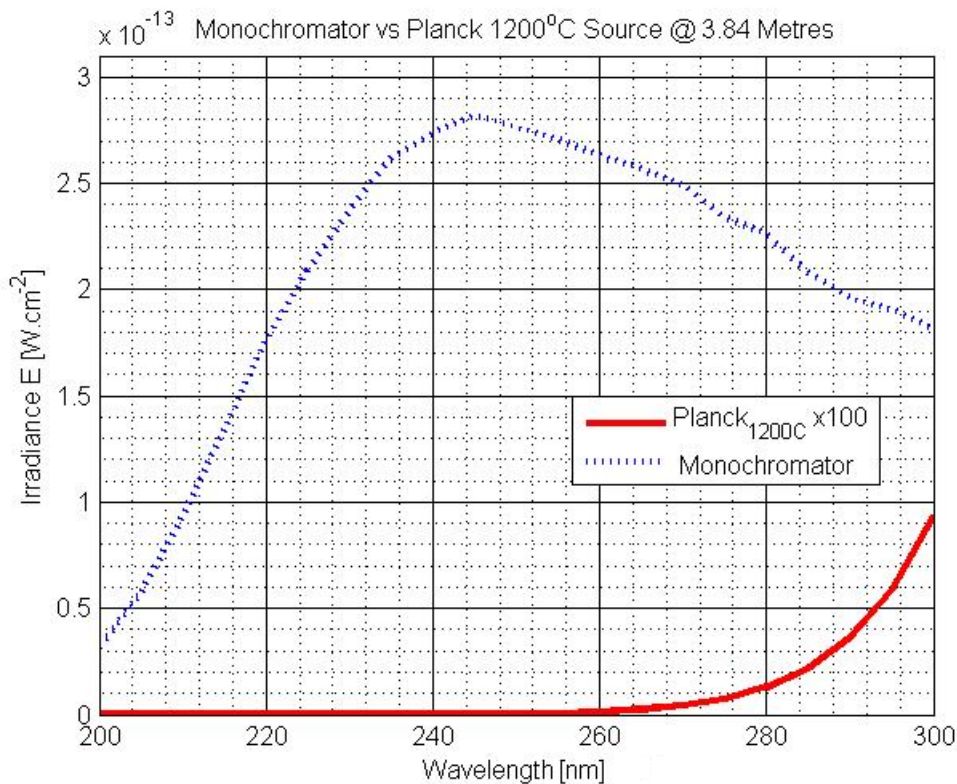
Figure 5.4. Comparison of the monochromator and the Planck source energy that arrives at the camera lens at a distance of 3.84 metres.

The simulation results as shown in **Figure 5.4**, shows that the monochromator energy arriving at the camera is more than the Planck source energy, which implies that the monochromator energy is

more than the Planck sources energy. There is an additional difference, the monochromator radiates narrow band energy as opposed to the Planck source that radiates over a wider band of wavelengths. This implies that the Planck source energy must be summed across wavelengths for a comparison with the monochromator's energy. In addition to the consideration of the source bandwidth, the energy from both sources must be weighted with the camera's spectral transfer function.

The simulation also compared the monochromator energy (Irradiance *E*) that arrives at the camera at 3.84 metres, with a 1200 ℃ Planck source at a distance of 2 m from the camera. The reason for this is to determine if the actual results correlate with the gain experiment results in **Table 5.1**. **Table 5.1** implies that the camera observing the monochromator at 3.84 metres with a gain of 5%, should have a ratio of 29 to 53 times less camera gain than the camera gain used for observing the Planck source at 2 metres.

The simulation resulted in a gain ratio of 21 between the monochromator and the 1200 ℃ Planck source. This is similar to the results of **Table 5.1**, but not identical to the expected value of 29 to 53 times the difference. The simulation thus implies that the gain of the camera observing the 1200 ℃ Planck source, should be 55%.

This 55% camera gain of the simulation instead of the 60 to 70% gain of the experiment can be attributed to the following:

- The solar-blind UV camera could indeed have been saturated for a gain of 60 to 70% in the experiment.
- The limited accuracy of the measurement of the camera's spectral transfer function.
- The particular camera's components were replaced as a part of maintenance after the Planck Source experiment, which was prior to the experiment with the monochromator. Thus the new components could have affected the differences in gain between the two experiments.

5.10 CHAPTER CONCLUSSION

Armed with the information in this and the previous chapters, the next chapter (6) provide conclusions, followed by the final Chapter 7 with recommendations arising from this investigation.

CHAPTER 6   CONCLUSIONS

6.1   INTRODUCTION

Conclusions for this particular investigation are derived from the goals and objective as stated in Chapter 1, as well as the experimental results from the other chapters.

6.2   CONCLUSIONS

6.2.1   Objective and questions

The objective of the study according to Chapter 1 section 1.2, was to improve the optical flux measurements performed by the particular solar-blind UV camera. A number of questions were used to expand and describe the objective in Chapter 1. Based on these questions as repeated below, conclusions from the study are provided next.

Why do results obtained from an earlier model and actual measurements differ?

- The spectral function has an influence, as determined by a simulation of the measured spectral transfer function in sections 4.1.10.2 and 5.9.2.
- Measurements of a source by the camera are saturated, with no internal camera mechanism (processing) to overcome this saturation as uncovered in section 4.1.4.
- The camera's convolution function was identified as a contributor to the saturation of the camera measurements (section 4.1.4).
- Other influences as identified in the earlier study of Du Toit [14] and other factors as stated in the investigation in section 3.3, also attributed to the differences between model and actual measurements.

How can a camera with limited measurement ability be characterized?

- A measurement methodology was developed based on the analogue method. This is one of the various methods with which the camera's data can be interpreted (section 3.5.2). The other method is counting, often referred to as "photon counting" (section 2.5).
- An experiment was developed and executed to provide confidence in the experimental results (sections 3.5.3 and 4.1.3).
- Furthermore, additional experiments were executed to uncover the camera operation.

What additional factors need to be considered in order to improve measurements?

- An automated gain control mechanism, the source area, the distance between the camera and the source, including the atmospheric attenuation are some of the factors identified.

6.2.2 Hypothesis and approach

A number of hypotheses were constructed to fulfil the main objective (section 1.3). The research results and the approach in accordance with these hypotheses, arrived at the following conclusions:

- It was confirmed that the solar-blind UV camera's spectral function influences its own measurements. This was achieved by experimentation and simplified simulations (sections 4.1.10.2 and 5.9.2.). It was determined that the transfer function approximates a Gaussian wide-band response within the solar-blind UV spectrum. In addition considerable amplification was required to detect solar-blind UV, which is highlighted by the experimental results and the analysis of the gain (sections 4.1.5.1 and section 5.4).

- It was confirmed through experimentation and the results of other research, that the particular camera does not consider the effect of distance on measurements. Consequently the camera needs to incorporate the effect of distance on its measurements in the future.

- It was confirmed that solar-blind UV is attenuated considerably (section 2.3.2). In addition, section 4.1.6 experimental results implied that the spectral distribution of a source also influences the attenuation of a radiometric measurement with distance. It can thus be stated that it is important that the camera knows what the source spectral distribution is. The reason is that different sources will have different atmospheric attenuation factors. **Figure 6.1** provides a conceptual illustration of the difference between a wideband Planck source, monochromatic and a natural source such as corona. A calibration solution is suggested in the next chapter [14, 18, 57].
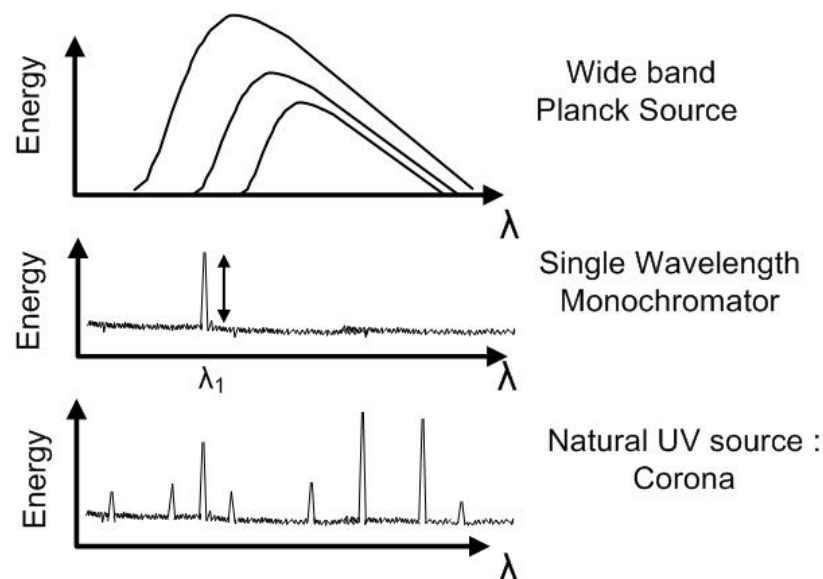
Figure 6.1. Conceptual comparison of monochromator -, Planck - and Corona spectrum.

- It can be concluded that the camera need some adaptation to its processing as summarised as follows:
    - Influence of distance must be incorporated in camera measurements.
    - Atmospheric attenuation should be included, as it has a considerable influence within the solar-blind UV spectrum, based on other similar camera experiments [24-26]. The value of γ approximates 0.9 to 1.1 according to **Table 2.1**.
    - Source area estimation must form part of the radiometric measurement process.
    - Saturation of images prior to processing must be avoided with the help of statistical analysis.
    - Interlacing of images must be accounted for in processing.
    - Camera software control must have additional commands to enable fast analysis of data and processing.
- The following can be concluded from a sample of research by others (**Table 2.2**), using solar-blind UV and related cameras for the purpose of electrical research:
    - Cameras are only used to observe the corona phenomena by some researchers.
    - Cameras are used by a certain group of researchers to determine the relation between corona emissions and electrical discharges. Unfortunately, the research objectives or roadmap for this group appears to be vague.
    - There are differences in the manner with which the different manufacturers calibrate and specify solar-blind UV cameras for corona detection [13].

6.2.3   Research Goals

It can be concluded that the research goals as stated in Chapter 1, were achieved. This is indicated as follows:

- It was possible to determine the spectral transfer function of the solar-blind UV camera.
- Additional factors that influence the measurements were identified, such as atmospheric attenuation, source area, distance and source spectrum.

6.2.4   Interrelated factors

It was concluded that all the different factors collected and identified are of course interrelated. All these factors thus need to be considered concurrently in any solution to improve the solar-blind UV camera's measurement. The next chapter thus provides recommendations to improve the camera's measurement of solar-blind UV phenomena.

CHAPTER 7   RECOMMENDATIONS

7.1   INTRODUCTION

Based on the results of this investigation and the conclusions, this chapter provides the following recommendations:

- That the measurement of the spectral transfer function of the solar-blind UV camera be adapted, with the consideration of factors identified.
- That an alternate calibration setup and procedure be used.
- That a proposed adaptation be implemented of the particular solar-blind UV camera's functional operation.
- That further research for the use of the solar-blind UV cameras for High Voltage Transmission lines focus on the actual practical measurement scenario encountered by maintenance personnel.

The objective of these recommendations is to provide ideas and stimulus for other further studies.

7.2   SOME ADDITIONS TO THE SPECTRAL MEASUREMENT PROCEDURE WITH CONSIDERATION OF IDENTIFIED INFLUENCES

7.2.1   Introduction

The relations used in Chapter 5 describe the energy that reaches the calibration detector and the solar-blind UV camera. The spectral transfer function is one of the factors that influence measurements by the camera of a source. All the factors identified in this study influence each other. This section shows how the measurement of spectral transfer function can be adapted to consider other factors that influence camera measurements. The particular reason is revealed later in this section.

7.2.2   Inclusion of atmospheric attenuation

The relations used in Chapter 5 with regard to the monochromator did not consider the atmospheric attenuation. This implies that relations (5.2) and (5.3) describing the energy that reaches the calibration detector and the camera lens from the monochromator, must include the atmospheric attenuation. Thus the relations (5.2) for E_λ at each wavelength upon the calibration (reference) detector considering the influence of atmospheric attenuation with (2.9) is

$$E_{\lambda-CALDET} = L_{MONO}.\Omega_{MONOCALDET}.e^{-\gamma r}.\cos\theta_{CALDET} \tag{7.1}$$

Similarly the energy in terms of spectral Irradiance (E_λ) at each wavelength arriving at the lens of the camera from the monochromator as described by (5.3) can be derived as

$$E_{\lambda-MONOCAM} = L_{MONO}.\Omega_{MONOCAM}.e^{-\gamma r}.\cos\theta_{CAM} \tag{7.2}$$

7.2.3   Considering the camera gain

In addition the spectral Irradiance (E_λ) arriving at the lens of the camera from the monochromator considering the camera gain G and an arbitrary offset w often encountered in electronics, which implies that (7.2) can be expanded to be

$$E_{\lambda-MONOCAM} = G\left[L_{\lambda MONO}.\Omega_{\lambda MONOCAM}.e^{-\gamma r}.\cos\theta_{CAM} + w\right] . \tag{7.3}$$

In the case of this particular solar-blind UV camera with an IICCD, the gain G can be described by an exponential function as described by (2.16) , as found experimentally by (4.1).

Note also that (4.1) was derived from a wideband source and not a narrowband monochromator source, which implies that the gain relation will be different as investigated in section 5.9.2.

7.2.4   Incorporation of other additional factors

There are of course more factors influencing the measurement that must be considered. These factors are not listed, as it could be part of further investigations. Examples of these factors are:

- The operation of camera components that fluctuate with temperature. An example of temperature variation is Electronic Background Interference (EBI) of the intensifier [35].
- Manufacturing tolerances that cause slight measurement variations. These include optical components and electronics. An example of this is the solar-blind filter of the camera which spectral transfer function can deviate due to variation in tolerances [4,13].

7.2.5   Proposed amendments to the measurement of the spectral transfer function

The procedure to measure the spectral transfer function as described in sections 2.2.2 and 3.5.10 whether analogue or using counting, can be slightly amended with the additional influences described by sections 7.2.2 and 7.2.3 as follows:

1. Measure the monochromator's spectral transfer function at a particular distance r_1 with the help of reference calibration detector.
2. Measure the monochromator's spectral transfer function at another distance r_2 with the help of reference calibration detector.
3. Use the results of step 1, 2 plus relations (7.1) and (2.10) to determine the atmospheric

attenuation γ (section 2.3.2) at each wavelength. Furthermore, the spectral Radiance L_λ at each wavelength of the monochromator can be determined by using γ.

4. Measure the camera's spectral response with the monochromator at each wavelength in analogue or count units for a particular camera gain setting, plus a selected distance.

5. Use relation (5.4) and results of the calibration detector (7.1) and camera (7.3) to determine the spectral response of the camera.

6. The resulting spectral response, atmospheric attenuation and spectral Radiance of the monochromator from the previous step should result in a camera spectral transfer function in terms of spectral Radiance (L_λ) or spectral Irradiance (E_λ).

7.2.6   Concluding remarks of the spectral transfer function additions

The following conclusions can be made from the recommended additions to the spectral transfer function's measurement:

- Relation (5.4) can be also used for the case where the relations for the calibration detector (7.1) and the camera (7.3) consider the inclusion of atmospheric attenuation. Furthermore, the gain of the camera at the time of measurement would also need to form part of (5.4).

- The inclusion of the atmospheric attenuation at each wavelength and the gain should provide a more accurate camera spectral transfer function.

Finally, it can be concluded that the monochromator can form part of the calibration of a solar-blind UV camera, with a number of additions as is recommended in the next section.

7.3   PROPOSED CALIBRATION SETUP

7.3.1   Proposed calibration setup

Figure 7.1 illustrates a proposed calibration optical bench for the solar-blind UV camera as part of the recommendations. The test setup is idealistic and for illustrative purposes, which implies that it can be adapted as required. The figure illustrates a reference camera and a camera to be calibrated. Both cameras are able to view through a beam splitter, a device which can adjust the path length and a set of filters and different calibration sources. Furthermore, the camera to be calibrated can also stare into an integrating sphere with a monochromatic (single wavelength) source. The source in this case is a monochromator, which feeds the sphere with a fibre optic connection. As part of the calibration the camera is placed on an X-Y table mount, which is somewhat specific for a narrow field of view (FOV) camera. The X-Y mount allows rapid mapping of the camera's optics, for the purpose of calibration. Not shown in the figure is a computer that controls the entire test assembly, which can be fully automated with electrical components (ex. motors).
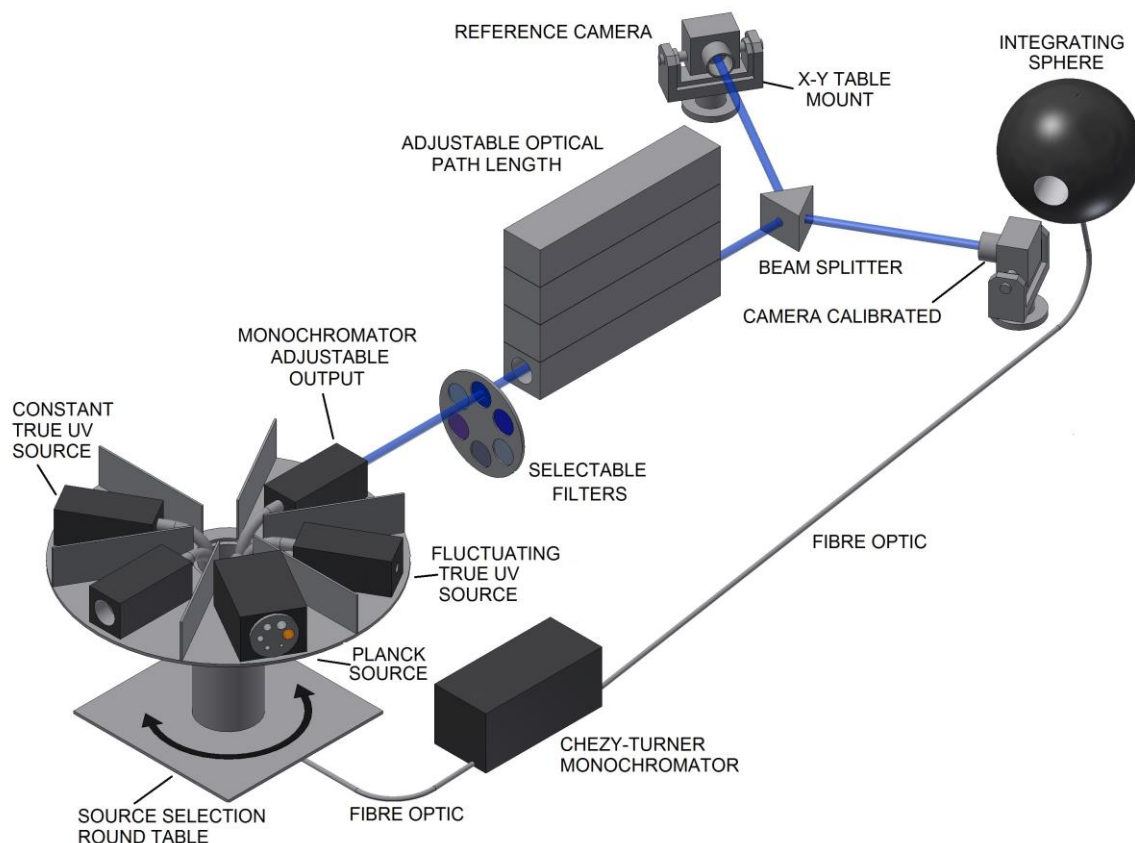
Figure 7.1. Proposed Calibration setup.

The sources and the other parts illustrated in **Figure 7.1**, each have a specific function explained in the following paragraphs. These components form part of the proposed calibration later.

7.3.2   Reference camera

The reference camera of **Figure 7.1** ensures that a calibrated camera measures the UV energy even if there are fluctuations (or changes) in the measurement environment, such as the atmospheric conditions (section 2.3.2 and 2.3.3). As a substitute for the reference camera, a reference calibration detector can be used, as discussed in section 7.2.5.

7.3.3   Integrating sphere

An integrating sphere with a lamp or led source is usually used to calibrate a solar-blind UV camera, with the objective of uncovering non-uniformity and set energy levels of a camera during calibration [53]. In contrast to these commonly used sources, this particular recommendation suggests that the source of the sphere be a monochromator. Such a monochromatic (single wavelength) source for the sphere ensures that the camera lens is radiated uniformly during the measurement of the spectral transfer function. Consequently manufacturing variations related to the spectral transfer function of the optical assembly can easily be identified.

7.3.4   Filters

A set of filters as shown in the mechanical assembly of **Figure 7.1** could be used during calibration.

7.3.5   Adjustable optical path length device

Figure 7.1 illustrates a hypothetical device with mirrors and optical components that can adjust the distance between the various sources and the solar-blind UV camera to be calibrated. The atmospheric environment can be controlled within this device to simulate different atmospheric conditions during calibration. This type of device is not necessarily essential, unless the camera internal processing to determine γ is calibrated.

7.3.6   Planck source

 A Planck source (similar to **Figure 3.1**) provides uniformly large targets that fill a large portion of the camera FOV. This source is suggested for the following calibration use:

- Calibration of the camera's source size estimation function (sections 3.5.6 and 4.1.7)

- Uniformity correction of the images across the entire FOV with correction factors.
- Determination of a particular camera's resolution (lines per mm) in conjunction with the filter wheel with targets.

7.3.7 True corona source

Figure 7.1 proposes two true UV corona sources, a constant and a fluctuating source. A corona UV source consists of unique spectral gas lines (wavelengths), which are not identical to a monochromator or a Planck source (section 6.2.2 , **Figure 6.1**). Therefore, to attain an accurate camera measurement, a true source is suggested as a part of calibration.

7.3.8 Adapted monochromatic source

A monochromator can be used to determine the spectral transfer function of the solar-blind camera, as described in the experiments in this investigation (section 4.1.10). Furthermore, by adding a set of filters in front of the monochromator output, it is possible to create an adjustable power output that doesn't suffer from spectral distortion of a Planck radiator when its temperature is changed.

7.4 PROPOSED CALIBRATION PROCEDURE

This section provides a brief outline of a proposed calibration procedure. Note that due to the limited space available here, not all the steps are presented and neither is the procedure fully described.

7.4.1 Initial operational spectral verification

It is suggested that as a first step that a relative spectral transfer function of the camera be determined by using a monochromator and an integrating sphere. The objective of this proposed first step is to determine if the camera that is calibrated is indeed only working in the solar-blind UV domain at an early stage. This is contrary to current methods where each camera's component is individually spectrally analysed and using the sun to determine if a camera is solar-blind [4, 13].

7.4.2 Event characterisation and adjustment

Next, event characterisation of the camera must be performed as is done by Bergamini *et al* [6]. This is similar to the description by manufacturers for Photo Multiplier Tubes (PMT) [35]. Furthermore, some camera manufacturers hinted that the events produced must be adjusted (no details provided) such that events sizes correspond between cameras [4]. It was concluded that this

adjustment is achieved by manipulating image intensifier gain, adjusting the threshold mechanisms in the electronics and finally performing adjustment of the electronics driving the image intensifier. In addition to the event size, it is concluded by the author, that the time response of events also need to be characterised for a camera. This is important because is the actual corona source is a fluctuating source. To slow events imply that the corona occurrences can be missed, leading to inaccurate UV energy measurement. The time response characterisation can be performed by a shutter, such as a chopper wheel placed between a source and the camera.

7.4.3   Lens mapping

Prior to calibration of the camera, the source to detector plane relation (mapping) must be determined. Prior to lens mapping the CCD is divided into small sectors, each containing pixels as illustrated in **Figure 2.6**. and **Figure 2.8**. Obviously these sectors must be larger than the event size such that counting can be performed (section 2.5). A source with a small area such as the monochromator output in **Figure 4.18**, together with the camera placed on a motorised X-Y mount, makes lens mapping possible. Alternative mechanical configurations and collimators can be used.

7.4.4   Creation of calibration tables

The creation of the lens map and calibration tables can be performed concurrently, if a monochromator with an adjustable output power is used. Furthermore, the calibration of a camera is preceded by the calibration of the components of the calibration bench in **Figure 7.1**. The steps creating the calibration tables as part of the suggested camera operation in **Figure 7.4** are as follows:

1. Use the reference detector to measure the spectral irradiance $E_{\lambda D1}$ of the monochromator at maximum output level, at a distance r_{D1}. This distance is shorter than the distance between the monochromator and the camera, as the camera can compensate for distance using gain.

2. Next measure the spectral irradiance $E_{\lambda D2}$ of the monochromator at a distance r_{D2}.

3. Determine the atmospheric attenuation $\gamma_{\lambda CAL}$ for the particular calibration, by using the results of step 1 and 2 and relation (5.4) followed by (2.10). Use $\gamma_{\lambda CAL}$ to determine the spectral radiance $L_{\lambda MONO}$ of the monochromator for each wavelength using relation (7.1). Perform another measurement $E_{\lambda D3}$ at a distance r_{D3} also using (2.10), (5.4), (7.1) and the distances or$_{D1}$ or r_{D2} to determine the value of $L_{\lambda MONO}$ and $\gamma_{\lambda CAL}$ more accurately if need be.

4. The next step uses an integrating sphere or the monochromator. Both are described next.
   Integrating sphere:

a. If an integrating sphere is available, place the reference detector in front of the sphere opening and measure $E_{\lambda DSPHERE}$. The measured values of $E_{\lambda DSPERE}$ (at each wavelength) can be used in conjunction with the previous step's results no. 1 to 3, which aim is to determine the sphere's spectral radiance $L_{\lambda SPHERE}$.

b. Position the camera to look into the sphere and use $L_{\lambda SPHERE}$ to determine the camera's spectral transfer function, using the values of $L_{\lambda SPHERE}$. For a particular monochromator output energy and camera, a particular pixel sector count value can be described by

$$\phi_{\lambda GS} = c_{i\_sec}.L_{\lambda SPHERE} = c_{i\_sec}.c_{\lambda SPHERE}.L_{\lambda MONO} \tag{7.4}$$

with

$\phi_{\lambda GS}$ the pixel sector count value for a particular wavelength [count.s^{-1}.m^{-2}.nm] ,

c_{i_sec} is the calibration factor per λ per sector [count.s^{-1}] ,

$L_{\lambda SPHERE}$ is the spectral Radiance of the sphere [W.sr^{-1}.m^{-2}.nm^{-1}],

$L_{\lambda MONO}$ is the spectral Radiance of the Monochromator [W.sr^{-1}.m^{-2}.nm^{-1}]
and

$c_{\lambda SPHERE}$ is a convertion factor per λ from Monochromator to sphere .

c. Calculate the camera's spectral bandwidth and the wavelength with maximum output response.   Determine if the camera's spectral response is within the expectable solar blind level

Monochromator only:

The procedure for the monochromator is similarly to that of an integrating sphere, but include parameters such as γ_λ based on (7.3).

5. Use the reference detector to measure the different output energy levels of the adjustable monochromator output, at the intended centre wavelength of the camera λ_{CS}, at any of the previous distances r_{D1} or r_{D2}. The graphs will be linear if a silicon type of reference detector is used, similar to other types of silicon detector camera calibrations [56]. Use the spectral radiance L_λ to create a relation between the detector's digital output level and $L_{\lambda MONO}$. The relation based on other solutions is postulated to be

$$DN \approx a_{\lambda MONO} A_{REFDET} L_{\lambda MONO} R_{REFDET} (\lambda_{cs}) e^{-\gamma_{\lambda CS} r} \tag{7.5}$$

where

DN is the output of the reference detector in volts [V] or ampere [A] or bits,

$a_{\lambda MONO}$ is the adjustable attenuation factor of the Monochromator,

$\gamma_{\lambda CS}$ is the atmospheric attenuation at particular wavelenght referred to as cs [nm]

A_{REFDET} is the area of the reference detector [m^2].

$L_{\lambda MONO}$ is the spectral radiance of the Monochromator [$W.sr^{-1}.m^{-2}.nm^{-1}$]

and

$R_{REFDET}(\lambda_{CS})$ is the calibrated reference detector output responsivity .

6. Create a set of non-linear numerical relations based on Fordham's [39] model, using the monochromator, considering different camera gain selections as shown in **Figure 7.2**, based on an image intensifier datasheet [36]. (Radiance simplifies scaling (section 7.4.5)).
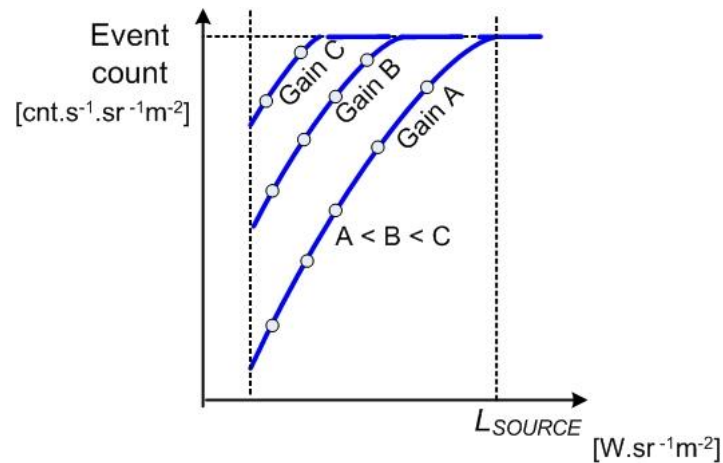
Figure 7.2. Source Radiance and event count output calibration graphs.

If a sphere is used, then measure all the pixel sector's count values and apply the correction factors from the lens mapping, creating a transfer function for each sector. If only a monochromator is used, select the pixel sector that provides the highest output to create a radiance and count relation map. Furthermore, incorporate $\gamma_{\lambda CAL}$, $L_{\lambda MONO}$ and the distance r_{cam} between the monochromator and camera as part of the count versus $L_{\lambda MONO}$.

7. Use the graph relations of 6, spectral results of the camera and the actual spectral of corona to create the camera transfer function similar to **Figure 7.2**, for the wide-band measurement of corona. The must be done to accommodate for: the corona calibration source's decay over time, temperature fluctuation, gain variations and finally, noise.

8. Verify the calibration with the actual source such as coronal source, applying correction if need be. Use the calibration reference camera if required.

7.4.5   Scaling of measurements as a part of calibration

This section provides an overview of the proposed role of scaling practical solar-blind UV energy measurements to the calibrated values. The calibration tables are created during calibration for a particular distance between the camera and the calibration source. The top left hand figure of **Figure 7.3** illustrates the input optical power from a source and the count output transfer function of an ICCD camera (section 2.5.5, **Figure 2.11**), which is measured at various distances. The calibration distance is shorter than the distance where the actual corona sources are measured. **Figure 7.3** depicts that the UV energy measured by the camera at the distance R_2 is less than the same energy at a shorter distance R_1 during calibration. This implies that any measurement must be scaled to the calibration graphs as illustrated in **Figure 7.3**, considering the following parameters:

- Distance and atmospheric attenuation (sections 2.3.3 and 2.3.2).
- Source area (section 3.3.3 and 3.5.6).
- Gain (sections 2.4.6, 3.5.5 and 4.1.5).
- Frame rate (section 3.5.2.3).
- Operating Temperature [48].
- Non Uniformity Correction (NUC) of images from the detector [48].
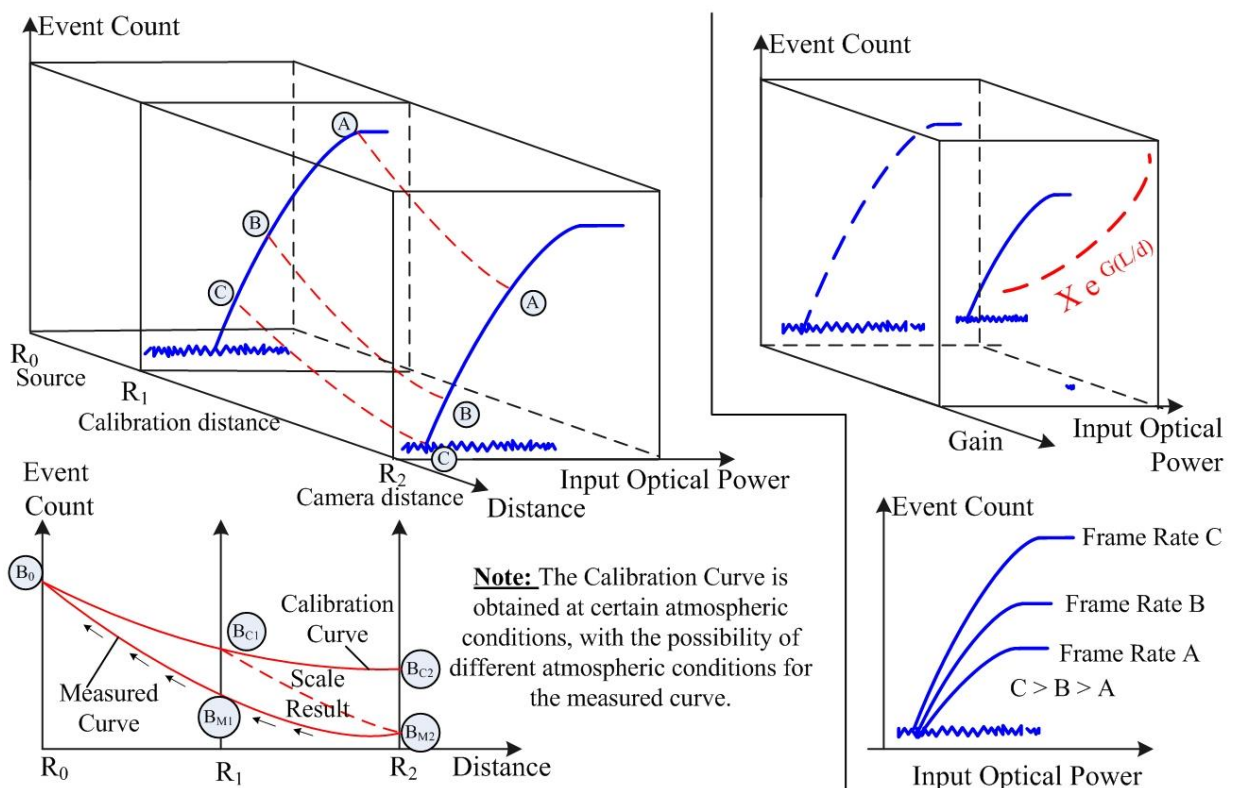
Figure 7.3. Proposed scaling of measurements to a calibration curve.

7.5   PROPOSED ENHANCEMENTS TO CAMERA OPERATION

Figure 7.4 provides a summary of the solar-blind UV camera's current and proposed alterations using counting techniques, each corresponding with a number in the figure described as follows:

1. The UV source (HVT corona) consisting of multiple wavelengths and a source area, emits energy that is measured by the solar-blind UV camera (section 2.3.1).

2. The source flux is attenuated with distance and the atmosphere's aerosols and molecules that absorbs and scatters it. Rayleigh type scattering is predominant for solar-blind UV.

3. Only a portion of the energy is detected by the optics of the camera, with a further distortion through the lens. It is proposed that a shutter form part of this optical assembly to collect background images (frames) for the purpose of eliminating noise.

4. A solar-blind UV filter ensures that only solar-blind UV energy is detected.

5. The source is weak and the solar-blind UV filter attenuates the source to such an extent that amplification is required. This amplification is only achievable with an image intensifier.

6. The anode of the intensifier can be a detector in the latest cameras, or be connected to a detector via an optical fibre or lens to a CCD or CMOS type detector.

7. The CCD or anode type detector of the intensifier provides three dimensional pulses that can be counted or be processed as analogue signals, as was done in this investigation.

8. It is proposed that the signal from the CCD be statistically analysed to ensure that no saturation occurs. The gain of the intensifier can thus be adjusted if saturation occurs.

9. It is suggested that a switch, frame accumulator and background frame store be used to capture a background frame when the shutter is closed. A subtraction of the background frame from source data is to be made possible with the control of the switch.

10. Proposed is a threshold mechanism for uniquely defined pixel sectors of the image (e.g. **Figure 2.8**). The purpose of the threshold mechanism is to define an upper and lower threshold to filter events to count for the next function.

11. Suggested is a count mechanism that counts the number of events in a pixel sector.

12. Proposed is the correction of each pixel sector count value based on the lens, non-uniformities from the intensifier, detector, fibre and other non-uniformities.

13. Proposed are summation functions to construct a source area for each pixel sector.

14. Suggested is a threshold mechanism to get values in the linear region of (2.24).

15. Proposed is a scaling function that uses the distance to source, atmospheric influence, source area and gain to determine the radiometric measurement of a sector.

16. Finally, all sectors are summed to attain a measurement of the source's UV energy.
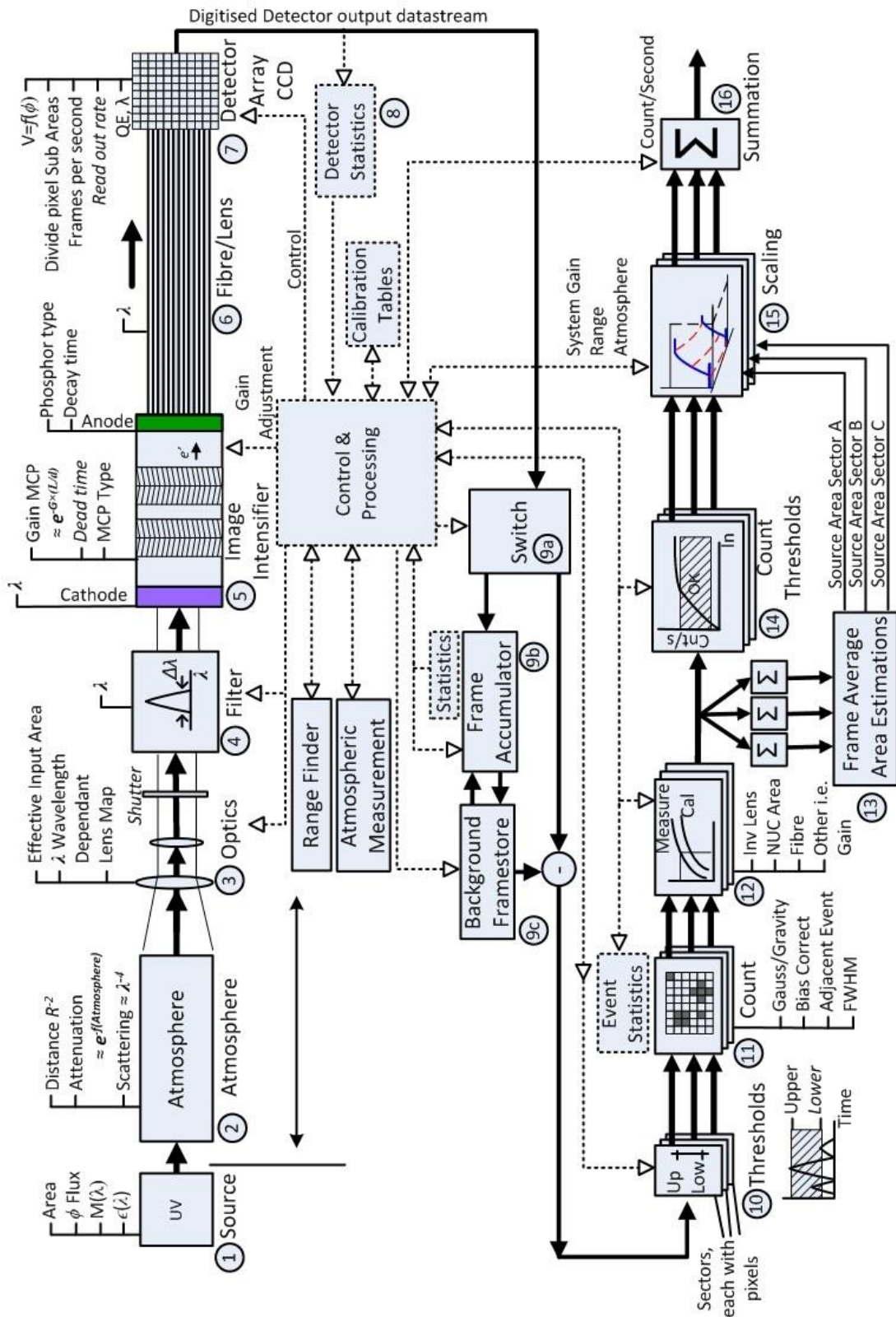
Figure 7.4. Proposed high level camera implementation.

7.6 PROPOSED FURTHER RESEARCH RELATING TO THE USE OF SOLAR-BLIND UV CAMERAS FOR HVT LINES

The solar-blind UV camera investigated is used for the inspection of a variety of high voltage equipment, for the presence of UV corona. One such an example is the inspection of High Voltage Transmission (HVT) lines as illustrated in **Figure 7.5**. Probable electrical faults are indicated by the presence of corona on a power pylon's insulator or on the conductors (wires) themselves in the HVT's case [13]. This uncertainty that an electrical problem is actually present in the presence of corona, is the problem that power distributors and the camera manufacturers are struggling with.
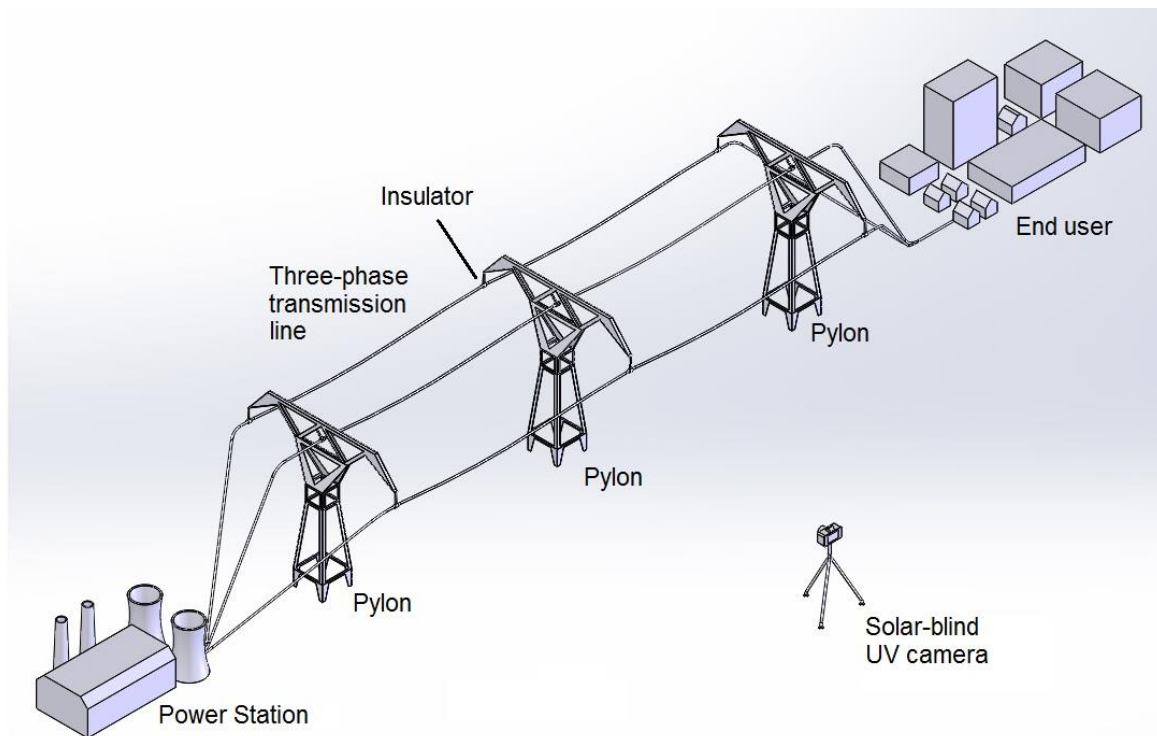
Figure 7.5. Typical practical electrical measurement scenario.

Fortunately, the results of investigations by the sample of researchers in **Table 2.2**, highlights that there is some relation between the electrical energy loss and the corona discharge as UV flux as observed by solar-blind UV cameras. Armed with the solar-blind UV camera's characteristics and studying a number of these electrical examples, a recommendation is presented here for the electrical researchers to hopefully uncover the electrical versus optical relation for this problem.

Based on **Table 2.2** that highlights by electrical and optical research in section 2.6, **Figure 7.6** illustrates what the expected electrical losses' relation to optical flux detected, could be for a power pylon.

It is assumed that there is an optical flux threshold that implies that the electrical losses need corrective repair or maintenance. A camera observing the optical flux within the solar-blind UV wavelengths must at least consider the atmospheric attenuation, distance (typically 25 to 75 metres) and the camera's design to determine the optical flux emitted at the pylon. The electrical energy loss can only be determined once the optical flux is determined accurately and reliably.
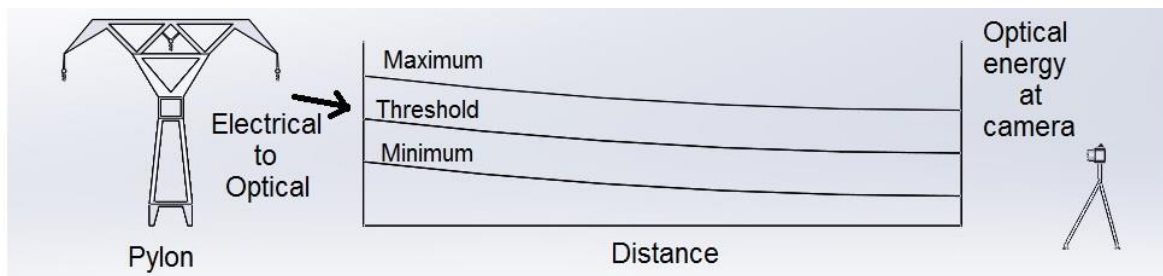
Figure 7.6. Optical flux detected on the pylon of a high voltage transmission line.

Furthermore, it is known from various power distribution models such as highlighted by Wadhwa [57], which is the fact that the voltage at the start of transmission line is not the same at the end of a HVT line. This implies that the voltage level which has an impact on the corona emission as found by researchers, also has an impact on the optical (loss) thresholds. As a result it is hypothesised that there is an optical observation plane unique for each HVT line as shown in **Figure 7.7**.
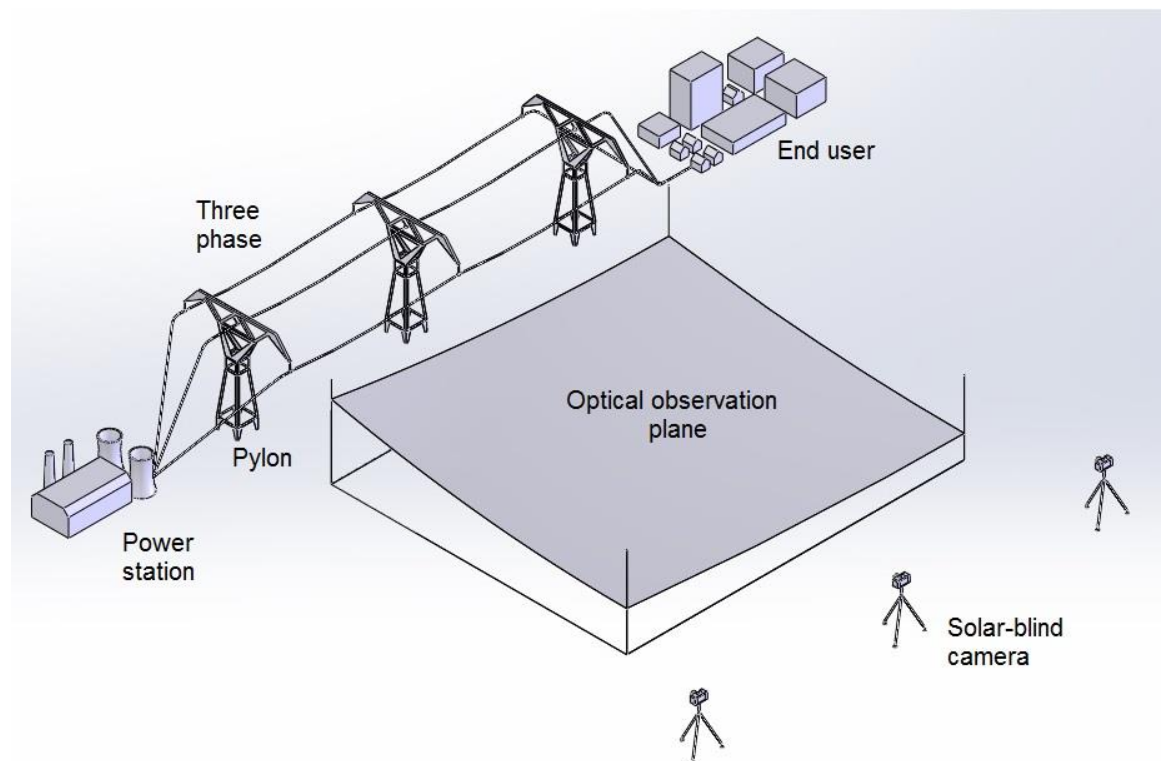
Figure 7.7. Hypothesised optical flux detection plane of a high voltage transmission line.

The actual optical flux measured by the camera currently from electrical charges in some cases are so weak that it cannot be measured at distances further than 50 metres [24 -26]. The manufacturer has subsequently embarked on new camera variants to improve the optical flux measurement.

7.7   EPILOGUE

The hypothesis that the UV radiometric measurements are influenced by its own spectral transfer function was proven, but additional factors that have an influence were uncovered with experiments. Experiments had to overcome the camera's limitations which was related to the fact that the internal camera's operation (processing) is unknown, thus a black-box. It is suggested that another type of camera that has open access to its internal processing and raw data be used, as it should provide more accurate results. Such a type of camera is referred to here as a scientific research camera, which are manufactured by others manufacturers such as Stanford Computer Optics and Princeton Instruments.

A number of recommendations were provided for further research:
- Presented was the outline of a calibration process which includes consideration for solar-blind UV camera's spectral function the atmospheric attenuation.
- Presented were ideas as to how the camera's internal processing can be adapted to perform true radiometric UV energy measurements. In addition, the camera components such as the fibre and CCD can be replaced with a delay line or capacitive technology [59], which should result in an improvement of the measurements by the camera.
- Finally, ideas were presented for future research related to the quantification of the relationship between electrical loss and the corona for a practical HVT implementation.

REFERENCES

[1]   B.J. Forney, "Spectral Analyses of Ultraviolet clutter sources to improve probability of detection in helicopter UV Missile warning systems", MSc Thesis, Naval Postgraduate School Monterey, California, 2008.

[2]   M. Lindler, S. Elstein, P Lindner, J.M Topaz and A.J Philips, "Daylight corona discharge imager", *Procedings 11ᵗʰ Int. Symposium on High Voltage Eng*, vol. 4 pp.349 -353, London , UK.

[3]   Naval Air Systems Command and Naval Air Warfare Center, *"Electronic Warfare and Radar Systems Engineering Handbook"*, 1999.

[4]   *Discussions with SAAB Grintek Electronic Defence Systems. 2011.*

[5]   M. Bass, C. DeCusatis, J. Enoch, V. Lakshminarayanan, G. Li,C. MacDonald, V. Mahajan and E. Van Stryland, *"Handbook of Optics, Volume II Design, Fabrication and Testing Sources and Detectors; Radiometry and Photometry, Third Edition"* McGraw-Hill, 2009, ISBN 9780071629270.

[6]   P.Bergamini, G. Bonelli, S. D'Angelo, S. Latorre, L. Poletto, G. Sechi, E.G. Tanzi and M. Uslenghi, "Performance evaluation of a photon counting intensified CCD", *Proceedings of SPIE - The International Society for Optical Engineering 3114*, pp. 250 - 259, 1997.

[7]   A. Boksenberg, C.I. Coleman, J. Fordham, K. Shortridge, "Interpolative Centroiding in CCD-Based Image Photon Counting Systems", *Advances in Electronics and Electron Physics*, vol. 64, Part A, pp. 33-47,1986,

[8]   K. Suhling, R.W. Airey, B.L. Morgan, "Optimisation of centroiding algorithms for photon event counting imaging", *Nuclear Instruments and Methods in Physics Research Section A: Accelerators, Spectrometers, Detectors and Associated Equipment*, vol. 437, iss. 2–3, pp. 393-418, 1999.

[9]   J.G. Bellis, D.A. Bone and J.L.A. Fordham, "A New Real-Time Centroiding Technique for Photon Detector", *Astronomic Society of the Pacific,* 103, pp. 253-257, 1991.

[10] M. Uslenghi, M. Fiorini and G. Sarri, "Wide dynamic range photon counting IICCD for ground-based astronomy", *Nuclear Instruments and Methods in Physics Research Section A: Accelerators, Spectrometers, Detectors and Associated Equipment*, vol. 518, iss. 1–2, pp. 223-225, Feb. 2004.

[11]   M.K. Carter and P.D. Read, "The implementation and performance of a connected regions centroiding algorithm for imaging photon counting", *Nuclear Instruments and Methods in Physics Research Section A: Accelerators, Spectrometers, Detectors and Associated Equipment*, vol. 510, iss. 1–2, pp. 185-189, Sept. 2003.

[12]   J.M. Bidaulta, P. Fonteb, T. Franckec, P. Galya, V. Peskovad and I. Rodionove, "A Novel UV Photon Detector with Resistive Electrodes", *Nuclear Physics B (Proc. Suppl.)*158, pp.199–203, 2006.

[13]   *Discussions with Uvirco South Africa, 2011.*

[14]   N.S Du Toit, "Calibration of UV-sensitive camera for corona detection", MSc Eng Thesis, University of Stellenbosch, 2007.

[15]   E. Hech and A. Zajac, *"Optics"* ADDISON-WESLEY.1974.

[16]   M. Bass, C. DeCusatis, J. Enoch, V. Lakshminarayanan, G. Li, C. MacDonald, V. Mahajan and Eric Van Stryland, *"Handbook of Optics Volume V Atmospheric Optics, Modulators, Fiber Optics, X-Ray and Neutron Optic, Third Edition",* McGraw-Hill, 2009, ISBN 9780071498890.

[17]   C.J. Willers, "Electro-Optical System Analysis and Design: A Radiometry Perspective", SPIE PRESS, 2013, ISBN 978081945693.

[18]   R. McClunney, "Introduction to Radiometry and Photometry". Artech House, 1994.

[19]   M. Bass, C.M. DeCusatis, J.M. Enoch,V. Lakshminarayanan, G. Li, C. MacDonald, V.N. Mahajan and E.Van Stryland, *"Handbook of Optics Volume 1 Geometrical and Physical Optics, Polarised Light, Components and Instruments",* McGraw-Hill, 2010, ISBN 9780071629256.

[20]   www.mathworks.com.

[21]   C. Frohlich and G.E. Shaw, "New determination of Rayleigh scattering in the terrestrial atmosphere", *Applied Optics*, vol.19, no.11, pp. 1773-1775, 1980.

[22]   G.C. Holst, *"Electro-Optical Imaging System Performance"*, SPIE Optical Engineering Press, 1995.

[23] *C. J. Coetzer. Work Experience: Measurement of an UVB source with an EMCCD camera, 2012.*

[24] C. Zang, H. Lei, Z. Jiang, H. Ye, S He, X. Zhao and Z. Jiang, "Study on Application of Ultra-Violet Instrument "*International Conference on High Voltage Engineering and Application, ICHVE* 2008, art. no. 4773955, pp. 391-393, 2008.

[25] W. Zhou, H. Li, X. Yi, J Tu and J. Yu, "A Criterion for UV detection AC Corona conception in a Rod-Plane Air Gap", *IEEE trans. Dielectrics and Electrical Insulation*, vol. 18, iss. 1, pp. 232–237, 2011.

[26] B. Pinnangudi, R.S. Gorur and A.J. Kroese, "Quantification of corona discharges on nonceramic insulators", *IEEE Trans. Dielectrics and Electrical Insulation*, vol.12 , no.3, pp. 513-523, 2005.

[27] R.E Jacobson, S.F. Ray and G.G. Attridge, *"The Manual of Photography, 8th Edition"*, Focal Press ISBN - 240 51268 5.

[28] A. Gerrard and J.M. Burch, *"Introduction to Matrix Methods in Optics"*, John Wiley and Sons, 1975, ISBN 0 471 29685 6.

[29] F. Nielsen, *"Visual computing: Geometry, Graphics and Vision"*, Charles River Media, 2005.

[30] Q. Wu, F. Zhu, Y. Hao and L. He, "Virtual Camera Based a Novel Calibration without Modelling", *IEEE International Conf. Control and Automation*, pp. 3230-3234, 2007.

[31] T. Sentenac, Y. Le Maoultt, G. Rolland and M. Devy, "Temperature Correction of Radiometric and Geometric Models for an Uncooled CCD Camera in the Near Infrared", *IEEE Trans. Instrumentation and Measurement*, vol. 52, no. 1, Feb 2003.

[32] Z. Ji , J. Du , J. Fan and W. Wang, "Gallium oxide films for filter and solar-blind UV detector", *Optical Materials*, vol 28 pp.415–417, 2006.

[33] M. Bass, C. DeCusatis, J. Enoch, V. Lakshminarayanan, G. Li,C. MacDonald, V. Mahajan and E. Van Stryland, *"Handbook of Optics, Volume II Design, Fabrication and Testing Sources and Detectors; Radiometry and Photometry, Third Edition"*, McGraw-Hill, 2009, ISBN 9780071629270.

[34] D. Dussaulta, P. Hoess,"Noise performance comparison of IICCD with CCD and EMCCD cameras", *Proceedings of SPIE - The International Society for Optical Engineering* 5563, art. no. 35 , pp. 195-204, 2004.

[35] www.hamamatsu.com, "Photo Multiplier Tubes, Basics and Applications, Third edition", retrieved 2011.

[36] www.hamamatsu.com ,"Image Intensifiers", retrieved 2011.

[37] J.L. Wiza, "Microchannel Plate Detectors", *Nuclear Instruments and Methods*, vol. 162, pp.587-601, 1979.

[38] N. Kishimoto, M. Nagamine, K. Inami, Y. Enari and T. Ohshima, "Lifetime of MCP–PMT", *Nuclear Instruments and Methods in Physics Research Section A: Accelerators, Spectrometers, Detectors and Associated Equipment*, vol. 564, iss. 1, pp. 204-2111, 2006.

[39] J.L.A. Fordham, C.F. Moorhead and R.F. Galbraith, "Dynamic-range limitations of intensified CCD photon-counting detectors", *Monthly Notices of the Royal Astronomical Society*, vol. 312, iss. 1, pp 83–88, Feb. 2000.

[40] C.L. Joseph, "UV image sensors and associated technologies" *Experimental Astronomy* 6 (1-2), pp. 97-127, 1996.

[41] W.K. Pratt, *"Digital Image Processing, 4th Edition"*, Wiley-Interscience, 2007, ISBN 978-0-471-76777-0.

[42] R.C. Gonzalez and R.E. Woods, *"Digital Image Processing: Third Edition",* Pearson International Education. ISBN 013505267-X, 2008.

[43] J.C. Dainty and R. Shaw,*"Image Science: principles analysis and evaluation of photographic-type imaging processes"*, Academic Press, 1974.

[44] *http://www.cis.rit.edu/class/simg713/notes/chapt5-photon, 2006.*

[45] S.M. Gubanski, A. Dernfalk, J. Andersson and H. Hillborg, "Diagnostic Methods for Outdoor Polymeric Insulators", *IEEE Trans. on Dielectrics and Electrical Insulation*, vol. 14, No. 5; pp. 1065-1080, Oct. 2007.

[46] R. Dai, F.Lu, S. Wang, "Relation of composite insulator surface discharge ultraviolet signal with electrical pulse signal", *International Conference on Electrical and Control Engineering (ICECI),* pp. 282 -285, Sept 2011

[47] C.J. Coetzer, "Aspects that need to be considered for the calibration of Ultraviolet Solar-blind cameras used for electrical inspection", *International Conference of the Insulator News & Market Report (INMR), Vancouver,* 2013.

[48] *C.J. Coetzer. Work experience: Kenis cooled thermal imager , Denel Dynamics, 2002- 2005*

[49] www.e2v.com, Data sheet. CCD97-00 Back Illuminated 2-Phase IMO Series Peltier Pack Electron Multiplying CCD Sensor, retrieved 2012.

[50] *C. Coetzer. Discussion with E2V, UK. 2009.*

[51] *C. Coetzer, Development report notes, Casel: 20 – 200 kHz Spectrum Analyzer, 1993.*

[52] L. Van Schalkwyk,W.E. Meyer, F.D. Auret, J.M. Nel, P.N.M. Ngoepe and M. Diale,"Characterization of AlGaN-based metalsemiconductor solar-blind UV photodiodes with IrO_2 Schottky contacts", *Physica B: Condensed Matter.* vol.407, iss.10, pp. 1529-1532, 2012.

[53] *Removed*

[54] R. Stolper, J. Hart and N Mahatho, "The design and evaluation of a Multi-Spectral Imaging Camera for the inspection of transmission lines and substation equipment", *International Conference of the Insulator News & Market Report (INMR), Hong Kong,* 2005.

[55] J.Wiza, "Micro Channel Plate Detectors", *Nuclear Instruments and Methods,* vol. 162, pp. 223-225, 1997.

[56] G Chander, B.L Markham, D L Helder, "Summary of current radiometric calibration coefficients for Landsat MSS, TM, ETM+, and EO-1 sensors", *Remote sensing of Environment*, Vol. 113 , pp. 893-903, 2009.

[57] F.Grum and L.F Costa, "Spectral Emission of corona discharges", *Applied Optics*, vol. 15, no. 1, pp76-79, 1976.

[58] C.L Wahhwa, "*High voltage engineering,3d edition*", New Age, 2010.

[59] O.H.W. Siegmund, A.S. Tremsin J.V. Valerga, "Advanced MCP sensors for UV/visible astronomy and biology", *Nuclear Instruments and Methods in Physics Research Section A: Accelerators, Spectrometers, Detectors and Associated Equipment*, vol. 510, iss. 1-2, pp 185-189, Sept. 2003.

APPENDIX

A.1. SOLAR-BLIND SPECTRUM

Solar-blind UV within the earth's atmosphere forms part of the UVC wavelengths as shown in **Figure A.1** [3]. The earth's ozone layer and other atmospheric gasses attenuate wavelengths in the UVC and extremely short UV wavelengths from the sun such that the sun radiation is not visible [1-4]. Solar-blind UV boundaries are defined to be from approximately from 180 nm to 280 nm the UVC and extreme UV wavelengths from the sun such that the sun radiation is not visible [4].
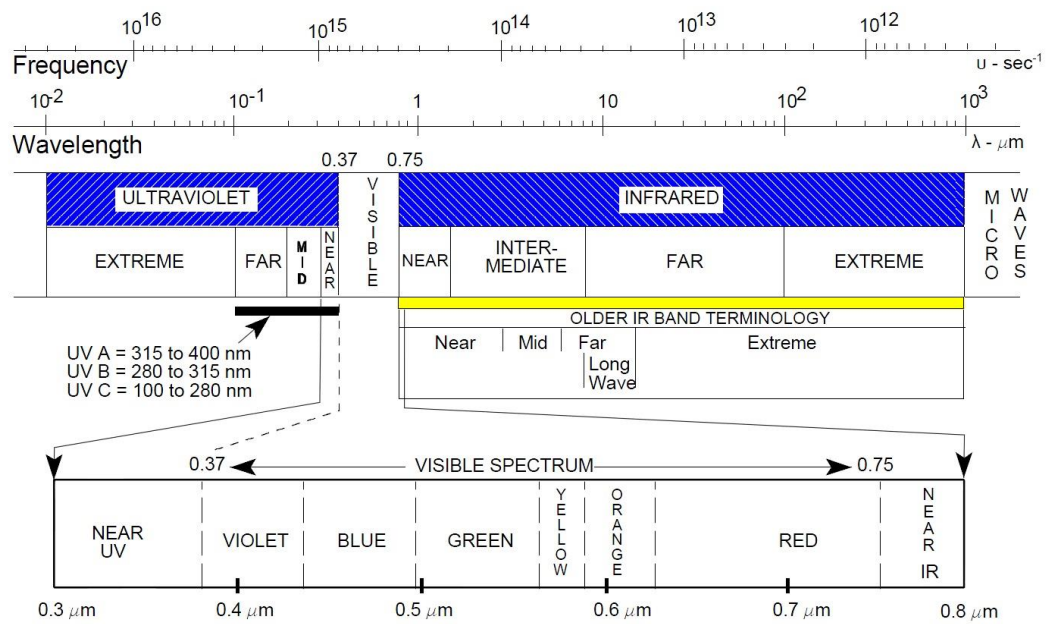
Figure A.1. Solar-blind UltraViolet (UV C) within the optical spectrum from [3].

A.2. SUMMARY OF THE RADIOMETRIC AND PHOTOMETRIC UNITS

Table A.1 and **Figure A.2** provide a summary of the different radiometric and photometric nomenclature. Photometry is only related to the energy within the wavelengths that humans can perceive with their eyes, whereas radiometry considers the energy at all wavelengths.

Table A.1. Summary of Radiometric and Photometric units compiled from [5], [17] and[18].

Quantity & Symbol	Photometric units	Radiometric units	Radiometric photons units
Energy Q	lumen-second [lm.s]	joule [J]	photons or [q]
Flux Φ	lumen [lm]	Watt [W] or alternatively [J/s]	photons per second [q/s]
Spectral emittance M_λ		$[W.m^2.nm^{-1}]$	$[q.\,s^{-1}.m^{-2}.nm^{-1}]$
Emittance M	$[lm.m^{-2}]$	$[W.m^{-2}]$	$[q.s.m^{-2}]$
Spectral intensity I_λ		$[W.sr^{-1}.nm^{-1}]$	$[q.s^{-1}.sr^{-1}.nm^{-1}]$
Intensity I	Candela ,cd, $[lm.sr^{-1}]$	$[W.sr^{-1}]$	$[q.s^{-1}.sr^{-1}]$
Spectral radiance L_λ		$[W.\,m^{-2}.sr^{-1}.nm^{-1}]$	$[q.s^{-1}.m^{-2}.sr^{-1}.nm^{-1}]$
Radiance L	nit=nt=$[lm/(m^2.sr)]$	$[W.\,m^{-2}.sr^{-1}]$	$[q.s^{-1}.m^{-2}.sr^{-1}]$
Spectral irradiance E_λ		$[W.m^{-2}]$	$[q.s^{-1}.m^{-2}.nm^{-1}]$
Irradiance E	Lux=lx=$[lm.m^{-2}]$	$[W.m^{-2}]$	$[q.s^{-1}.m^{-2}]$
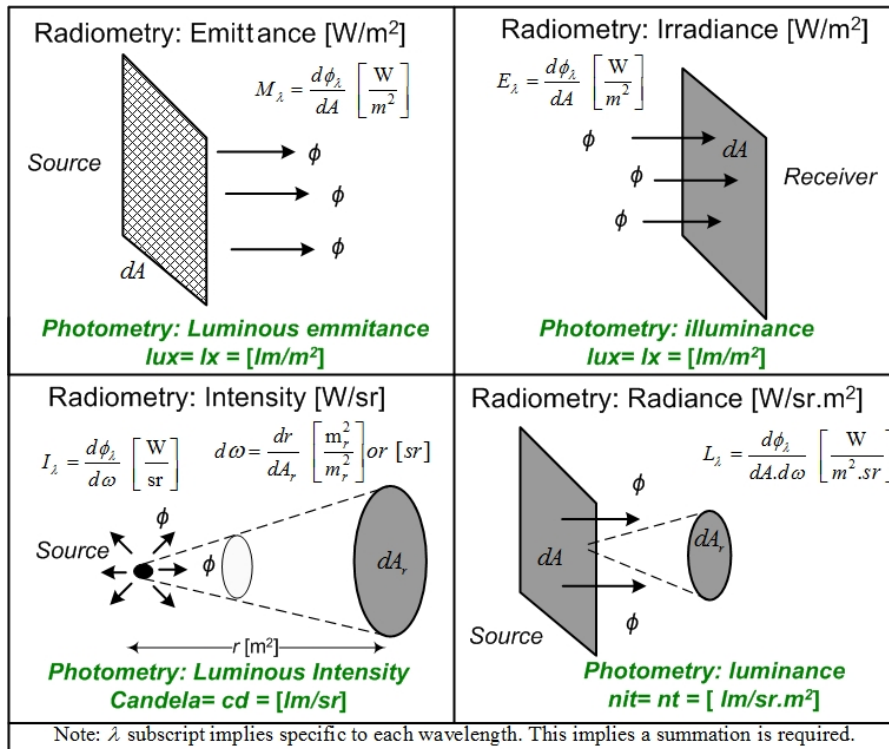
Figure A.2. Pictorial descriptions of radiometry from [5],[17] and [18].

A.3.   CODE LISTING FOR A SIMPLIFIED CAMERA MODEL

```matlab
%% Start of Matlab code file. =========================================

%-----------------------------------------------------------------------
% File_name : ThreeCamera.m                        Author/s : C J Coetzer
%
%  Description: Simplified model comparing 3 camera spectral response
%  Camera Lens diameter 62 mm placed 2 metres from a Planck Source with 22,2mm
%  diameter. Investigate spectral Narrow -, wide - , Gauss spectral response.
%  Use filter equations to model the spectral tranfer function of cameras.
%-----------------------------------------------------------------------
%23456789012345678901234567890123456789012345678901234567890123456789012345678901234567890
%         1         2         3         4         5         6         7         8
%-----------------------------------------------------------------------
%
%
%%
%  Mcode starts
clear ;         % cleared simulation memory to avoid problems
display ('  ========================================================== ');
display ('  ThreeCamera.m   ');
%% ----------------------------------------------------------------------
% Array of wavelengths represent by …………………………
display ('  Create array of nm Wavelengths ');
wl = 100:0.01:1500; % wavelengths 100nm to 1500nm (or 1.5um)

%% ----------------------------------------------------------------------
%   wl array
display ('  Set the max wavelength to do calculation at max of 1.5 um ');
wl_end = 1500;
strtvalue =1;
wl_size_array =(size(wl));
wl_long_array = max(wl_size_array);

for x=strtvalue:wl_long_array
 if wl(x)>=wl_end;
    break;
 end;
end;
  StopsIntegral =x;
%% ----------------------------------------------------------------------
% Empty array to get size
disp (' Empty array for size ');
% create a few dummy values .....for filter that is only to get array size
tsup = 0.0; % Camera response in non-pass suppression
tpass = 1;   % Camera relative response pass band
wl_cf_nm = 0.260 * 1000;% Camera peak wavelength in centre
shape = 2 ; %  Gauss Shape
wl_width_nm = 0.04*1000; % pasband width [nm]
Ffilt_dum_nm = FILTER(wl,wl_cf_nm,wl_width_nm,tpass,tsup,shape);
%%----------------------------------------
% multidimensional array  3 Cameras created
disp (' Make an empty Camera array  ');
CamSpectrals = rand(max(size(wl)),3);
CamSpectrals(:,:) =0;

disp (' Create three Camera arrays with spectral responses ');
%1)Gauss shaped camera response
wl_cf_nm = 0.260 * 1000;% Centre wavelength
shape = 2 ; % Shape gauss  2
wl_width_nm = 0.025*1000; % width in nm of pass band
```

Department of Electrical, Electronic and Computer Engineering   91
University of Pretoria

```matlab
CamSpectrals(:,1) = FILTER(wl,wl_cf_nm,wl_width_nm,tpass,tsup,shape);

%2)Make wide band camera response
wl_wcf_nm = 0.235 * 1000;% Centre wavelength
wl_width_nm = 0.09*1000; % Spectral width in nm
shape = 1E6 ; % Shape Square when large
CamSpectrals(:,2) = FILTER(wl,wl_wcf_nm,wl_width_nm,tpass,tsup,shape);

%3) Make Narrow camera response
wl_width_nm = 0.01 * 1000;
wl_cf_nm = 0.260*1000;% Centre wavelength pass band
                      % Shape as was Square when large
CamSpectrals(:,3) = FILTER(wl,wl_cf_nm,wl_width_nm,tpass,tsup,shape);
Ffilt_dum_nm=CamSpectrals(:,1);


%%------------------------------------------------------------
% Plotting the three camera response
display ('  Plotting  three Camera spectral tranfers functions ');
figure(20);

plot(wl ,CamSpectrals(:,1),'r',...
    wl,CamSpectrals(:,2),':k',wl,CamSpectrals(:,3),'--b','LineWidth',1.5);
legend('Camera_G_A_U_S_S','Camera_W_I_D_E','Camera_N_A_R_R_O_W',2);
axis([160 300 0 1.05]);
 grid on;
xlabel(' Wavelenght[nm] '); %  x axis
ylabel(' Relative Response (Max 1)'); % y axis
title('Three Camera Spectral Transfer functions ');% The graph's label

%% ------------------------------------------------------------
graphstotal =3;

for GraphNo = 1 : graphstotal
    Ts_steps =10;
    Ts_Cstrt =900;                 % Source Celsius where starts
    Ts_strt = Ts_Cstrt + 273.16;
    Ts_Cmax =1200;                 % Source Celsius where stops
    Ts_max = Ts_Cmax + 273.16;

    graphsteps = (Ts_max-Ts_strt)/Ts_steps;
    stepNo  =1;
    Totalcalc = rand(graphsteps+1,1);
    Totalcalc(:) = 0;
    Txi = Totalcalc;

for Tsource = Ts_strt:Ts_steps:Ts_max
   Txi(stepNo)=Tsource;
%------------------------------------------------------------
% Planck's law in  radiant emittance at  wavelength
% parameters:
display ('  Create Planck Source''s array values ');

M_source =PLANCK_EL_nm(wl,Tsource);     % Create source emittance [W/m^2]
L_source = M_source/pi;          % Thus source radiance ..emmisivity is 1
%------------------------------------------------------------
  D_src = 22.2e-3 ;               % Diameter circular source  [m^2]
  A_src = (pi *((D_src)^2))/4;   % Source area
  A_lns = (pi *((62e-3)^2))/4; % Area of camera lens
  Rdistance=20;                    % Distance between source and camera
 % Part outside the integral
  Tot_constant =((1e-4)*A_src)/((Rdistance*Rdistance));
    % integral portion of the source.............
```

Department of Electrical, Electronic and Computer Engineering
University of Pretoria

92

```matlab
 Tot_integral =0;        % - Init the current to zero for the loop...

strtvalue=1;               % Index to 0

for x=strtvalue:StopsIntegral
                                              %Only the radiance and
                                              %   Responsivity
    Tot_integral = Tot_integral+( L_source(x)*CamSpectrals(x,GraphNo));
                                              % ..usually filter and
                                              % atmospheric transmittance also but
                                              % they are unity (=1) in this case
end

 Totalout=  Tot_constant * Tot_integral; % Ouput = constant x Integral
 Totalcalc(stepNo) = Totalout;
 stepNo=stepNo+1;                                              % window

%
end;
  Id_Graph(:,GraphNo)=Totalcalc;
end;
%%
 display ('  Plot Source BB versus Irradiance  ');
figure(12);
 plot(Txi,Id_Graph(:,1),'r',Txi,Id_Graph(:,2),':k',Txi,Id_Graph(:,3),'--
b','LineWidth',1.5);
 grid on;
legend('Camera_G_A_U_S_S_2_6_0_n_m','Camera_W_I_D_E_B_A_N_D','Camera_N_A_R_R_O_W'
,2);
 xlabel(' Planck Source Energy in terms of Absolute Temperature[K] '); %  x
label
 ylabel('Irradiance E [W.cm-2]'); % y label
 title(' Energy detected by three different Camera Spectral Responses');%  The
graph's label

 disp(' done calculation');

%% Printout for Evaluation ... this is to compare with calibration
%   of Uvirco
% put values in a spreadsheet
    Ts_steps =10;
    Ts_Cstrt =900;
    Ts_strt = Ts_Cstrt + 273.16;
    Ts_Cmax =1200;
    Ts_max = Ts_Cmax + 273.16;

    graphsteps = (Ts_max-Ts_strt)/Ts_steps;
    stepNo  =1;
    Totalcalc = rand(graphsteps+1,1);
    Totalcalc(:) = 0;
    Txi = Totalcalc;
    stepNo=1;
    z= Ts_Cstrt;
    disp(' ----------------------------------------------');
    disp(' Planck Temp   E [W/cm^2]        E [W/cm^2]      E  [W/cm^2]');
    disp(' Temp C    Gauss shape    Wide 190to280nm   Narrow response');
for zshow=Ts_Cstrt:10:Ts_Cmax
    disp(sprintf(' %d     %E  %E  %E ',zshow...
         ,Id_Graph(stepNo,2),Id_Graph(stepNo,2),Id_Graph(stepNo,3)));
     stepNo=stepNo+1;
end;
```

Department of Electrical, Electronic and Computer Engineering   93
University of Pretoria

```
%% =========================================================
%% The Source energy description
%   PLANCK_EL_nm.M
% Planck's law radiant emittance
% operate in the nm range
% input :
% w = wavelength vector in  [nm]
% t_Kelvin = temperature scalar in [K]
% Note  10^3 to compensate for the nm scale
% returns :
% spectral emittance [W/m^2.nm]

function y=PLANCK_EL_nm(w,t_Kelvin)

y= 3.7418301e20 ./ (w .^ 5 .* ( exp(14387863.142 ./(w * t_Kelvin))-1));


%   FILTER.M
%% =========================================================
% function in matlab
% Calculate Transmittance of filter
%  um wavelenght or for nm use * 1000
% input values:
% wl  array of wavelenghts
% tsup = 0.0; Camera response in non-pass suppression
% tpass = 0.8;   % Camera relative response passband
% wl_wcf_nm Centre wavelenght passband
% shape = 2 ; % Shape gauss when2
% wl_wide = 0.02 % width in nm of passband

function y=FILTER(wl,wl_wcf_nm,wl_wide,tpass,tsup,shape)
y = tsup +tpass*exp(-(2*(wl -wl_wcf_nm)/wl_wide).^shape); % formula
```

A.4.   SPECIFICATIONS OF INSTRUMENTS USED FOR EXPERIMENTS

Table A.2. Abstract from the specifications of the Corocam 504, a solar-blind UV camera.

UV FOV	
UV Field of View , horisontal and vertical observation angle in degrees.	8° by 6°.
Solar-blind UV specification	
Minimum focal distance for UV.	2 [m]
Solar-blind UV operating spectrum bandwidth.	240 to 280 [nm]
Minimum detectable solar-blind UV energy.	$3.0 \text{ E}10^{-18}$ [W.cm^{-1}]
Available camera UV image processing	
Adjustable UV event counter update rate.	0.02 to 2 [s]
Counter's display update rate.	4 [s]
Integration (Attack) and degradation (Decay).	Both On and off selectable, value adjustable in terms of a percentage.
Image Noise removal.	Convolution.
UV Event Count method.	Blob counter.
Image size	
Image resolution (horizontal by vertical pixels).	640 by 480 pixels

Table A.3. A summary of the equipment used in the experiments.

No	Items	General Information
1	Uvirco's Corocam 504	Solar-blind UV camera from Uvirco. Successor of the Corocam IV used by Du Toit[14].
2	Uvirco's Corocam 6	Successor of the Corocam 504.
3	Personal Computer (PC)	Intel i7, 8 GByte DDR3, Windows 7 ,64 bit.
4	Analogue PCI image capture Card	dPict-Image Pro. Eight bit analogue video capture card.
5	Planck Source	Maximum temperature 1200°C.
6	Point Source lamp	UV focusing lamp.
7	Measuring Tape	
8	Tripod	Camera mounting stand.
9	Image Pro-Plus 7	Image processing software.
10	Matlab ©	Modeling software.
11	Microsoft © Excel 2007	General processing.
12	Chezy-Turner monochromator	Non-linear wavelength selectable source.
13	Reference Detector	Calibrated CMOS reference detector.

A.5.   CODE LISTING FOR EVALUATING SOURCE SIZE

```matlab
%% Start of Matlab code file. ================================================

%-----------------------------------------------------------------------------
% File_name : SizeTifC504v2.m                      Author/s : C J Coetzer
%
%   Description: Analyses the tiff files captured for experiments and shows the
%   values as it is analysed for a BB target. for different sizes
%-----------------------------------------------------------------------------
%23456789012345678901234567890123456789012345678901234567890123456789012345678890
%        1         2         3         4         5         6         7         8
%-----------------------------------------------------------------------------
%
%
%%
%  Matlab code starts
display ('  ======================================================= ');
display ('  File = SizeTifC504.m Evaluating different target sizes ');
clear ;       % clear simulation memory to avoid problems

%%
% Get image and the Background

display ('  ======================================================= ');
display ('  1. Get the Background from the file image and plot ..Busy');
for i=1:200,
Src_Tiff(:,:,i)=uint32(imread('c:\13April\x17BbckD0R0x1A14ay14g62t1220TR38.tiff',
i));end;
```

```matlab
% Set the image sizes according to pic
ImageSize = size(Src_Tiff);
NoRows = ImageSize(1);
NoCol = ImageSize(2);
noFrames = ImageSize(3);
%%
% Calculate background value from the data and plot it
vSumBck = uint32(zeros(NoRows,NoCol));
for Loopcnt=1:1:noFrames vSumBck= vSumBck+Src_Tiff(:,:,Loopcnt); end;
figure(1);imagesc(vSumBck); figure(gcf);
colormap(gray);
title('Background : Attack 14% Decay 14% Gain 62% Distance 2 Meters');% main
graph label
%% -------------------------------------------------------------------
% Do the 22.2mm source area ...
TheTitle = 'Diameter 22 mm';
ui16vSumImage=Getandplot2('c:\13April\x14B1200D22R2x1A14ay14g62t1212TR38.tiff',vS
umBck,TheTitle,noFrames,2,2,2,1)
% Add all the pixel values
subtotal=sum(uint32(ui16vSumImage)); % first get all the columns
Val22mm= sum(subtotal);            % final solution
% Do a 3 d plot
figure(21);surfl(ui16vSumImage); figure(gcf);colormap(gray);
title('Source 22mm diameter 3d plot');% main graph label
%% -------------------------------------------------------------------
% Do the 15 mm source area ...
TheTitle = 'Diameter 15 mm';
ui16vSumImage=Getandplot2('c:\13April\x19B1200D15R2x1A14ay14g62t1226TR38.tiff',vS
umBck,TheTitle,noFrames,2,2,2,2)
% Add all the pixel values
subtotal=sum(uint32(ui16vSumImage)); % first get all the columns
Val15mm= sum(subtotal);            % final sum for 15 mm diameter of all pixels
%% -------------------------------------------------------------------
% Do the 12 mm source area ...
TheTitle = 'Diameter 12 mm';
ui16vSumImage=Getandplot2('c:\13April\x18B1200D12R2x1A14ay14g62t1223TR38.tiff',vS
umBck,TheTitle,noFrames,2,2,2,3)
% Add all the pixel values
subtotal=sum(uint32(ui16vSumImage)); % first get all the columns
Val12mm= sum(subtotal);            % final sum for 12 mm diameter of all pixels
%% -------------------------------------------------------------------
% Do the 9 mm source area ...
TheTitle = 'Diameter 9 mm';
ui16vSumImage=Getandplot2('c:\13April\x21B1200D9R2x1A14ay14g62t1237TR38.tiff',vSu
mBck,TheTitle,noFrames,2,2,2,4)
% Add all the pixel values
subtotal=sum(uint32(ui16vSumImage)); % first get all the columns
Val9mm= sum(subtotal);              % final sum for the 12 mm diameter of all
pixels
% Do a 3 d plot
figure(22);surfl(ui16vSumImage); figure(gcf);colormap(gray);
title('Source 9mm diameter 3d plot');% main graph label
%% Initiliase plot array
Plotarray=[ 9 12.7 15 22.2 ; 0 0 0 0 ; 0 0 0 0; 0 0 0 0 ; 0 0 0 0];
%% Get values into the plot array of values read
Plotarray(2,1)= Val9mm;
Plotarray(2,2)= Val12mm;
Plotarray(2,3)= Val15mm;
Plotarray(2,4)= Val22mm;
%% Number ratio for value measured
Plotarray(3,1)=Plotarray(2,1)/Plotarray(2,4);
Plotarray(3,2)=Plotarray(2,2)/Plotarray(2,4);
Plotarray(3,3)=Plotarray(2,3)/Plotarray(2,4);
```

```matlab
Plotarray(3,4)=Plotarray(2,4)/Plotarray(2,4);
%% calulate source areas...
Plotarray(4,1)=pi*(Plotarray(1,1)^2);
Plotarray(4,2)=pi*(Plotarray(1,2)^2);
Plotarray(4,3)=pi*(Plotarray(1,3)^2);
Plotarray(4,4)=pi*(Plotarray(1,4)^2);
%% Number ratio for source areas measured
Plotarray(5,1)=Plotarray(4,1)/Plotarray(4,4);
Plotarray(5,2)=Plotarray(4,2)/Plotarray(4,4);
Plotarray(5,3)=Plotarray(4,3)/Plotarray(4,4);
Plotarray(5,4)=Plotarray(4,4)/Plotarray(4,4);
%% Plot the source areas and values with ratios
 figure(45);
 plot(Plotarray(1,:) ,Plotarray(3,:),'-or',...
      Plotarray(1,:) ,Plotarray(5,:),'--xb',...
      'LineWidth',1.5);
legend('Source Area / Max Source Area',...
'Source Measured / Max Source Measure',1);
axis([8 24 0 1.2]);
grid on;
xlabel(' Source Diameter [mm] '); % add a name to the x axis
ylabel(' Area or Measured Value:   Source/Maximum '); % y axis name
%% Perform a 3 d plot of one of the results…
figure(7);surfl(ui8vSumImage); figure(gcf);colormap(gray);
```

A.6. MONOCHROMATOR POWER OUTPUT PER WAVELENGHT
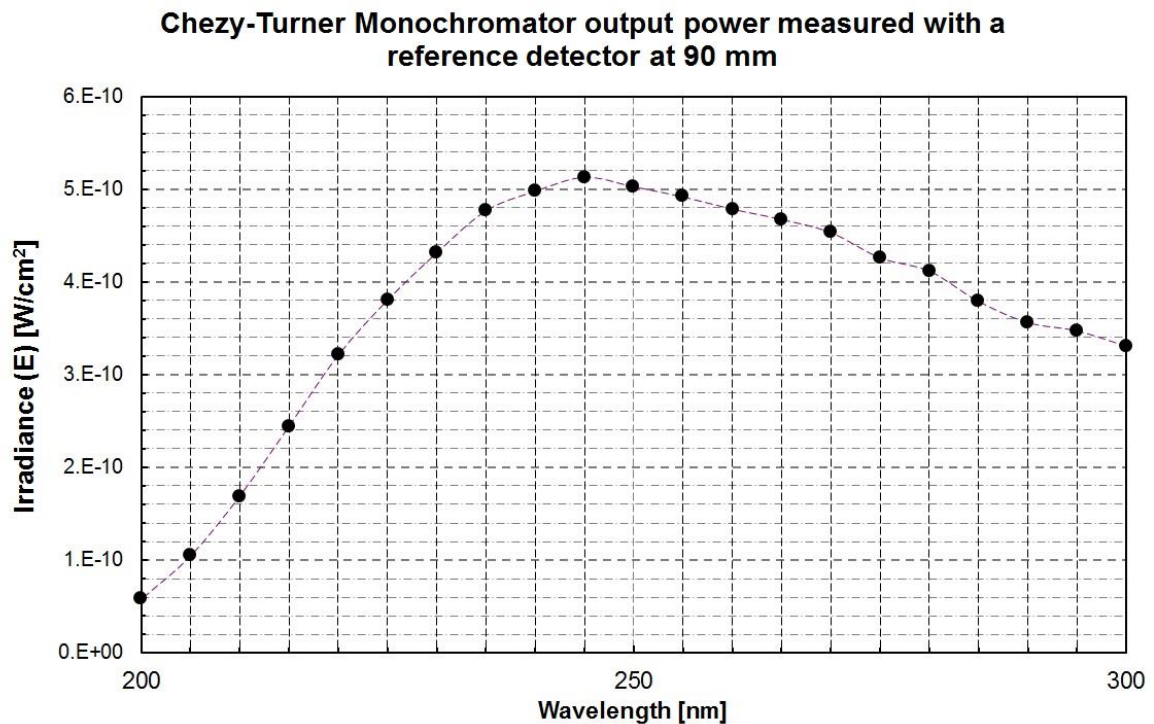
Figure A.3. Chezy-Turner monochromator power output as measured with a reference detector.

Table A.4. Monochromator Correction Values within the Solar-Blind UV wavelengths

Wavelength[nm]	Correction factor
235	0.929632
240	0.970698
245	1
250	0.979919
255	0.958782
260	0.93306
265	0.911235
270	0.883713
275	0.830424
280	0.802675
285	0.738711

A.7. MATLAB CODE : CAMERA OUTPUT RESPONSE FOR MEASURED SPECTRUM

```matlab
%% ++++++++++++++++++++++++++++++++++++++++++++++++++++++++++++++++++++++++
%% Start of Matlab code file. =============================================

%-------------------------------------------------------------------------
% File_name : ModelActualCompare.m                    Author/s : C J Coetzer
%
%   Description :  Compares the actual measured spectrum with thre
%   postulated camera responses.
%-------------------------------------------------------------------------
%2345678901234567890123456789012345678901234567890123456789012345678901234567890
%        1         2         3         4         5         6         7         8
%-------------------------------------------------------------------------
%
%%
%  Matlab code starts
clear ;         % clear simulation memory to avoid problems
%%
% Collect the case picture and show it
display ('  ------------------------------------------------------------- ');
display ('  ModelActualCompare.m  simplified model compare cameras spectrum ');
%% -----------------------------------------------------------------
% Array of wavelengths represent by …………………………
display ('  Create array of nm Wavelengths ');
wl = 100:0.01:1500; % wavelengths 100nm to 1500nm (or 1.5um)

%% -----------------------------------------------------------------
%  wl array
display ('  Set the max wavelength to do calculation at max of 1.5 um ');
wl_end = 1500;                    % Max wavelength
                                 % in terms of nm ...this is selected as 1um
strtvalue =1;
wl_size_array =(size(wl));        % Analyse the wavelength array ...
wl_long_array = max(wl_size_array);  %
                                     %

for x=strtvalue:wl_long_array        %
 if wl(x)>=wl_end;                   %
    break;
 end;
end;
  StopsIntegral =x;                  % - Calculated number of steps for integral

%% -----------------------------------------------------------------
% Empty camera wavelenght array to get size
disp (' Empty array for size ');
tsup = 0.0;  % Camera response in non-pass suppression
tpass = 1;   % Camera relative response pass band
wl_cf_nm = 0.260 * 1000;% Camera peak wavelenght in centre
shape = 2 ; % Gauss shape 2, Square shape if large
wl_width_nm = 0.04*1000; % pasband width [nm]
Ffilt_dum_nm = FILTER(wl,wl_cf_nm,wl_width_nm,tpass,tsup,shape);
%%-------------------------------------------
% multidimensional array  3 Cameras created
disp (' Empty Camera array  ');
CamSpectrals = rand(max(size(wl)),3);
CamSpectrals(:,:) =0;

%1)Gauss shaped camera response
```

Department of Electrical, Electronic and Computer Engineering   99
University of Pretoria

```matlab
wl_cf_nm = 0.260 * 1000;% Centre wavelenght
shape = 2 ; % Shape gauss  2
wl_width_nm = 0.025*1000; % width in nm of passband
CamSpectrals(:,1) = FILTER(wl,wl_cf_nm,wl_width_nm,tpass,tsup,shape);

%2)Make wide band camera response
wl_wcf_nm = 0.235 * 1000;% Centre wavelenght
wl_width_nm = 0.09*1000; % Spectral width in nm
shape = 1E6 ; % Shape Square when large
CamSpectrals(:,2) = FILTER(wl,wl_wcf_nm,wl_width_nm,tpass,tsup,shape);

%3) Make Narrow camera response
wl_width_nm = 0.01*1000;
wl_cf_nm = 0.260 * 1000;% Centre wavelenght pass band
                       % Shape Square when large
CamSpectrals(:,3) = FILTER(wl,wl_cf_nm,wl_width_nm,tpass,tsup,shape);
Ffilt_dum_nm=CamSpectrals(:,1);


%------------------------------------------------------------
%% ----------------------------------------------------------------------
% Actual Camera measured response
display ('  Measured Corocam 504 spectral response ');
DLanalogue = [0 0 20 40 60 120 160 190 157 115 55 35 15 0 0 0 0];
actual_nm = [100 230 235 240 245 250 255 260 265 270 275 280 285 290 295 300
1500];
figure(24);
plot(actual_nm ,DLanalogue,'r');
legend('Corocam_5_0_4');
xlabel(' Wavelenght [nm] '); %  x  label
ylabel('  Analogue Value'); % y label
title('Spectral response Corocam ');%  The graph's label
%%
display ('  Assume that the maximum throughput is 10%, adapt the data ');
DL_normalised = (DLanalogue./190).*0.1; % Normalise al values to maximum
figure(30);
plot(actual_nm ,DL_normalised,'r');
legend('Corocam_5_0_4');
xlabel(' Wavelenght [nm] '); %  x  label
ylabel('  Digital Value'); % y label
title('Normalised Corocam Spectral response  ');%  The graph's label
%%
Coro_Spect = interp1(actual_nm,DL_normalised,wl);
figure(40);
plot(wl ,Coro_Spect,'r');
legend('Corocam');
xlabel(' Wavelenght [nm] '); %  x  label
ylabel('  Analogue Value'); % y label
title(' Scaled Corocam 504 Spectral response  ');%  The graph's label
CamSpectrals(:,4)=Coro_Spect;
%------------------------------------------------------------
%%
% Plot the Filter and Detector Response values ....
display ('  Plot the different Camera relative responses ');
figure(3);
%subplot(2,1,1);
plot(wl ,CamSpectrals(:,1),'r',wl ,CamSpectrals(:,4),'g',...

wl,CamSpectrals(:,2),':k',wl,CamSpectrals(:,3),'b','LineWidth',3');%wl,Ffilt_dum_
nm)
legend('Camera_G_A_U_S_S','Corocam 504','Camera_W_I_D_E','Camera_N_A_R_R_O_W',1);
axis([160 350 0 1.05]);
xlabel(' Wavelenght [nm] '); %  x  label
```

Department of Electrical, Electronic and Computer Engineering
University of Pretoria

100

```matlab
ylabel('  Spectral Response'); % y label
title('Simulated Camera Spectral Responses and Corocam');%  The graph's label
grid on;

%% --------------------------------------------------------------
graphstotal =4;

for GraphNo = 1 : graphstotal


    Ts_steps =10;
    Ts_Cstrt =900;
    Ts_strt = Ts_Cstrt + 273.16;
    Ts_Cmax =1200;
    Ts_max = Ts_Cmax + 273.16;

    No_graphsteps = (Ts_max-Ts_strt)/Ts_steps;
    stepNo  =1;
    Totalcalc = rand(No_graphsteps+1,1);
    Totalcalc(:) = 0;
    Txi = Totalcalc;


for Tsource = Ts_strt:Ts_steps:Ts_max
   Txi(stepNo)=Tsource;
%-------------------------------------------------------------
%  Cell ... the Source a black body radiator....
% Planck's law in wavelength domain,
% display ('  Create Source black body array values ');

M_source =PLANCK_EL_nm(wl,Tsource);               % Get source emittance [W/m^2]
L_source = M_source/pi;                   %Get the sourc radiance ..emmisivity
is 1
% display ('  Plot Source BB emittance graph  ');
% figure(11);
% plot(wl,M_source)
% xlabel(' Wavelenght [nm] '); %  x  label
% ylabel('M Emittance [W.m^-^2]'); % y label
% title(' Planck Source @ 6000[K]');%  The graph's label
%-------------------------------------------------------------
% Input parameters
  D_src = 22.2e-3 ;            % Diameter of the source given..22.2 mm [m^2]
  A_src = (pi *((D_src)^2))/4;   % Circular source area
  A_lns = (pi *((62e-3)^2))/4; % Area of lens..given
  Rdistance=20;                    % Distance between source and detector in [cm]
 % Part that is doesn't form part the integral
  Tot_constant =((1e-4)*A_src)/((Rdistance*Rdistance));
   % do the integral portion using a loop
 Tot_integral =0;     % - Init the current to zero for the loop...

strtvalue=1;             % Index to 0

for x=strtvalue:StopsIntegral
                                    %Only the radiance and
                                    %    Responsivity
    Tot_integral = Tot_integral+( L_source(x)*CamSpectrals(x,GraphNo));
                                    % ..usually filter and
                                    % atmospheric transmittance also but
                                    % they are unity (=1) in this case
end

 Totalout=  Tot_constant * Tot_integral; % Id = constant x Integral
```

Department of Electrical, Electronic and Computer Engineering

University of Pretoria

101

```matlab
 Totalcalc(stepNo) = Totalout;
 stepNo=stepNo+1;

%
end;
  Id_Graph(:,GraphNo)=Totalcalc;
end;
%%
 display ('  Plot Planck Source versus Irradiance energy ');

figure(60);

plot(Txi,Id_Graph(:,1),'r',Txi,Id_Graph(:,4),'g',Txi,Id_Graph(:,2),':k',Txi,Id_Gr
aph(:,3),'--b','LineWidth',3);
 axis([1200 1500 0 4.0e-15]);
legend('Camera_G_A_U_S_S','Corocam_5_0_4','Camera_W_I_D_E','Camera_N_A_R_R_O_W',2
);
 xlabel(' Planck Source input in terms of absolute Temperature[K] '); %  x  label
 ylabel('Irradiance E [W.cm^-^2]'); % y label
 title(' Comparison: Camera output responses at 2[m]');%  The graph's label
 grid on;
 disp(' ...done Matlab simulation');

%=================================================================
%=================================================================
% Function in separate file
% FILTER.M
% Calculate Transmittance of filter
%  um wavelength or for nm use * 1000
% input values:
% wl  array of wavelengths
% tsup = 0.0; Camera response in non-pass suppression
% tpass = 0.8;   % Camera relative response pass band
% wl_wcf_nm Centre wavelength pass band
% shape = 2 ; % Shape gauss if  =2
% wl_wide = 0.02 % width in nm of passband

function y=FILTER(wl,wl_wcf_nm,wl_wide,tpass,tsup,shape)

y = tsup +tpass*exp(-(2*(wl -wl_wcf_nm)/wl_wide).^shape); % Filter formula

%=================================================================
%=================================================================
% Function in separate file
%% The Source energy description
%  PLANCK_EL_nm.M
% Planck's law radiant emittance
% Operate in the nm
% input values:
% x == wavelength vector in  [nm]
% t_Kelvin == temperature in [K]
%  10^3  for the nm scale
% returns :
% spectral emittance [W.m^-2.nm^-1]

function y=PLANCK_EL_nm(w,t_Kelvin)

y= 3.7418301e20 ./ (w .^ 5 .* ( exp(14387863.142 ./(w * t_Kelvin))-1));
```

A.8.   PLANCK VERSUS MONOCHROMATOR SOURCE ENERGY

Table A.5. Monochromator versus Planck source energy at camera lens at 3.84 metres

Wavelength [nm]	E $_{Monochromator}$ [W.cm^{-2}.nm]	E $_{Planck\ 1200C}$ [W.cm^{-2}.nm]	E $_{Planck\ 1200C}$ x100 [W.cm^{-2}.nm]	Camera Spectral
200	3.18E-14	6.0496E-22	6.05E-20	20
205	5.7404E-14	1.7595E-21	1.76E-19	20
210	9.29E-14	4.8495E-21	4.85E-19	20
215	1.34E-13	1.2715E-20	1.27E-18	20
220	1.7641E-13	3.1826E-20	3.18E-18	20
225	2.09E-13	7.6283E-20	7.63E-18	20
230	2.37E-13	1.7560E-19	1.76E-17	20
235	2.62E-13	3.8923E-19	3.89E-17	20
240	2.73E-13	8.3276E-19	8.33E-17	40
245	2.82E-13	1.7236E-18	1.72E-16	60
250	2.76E-13	3.4579E-18	3.46E-16	120
255	2.70E-13	6.7374E-18	6.74E-16	160
260	2.63E-13	1.2770E-17	1.28E-15	190
265	2.57E-13	2.3586E-17	2.36E-15	157
270	2.49E-13	4.2509E-17	4.25E-15	115
275	2.34E-13	7.4863E-17	7.49E-15	55
280	2.26E-13	1.2899E-16	1.29E-14	35
285	2.08E-13	2.1772E-16	2.18E-14	20
290	1.96E-13	3.6036E-16	3.60E-14	20
295	1.91E-13	5.8549E-16	5.85E-14	20
300	1.82E-13	9.3469E-16	9.35E-14	20

```
%% Start of Matlab code file. =================================================

%-----------------------------------------------------------------------------
% File_name : MonoVersusPlanck.m                        author : C Coetzer
%
%   Description: Unravel the relation between the monochromator and Planck Source
%   energy, thereby validating the gain relation of the Camera itself
%-----------------------------------------------------------------------------
%23456789012345678901234567890123456789012345678901234567890123456789012345678 90
%         1         2         3         4         5         6         7         8
%-----------------------------------------------------------------------------
%
%
%%
%  Matlab code starts
display ('  ==================================================== ');
display (' File =  MonoVersusPlanck.m  unraveling relation with source energy
');
clear ;       % clear simulation memory to avoid problems
```

Department of Electrical, Electronic and Computer Engineering   103
University of Pretoria

```
%%
display ('  Create array of nm Wavelenghts ');
wl = 200:5:300; % wavelenghts values starting at 200nm  up to 285 nm
                    % using steps of 5 nm


%% --------------------------------------------------------------------
% Create the data array for Planck Source at 3.84 Meters from the camera
% for the energy that arrives at the lens input.
Tc = 1200 ;                 % Degrees Celsius
Tsource = Tc +273.15;           % 1200 degrees celsius is so much Kelvin
Msource =PLANCKEL_nm(wl,Tsource); % Get source emittance [W/m^2] using Planck nm
function
Lsource = Msource/pi;       % Get the sourc radiance ..[W/m^2.sr^1]
                            %   with sr = pi for planck source emmiting a half
sphere
Ds = 22.2e-3 ;              % Diameter of the source given..22.2 mm [m^2]
  A_src = (pi *((Ds)^2))/4;   % Area of the source seen as disc by detector
  AL = (pi *((62e-3)^2))/4; % Area of lens..given
  Rdist=3.84;               % Distance between source and lens in [m]

% Total Irradiance [W/m^2] energy on the lens of camera
% E = Lsource . Omega  = Radiance . solidangle  =
% Simplified case is
% E = L . Asource / distance^2
% L is dependant of wavelenght ...has a value each nm

% For the simplistic case Portion outside the integral

  Omega  =( A_src)/((Rdist*Rdist));
 %% Callculate the energy of the lens upon the
 % The energy upon the lens is thus  per wavelenght
 %  this is with units[W/m^2.nm]
  E_lens =  Lsource * Omega;
 %% Prepare this for comparison with the Monchromator data
 % The data of the monochromator is however in [W/cm^2.nm]
 % It thus implies that the to correct the number ....
 Elens_W_cm2_nm = E_lens * 1e-4;
%% --------------------------------------------------------------------
%   monochromator calibration Data
%   Units is [W.cm^-2], at a distamce of 0.9 meters obtained with reference
%   detector is obtained the following table
Ecalmono = [5.7800E-11 1.0450E-10 1.6916E-10 2.4446E-10 3.2114E-10 3.8046E-10...
            4.3149E-10 4.7681E-10 4.9788E-10 5.1291E-10 5.0261E-10 4.9177E-10...
            4.7857E-10 4.6738E-10 4.5326E-10 4.2593E-10 4.1170E-10 3.7889E-10...
            3.5622E-10 3.4718E-10 3.3064E-10];
r_cal= 0.09;    % Calibration Detector and monochromator distance
rcamera =3.84; % Camera and monochromator distance
% Use projection back to origin L radiance or Van Schalwyk's fix
% Assume the energy in radiance of the monochromator is Lmono [W.sr-1.nm.cm-2]
% Ecalmono = Lmono . omega_rcal = Lmono . Area Monochrome fibre / r_cal ^2
%  where it is assumed to sources are perpendicular to each other
% thus want to know
% Emonolens = Lmono . omega_rcamera
%          = Lmono . Area Monochrome fibre/(rcamera *rcamera )
% using the two equations as Lmono is in both
% implies thus
Emonolens = Ecalmono * ((r_cal/rcamera)*(r_cal/rcamera));

% the following is the data generated with spreadsheet (give the result)
%% Data at 3.84 Meters for the monochromator
```

```
% Emonolens = [3.1751E-14 5.7403E-14 9.2924E-14 1.3428E-13 1.7641E-13 2.0899E-
13...
%             2.3703E-13 2.6192E-13 2.7349E-13 2.8175E-13 2.7609E-13 2.7013E-
13...
%             2.6289E-13 2.5674E-13 2.4898E-13 2.3397E-13 2.2615E-13 2.0813E-
13];
%% Data provided by casting to and back L method by going back to 2metres
%  Emonolens = [1.17046E-13 2.1161E-13 3.42556E-13 4.95023E-13 6.50302E-13
7.70424E-13...
%             8.73772E-13 9.65549E-13 1.0082E-12 1.03864E-12 1.01778E-12
9.95825E-13...
%             9.69109E-13 9.46441E-13 9.17856E-13 8.62508E-13 8.33687E-13
7.67251E-13];
%%
 % Plot a figure
 figure(99);
 Elens_W_cm2_s = Elens_W_cm2_nm *100;
 plot (wl,Elens_W_cm2_s,'r',wl,Emonolens,':b','LineWidth',3');
 axis([200 300 0 3.1e-13]);
 title(' Monochromator vs Planck 1200^oC Source @ 3.84 Metres ');% main graph
label
 xlabel(' Wavelenght [nm] '); % add a name to the x axis
  ylabel('Irradiance E [W.cm^-^2]'); % y axis name
 legend('Planck_1_2_0_0_C x100',' Monochromator',0);
 grid on;
 grid minor;
 %set(axes_handle,'XGrid','on');
%%
 display ('  Use the actual Corocam 504 SN 006 analog measured spectral response
');
DLvalue = [20 20 20 20 20 20 20 20 40 60 120 160 190 157 115 55 35 20 20 20 20];
FilterNormalise = (DLvalue -20)/(190-20);
%%
% Calculate the irradiance where the Planck source was observed by the
% camera with a gain of 55% to max of 70 Gain which is 2 metres
% .. that is where the 2 in next formula comes from...
Elens_W_cm2_nm_2m = Elens_W_cm2_nm *((rcamera/2)*(rcamera/2));
%Perform a rough estimate of the value of the values after it passes the
% through the camera using rough spectral transfer function
Elens_W_cm2_nm_2m_Filt = Elens_W_cm2_nm_2m .* FilterNormalise;


%%
Elens_W_cm2_nm_2m_Filtsum =sum(Elens_W_cm2_nm_2m_Filt);

%% The value has a ration to the monochromator at 260nm value
Emono260nm =Emonolens(13);
%% Amplify this by approx 4967
Emono260nmG5 =Emono260nm *4967;
% amplify Planck by effective 200000 or 100000
Elens_W_cm2_nm_2m_FiltsumGx = Elens_W_cm2_nm_2m_Filtsum *100000;

%% Determine the ratio of monochromator and summarised Planck value
Eratio = Emono260nmG5 /Elens_W_cm2_nm_2m_FiltsumGx;
```